Lagrangian Analysis of Thunderstorms in Switzerland

Master Thesis

Faculty of Science

University of Bern

handed in by

Thomas M. Lanz

2020

Supervisor

Prof. Dr. Olivia Romppainen-Martius

Oeschger Centre for Climate Change Research

Institute of Geography, University of Bern

Abstract

Thunderstorms occur frequently in Switzerland and they can cause severe damage. Although their frequent occurrence, the initiation of thunderstorms is still incompletely understood. Here, this master thesis aims to contribute to a better understanding of conditions and processes leading to thunderstorm initiation in Switzerland. Therefore, trajectories were calculated with Lagranto in high resolution WRF model data simulated for May 2018. The research of thunderstorms by calculating trajectories in high resolution model data, is a novel approach and enabled new insights into the formation of the atmospheric layers. Combined with other analysis tools, five case studies were conducted and the basic ingredients for thunderstorm initiation were therein investigated. The assessment of the responsible triggering mechanisms revealed a high relevance of the presence of low-level convergence (all case studies), a direct impact of storm outflow boundaries (two case studies) and a strong influence of the orography (three case studies) on the initiation of the respective thunderstorm. The second part of this thesis addressed the impact of the changing climate on the initiation of thunderstorms, which is still an open question. Therefore, the pre-strom environments of all thunderstorms in May 2018 and in end of the century climate conditions were analysed. The comparison between the two climate conditions indicates a higher potential for strong and short-lived convection in end of the century climate conditions.

Contents

1 Introduction

During the summer months in Switzerland, thunderstorms occur frequently and can cause severe damage (Huntrieser et al., 1997; MeteoSwiss, 2018a; Nisi et al., 2016; Trefalt et al., 2018) of more than US$1 billion for a single event (Allen et al., 2017). Although they appear in Switzerland on small spatial scales (compared to e.g. a foehn storm), they produce high precipitation amounts in short time periods and there is high damage potential by hail, lightning and wind gusts (Doswell et al., 1996; García-Ortega et al., 2007; Trefalt et al., 2018). Therefore, an in-depth understanding of these destructive weather systems is of great importance and that having an accurate forecast for them is a desirable goal. Despite their frequent occurrence and damage potential, the initiation of thunderstorms is still incompletely understood. This applies also for the projection of their behaviour in future climate conditions. How the initiation of thunderstorms will be impacted by the changing climate is still an open question (CH2018, 2018). By studying the initiation of thunderstorms in current (and future) climate conditions in Switzerland, this master thesis aims to improve the understanding of conditions and processes leading to thunderstorm initiation.

For the research of thunderstorm initiations in current climate conditions, the month of May 2018 was selected because of its characteristics disclosed in the following. This month reached the second warmest mean temperatures ever measured locally and the fifth warmest mean temperatures ever measured nationally (MeteoSwiss, 2018d). In Switzerland, these record values of May 2018 contributed to the warmest summer half-year (April until September) since the beginning of measurements in 1864 (MeteoSwiss, 2019). In addition, the thunderstorm activity in May 2018 was above average by comparison to the long term climatology (MeteoSwiss, 2018b). In the second half of May especially, a series of thunderstorms moved across Switzerland and brought high amounts of precipitation with it locally (MeteoSwiss, 2018a) and also hail in certain areas (MeteoSwiss, 2018c; Sturmarchiv, 2019). Besides the high frequency in thunderstorms, their tracks were unusual too. Whereas thunderstorms move typically from southwest to northeast over Switzerland, the direction of origin of most storms switched to south, southeast or even to northeast (MeteoSwiss, 2018b). Because of these characteristics, the month of May 2018 is chosen for in-depth research in this master thesis.

May 2018 falls within the convective season of Switzerland, which runs from April until September. That is when favourable conditions for the evolution of thunderstorms are present (Nisi et al., 2018). In general, a thunderstorm is defined by the American Meteorological Society (AMS) as "a local storm, invariably produced by a cumulonimbus cloud and always accompanied by lightning and thunder, usually with strong gusts of wind, heavy rain, and sometimes with hail" (AMS, 2012). For the evolution of deep convection (thunderstorms, but includes also nonthundering convection; hereafter "thunderstorm" will include all deep convective cells) some atmospheric preconditions need to be met. These preconditions comprise a substantial amount of boundary-layer moisture, a conditional instability present in the atmosphere and a triggering mechanism to cause lifting of boundary-layer air (Doswell et al., 1996; Stull, 2015; Wallace & Hobbs, 2006). These preconditions represent the basic ingredients for thunderstorm initiation.

Due to the complex topography of Switzerland (see Figure 1.0.1), the causes (triggering mechanisms) of thunderstorm initiation are manifold (Graham et al., 2012; Houze et al., 1993; Nisi et al., 2018; Trefalt et al., 2018). Therefore, their identification will be of main interest in this study. The research will focus on the definition of the responsible atmospheric conditions and processes for the initiation of selected thunderstorms (case studies) spread across Switzerland. Thereby, this master thesis aims to make a contribution by understanding better the local thunderstorm initiation processes in Switzerland, with its complex topography.

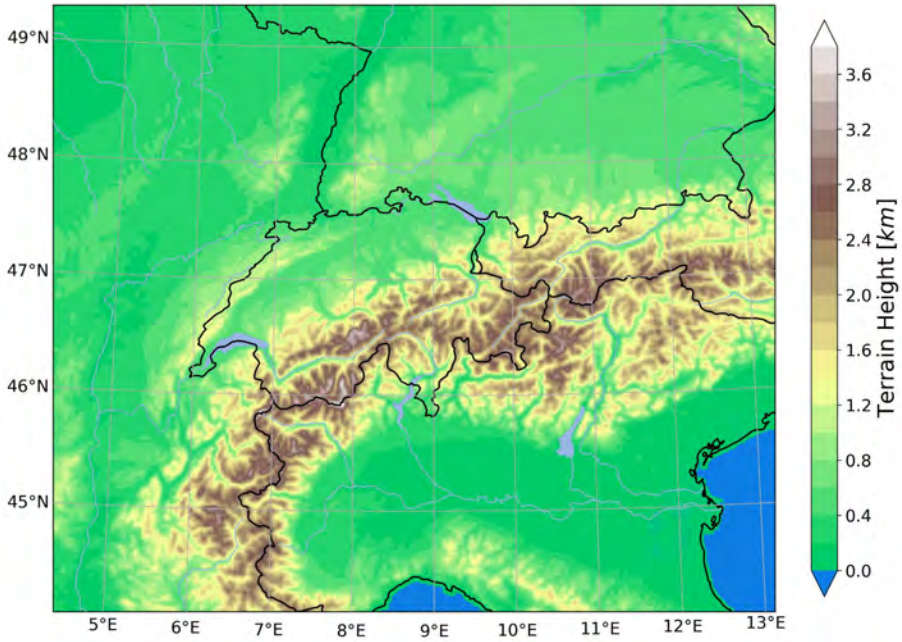

Figure 1.0.1: Investigation area with terrain height [km] from the inner domain of the WRF (ARW) model.

For the analysis of small-scale weather phenomena (like convection) in such complex topography, the utilised data need to be of high resolution in order to capture these phenomena more accurately. The Weather Research and Forecasting (WRF) model (Powers et al., 2017), used in this master thesis, can be of very high resolution and thus capture small-scale weather patterns. Despite this high resolution, important small-scale weather processes (for thunderstorm initiation) still need to be parameterised in the model. This parameterisation of cloud (ice-phase) microphysics can be done with different microphysics schemes. Based on tests carried out, the predicted particle properties (P3) scheme (Morrison & Milbrandt, 2014) was chosen for the parameterisation in the WRF simulations of this master thesis. The convection-permitting WRF model outputs comprehensive three-dimensional fields of the atmosphere in very high temporal and spatial resolution. This enables an in-depth atmospheric research based on many different variables and the use of Lagrangian analysis tools. In addition, the model can simulate the atmospheric conditions in climate change scenarios. This is a further advantage of model data compared to e.g. radar data.

This study will use WRF model data from simulated future climate conditions by the end of the 21st century. Based on the current projections, a warming climate will intensify the frequency of heavy precipitation events (Ban et al., 2015) in all regions and seasons of Switzerland (CH2018, 2018). Furthermore, the authors of the recently published climate scenarios for Switzerland (CH2018, 2018, p. 132) "indicate that future increases in summer precipitation over high alpine elevations are associated with enhanced convection". Although, the future thunderstorm behaviour remains highly uncertain in the models (CH2018, 2018). These uncertainties are "related to the representation of clouds, moist convection, and complex topography" (Ban et al., 2014, p. 1) in the models. Thus, further research with convection-resolving models is needed and will be conducted in this master thesis. Therefore, the research in this thesis will be supported by an analysis of the pre-storm environments of all thunderstorms in May 2018 and in the same month with end of the century climate conditions.

In the present simulations of May 2018, the air parcels of the thunderstorm initiation area will be traced with Lagranto, a Lagrangian analysis tool (Sprenger & Wernli, 2015; Wernli & Davies, 1997). Lagranto can calculate trajectories of air parcels backwards in time. These trajectories make it possible

to detect where air parcels originate by following the parcel's path. Beside this spatial reference, additional information can be gained regarding the evolution of variables along the trajectories. Using Lagranto in such high resolution model data and for analysing the initiation of thunderstorms, is a novel approach. By the application of this novel approach, the present master thesis aims to acquire new insights in the conditions and processes regarding thunderstorm initiation. Besides the Lagrangian perspective, also the Eulerian perspective will be taken by analysing the initiation environment regarding the important variables for thunderstorm initiation at a specific point in space. The combination of the two perspectives will result in an evaluation of the atmospheric conditions and processes leading to thunderstorm initiation in May 2018.

1.1 State of Knowledge and Research Questions

Thunderstorm initiation is mainly related to the availability of the preconditions for thunderstorm initiation. These environmental preconditions are nowadays well known and consist of three basic ingredients:

- a substantial amount of boundary-layer moisture,
- a conditional instability present in the atmosphere, and
- a triggering mechanism to cause lifting of boundary-layer air

(Doswell et al., 1996; Stull, 2015; Wallace & Hobbs, 2006). Translated into air parcel theory after Doswell et al. (1996, p. 563), "there must be sufficient moisture that some rising parcel's associated moist adiabat has a level of free convection (hereafter LFC), the environmental lapse rate must be conditionally unstable and there must be some process by which a parcel is lifted to its LFC". Strong wind shear is defined as a forth basic ingredient by Stull (2015), based on the argument of a sufficient "fuel" supply for the development of an intense and long lasting thunderstorm. Because if a vertical wind shear (change in wind speed and/or direction with height) is present in the lower troposphere, the boundary layer air would move relatively to the thunderstorm and supply the thunderstorm with moist and warm air ("fuel"). Vertical wind shear and its influence on the evolution of thunderstorms is further described in 2.4 Thunderstorm Processes. In the following, I will present each basic ingredient and its relevance for thunderstorm initiation in more detail.

A substantial amount of moisture in the Planetary Boundary Layer (hereafter PBL) builds the main energy source of thunderstorms. As the moist air of this layer rises and cools in the updrafts of the thunderstorm, water vapour condenses and latent heat is released. The warmer and moister boundary-layer air is, the more intense thunderstorms can get (if the other basic ingredients are available too) (Stull, 2015). Johns and Doswell (1992) expanding the location of the moisture layer up to the mid-troposphere, mainly emphasising a sufficient depth of the respective moist layer.

Conditional instability occurs due to a temperature inversion capping the warm moist boundary-layer air with relatively colder air aloft. If warm air ascends over this inversion, then the colder environmental air increases the updraft of the warm air and hence the strength of thunderstorms (Stull, 2015). The strong updrafts are resulting from the potential energy inherent in the temperature and moisture stratification of the atmosphere, which is represented by the Convection Available Potential Energy (hereafter CAPE). In Switzerland, a modified version of this parameter (CAPE_{CCL}) forecasted most successfully the probability of widespread or isolated thunderstorms in the course of the day (Huntrieser et al., 1997). Therefore, CAPE is a valuable indicator for the strength of possible convection. CAPE values exceeding 4000 J kg^{-}1 can result in extreme, 2500-4000 J kg^{-1} in strong, 1000-2500 J kg^{-1} in moderate and 0-1000 J kg^{-1} in marginal convection. This is a classification based on the conditions in the USA. According to Bott

(2016), CAPE values over 3000 J kg^{-1} have a rare occurrence in Central Europe, which was confirmed in a reanalysis study by Brooks (2009). During the "Grossversuch IV" in Switzerland, CAPE values were measured ranging between 340 to 2340 J kg^{-1} (Huntrieser et al., 1997).

Aside from high CAPE values, Convective Inhibition (hereafter CIN) should be small, but non-zero (0-100 J kg^{-1}). CIN can be viewed as the required energy to lift an air parcel to its LFC and deep convection is unlikely to occur if they exceed 100 J kg^{-1}. The presence of a stable layer or inversion at the top of the PBL corresponds to the presence of CIN values. If they would be zero (i.e. no inversion), then air parcels can constantly reach their LFC and release CAPE, which can not build up high values supporting vigorous deep convection (Wallace & Hobbs, 2006). In addition without a capping inversion, the warm and moist air is no longer trapped and hence the energy source for the thunderstorm is missing (Stull, 2015).

For the release of the CAPE inherent in the temperature and moisture stratification, the environmental air needs to be destabilised (lowering of CIN) by a triggering process to cause lifting of boundary-level air. Moreover, air parcels need to be lifted to their LFC in this destabilised environmental air. This destabilisation corresponds to a weakening of the inversion layer above the PBL, which can be achieved by lifting and/or radiative heating. Subsequently, buoyant air parcels can break through this statically stable layer (Wallace & Hobbs, 2006). If the trigger mechanism is strong enough to lift the air parcels up to their LFC, they can rise and accelerate under their own buoyancy still following the moist adiabat (Stull, 2015). Bott (2016) describes also the influences of the intense diurnal solar radiation during the summer months. As a consequence of this heating, the resulting turbulence decreases more and more boundary-layer CIN (i.e. the PBL height can reach the LFC) and the air can rise without external forcing to its LFC.

Lifting is associated to low level convergence, which destabilises the environmental air and is often driven by some large-scale forcing mechanism (e.g. upper level trough) (Wallace & Hobbs, 2006). The large scale atmospheric processes are mainly responsible for the thermodynamic structure and the corresponding instability. On the other hand, Doswell (1987) attributes the mesoscale processes the main responsibility for the initiation of the convection. The initiation triggering air parcel "is usually associated with a more localized, short-lived and less predictable forcing mechanism" (Wallace & Hobbs, 2006, p. 347). These mechanisms (triggers) are responsible for the initial lifting of a boundary-layer air parcel to its LFC. Stull (2015, p. 525) divides them into triggers with airmass boundaries like "synoptic fronts, dry lines, sea-breeze fronts, gust fronts from other thunderstorms"; and other triggers like mountains, atmospheric buoyancy waves and localised regions of excess surface heating. Apart from that, another triggering mechanism can occur due to urbanisation and the corresponding urban heat island effect. Haberlie et al. (2015) analysed this influence of urbanisation on thunderstorm initiation and found an positive impact of the urbanisation on the frequent occurrence of convective events. In the following, some important triggering mechanisms for Switzerland are explained in more detail.

Airmass boundaries are defined as the dividing lines between denser and less-dense airmasses. If there exists any convergence towards this boundary, then the denser airmass force the less-dense air to rise over it. On a synoptic scale, airmass boundaries are described as warm and cold fronts. Lake- (or sea-)breeze fronts are another example of the interaction between airmasses with different densities (Stull, 2015). On a smaller scale, the downdrafts (or even downbursts, see 2.4 Thunderstorm Processes) of a matured thunderstorm can trigger the initiation of other thunderstorms. This happens along the forward propagating gust front, which contains the evaporative cooled air from the downdrafts. Due to its higher density, the cool air of the gust front slides under the warm and moist air of the PBL. This

air is lifted by the gust front until its LFC, where the air gets buoyant and new cells are developing through condensation (Wallace & Hobbs, 2006). Besides varying temperatures, airmass boundaries can also develop due to varying moisture content between the airmasses (called dry lines). If these airmasses of warm humid and warm dry air converge, then the less-dense humid air is forced to ascent (Stull, 2015). In addition to the previously described airmass boundary triggers, the International H_2O Project (IHOP_2002) described the impact of boundary types like horizontal convective rolls or undular bores on thunderstorm initiation (Weckwerth & Parsons, 2006).

As already mentioned, the topography of Switzerland is very complex and Huntrieser et al. (1997, p. 122) stated that this "topography plays a crucial role for the initiation of thunderstorms in a mountainous country like Switzerland". During summer days in Switzerland, a large amount of air and water vapour is transported from the lowlands to the nearby western Alps (diurnal mountain-valley wind system). The associated airflow convergence results in orographic convection and hence can initiate thunderstorms in the afternoon and evening (Graham et al., 2012). The COPS (Convective and Orographically-induced Precipitation Study) found other orography-related forcing mechanisms of convection and classified them as follows: "(i) surface heating and low-level flow convergence; (ii) surface heating and moisture supply overcoming convective inhibition during latent and/or potential instability; or (iii) mid-tropospheric dynamical processes due to mesoscale convergence lines and forced mean vertical motion" (Kottmeier et al., 2008, p. 931).

In the last paragraphs, I presented the state of knowledge regarding the initiation of thunderstorms. The basic ingredients for thunderstorm initiation are already well known since a longer time. But the assessment of the interplay of the different ingredients is still incompletely understood. Further, the definition of a possible triggering mechanisms is difficult and varies from one thunderstorm initiation to the other. This is manly owed to the differences of the small-scale processes and conditions in each thunderstorm initiation, which holds especially for Switzerland with its complex topography. In order to tackle this outstanding issue in meteorology (Graham et al., 2012), the following research questions are addressed in this master thesis:

[A] How relevant was the presence of convergence for the initiation of selected thunderstorms in May 2018 in Switzerland?

[B] Which impact had storm outflow boundaries on the initiation of selected thunderstorms in May 2018 in Switzerland?

[C] How far influenced the complex topography of Switzerland the initiation of selected thunderstorms in May 2018?

[D] How might the temporal evolution of important variables before thunderstorm initiation and their magnitude change in future climate conditions?

The in-depth analysis of different case studies in May 2018 generates a lot information about the particular basic ingredients for thunderstorm initiation. A novel approach is implemented in this research, which uses a Lagrangian analysis tool for the research of thunderstorm initiation with high resolution model data. This new perspective can contribute to a better understanding of the local thunderstorm initiation processes in Switzerland, with its complex topography. Based on this information, the particular triggering mechanism can be assessed for each case study. Finally, the comparison of the pre-storm environments of all thunderstorms in May 2018 and in end of the century climate conditions enable inferences about the atmospheric conditions for thunderstorm initiation following a climate change scenario.

Following this section, a description of the basic notions (2 Basic Notions), data (3 Data) and methods (4 Methods) used in this master thesis are presented. Subsequently, in Section 5, the results are presented, and they are discussed in Section 6 to answer the research questions. Finally, the conclusions appear at the end in Section 7.

2 Basic Notions

2.1 Historical Overview

The invention of the telegraph 1833 enabled the communication between remote weather stations and marked the formation of national weather services in the late 19th century. Since the beginning of the weather services, the prediction of thunderstorms was always of interest. After World War I, the physical laws for atmospheric processes of the Norwegian school were globally recognised, also due to the growth of the aviation industry. But until the middle of the 20th century, the resources for thunderstorm research were limited. The developments of radiosondes and radar after World War II is tantamount to progress in thunderstorm research from then on (Galway, 1992). This development peaked in the first large-scale investigation of thunderstorms in 1946-47, known as the Thunderstorm Project (Byers & Braham, 1949). "The systematic ground and airborne measurements that were made enabled much of the structure, dynamics, and physical nature of thunderstorms to be defined for the first time" (Pierce, 1976, p. 1214).

Thirty years later (1976), the Thunderstorm Research International Program (TRIP) conducted another large-scale project with improved measurement techniques. "The experiments include radar observations; electrical measurements at the ground and from aircraft and balloons; tests of various methods for locating lightning; studies of thunder; and so on" (Pierce, 1976, p. 1214). In Switzerland, the randomised hail suppression experiment, known as "Grossversuch IV" (Federer et al., 1978), marked an important milestone in thunderstorm and hail research. During five years (1977-81), selected hail cells were seeded with rockets containing silver iodide. Afterwards, the hail kinetic energy was independently measured by a dense hailpad network and a calibrated radar. The results of the experiment showed no significant difference between seeded and unseeded hail cells. Instead of suppression hail formation, "a majority of the evaluations suggest some trend to larger seeded-hail energy and larger seeded-hail area values" (Federer et al., 1986, p. 949).

Based on these developments in the observation of thunderstorms, the understanding of their physical processes was improved and possible ingredients of thunderstorm initiation (atmospheric instability, a process which releases this instability and vertical motion) were already defined in the middle of the 20th century (see Figure 2.4.1). But the proof of these assumptions was not possible due to the missing observation techniques (House, 1963). After the turn of the millennium, these observation techniques became available and several field campaigns researched the initiation of convection. For example, the International H_2O Project (IHOP 2002, USA) focused on the influence of the mesoscale wind and humidity discontinuities in the PBL for the convection initiation. Another field campaign, the Convective Storms Initiation Project (CSIP 2004 and 2005, UK), analysed convection in weak convective instability and capping inversions. Another example can be given by the already mentioned COPS (see 1.1 State of Knowledge), where the focus of the research was set on the influence of the orography on the convection initiation in southern Germany and eastern France (Kottmeier et al., 2008).

2.2 Numerical Simulation

The first attempt to simulate numerically the evolution of moist convection was in 1963 by a study of Ogura (1963). Afterwards, several studies followed until a first numerical simulation of the life cycle of a thunderstorm was published in 1971 (Ogura & Takahashi, 1971). In the model of this study, the vertical equation of motion, the equation of mass continuity, the first law of thermodynamics and several microphysical parameters were included (like for example the condensation of water vapour to produce cloud droplets or conversion of cloud droplets to raindrops). The model could qualitatively simulate some aspects of the three stages of life cycle of a cumulus cloud defined by Byers and Braham (1949) after

the Thunderstorm Project (see 2.1 Historical Overview). Further, the study remarked the importance of the rate of conversion from cloud droplets to raindrops for the life cycle duration of a thunderstorm cell. Although the parameterisation of the model's microphysical processes was kept very simple, the results of this study were promising and laid the basis for further research and progress in this area (Ogura & Takahashi, 1971).

Thunderstorm research by climate models started only by the end of the 20th century. The reason for the late development lies in the dependence on computing resources. Because only with high spatially and temporally resolved Regional Climate Models (RCM) research on small-scale processes (like thunderstorms) can be done. RCMs are nested in General Circulation Models (GCM), which include the large-scale processes in lower resolution. With these inputs of the GCMs, the RCMs can increase the temporal and spatial resolution for a limited area of interest (Beniston et al., 2007). With a rapid technical evolution in this research area since the end of the 20th century, RCMs can nowadays simulate future climate change including convection and mesoscale orography at 4 km grid spacing (Liu et al., 2017).

But, the spatial and temporal resolution of these RCMs are still too coarse for capturing small-scale weather processes (like thunderstorms). Due to this deficiency, small-scale weather processes need to be parameterised before they are included in a RCM. This parameterisation is a difficult task and for this reason the Convective Storm Initiation Project (CSIP) was founded (Browning et al., 2007). The aim of the CSIP is an improvement of numerical weather prediction (NWP) models. Only through the development of very highly resolved NWP models (like the WRF model in this master thesis with 1.5 km grid spacing), in-depth (case) studies are possible in a high quality and accuracy. These are basic requirements for the analysis of small-scale weather phenomena. An recent example of such an in-depth case study of a thunderstorm can be found in Trefalt et al. (2018). Based on, inter alia, high resolution NWP data, they analysed in detail the thunderstorm of Thun in 2015. This thunderstorm was stationary over the city for several hours and resulted hence in large damage.

2.3 Observations

Another database for the analysis of thunderstorms are radar-based observations. By continuously scanning the atmosphere, radars receive high temporal and spatial resolved reflectivity values, which provide information on the precipitation intensity and the presence of hail. Beside insurance damage claims, radar data are the only continuous ground observations of hail in Switzerland (Trefalt et al., 2018) and are valuable for long term analysis of thunderstorms. For example Wilson and Schreiber (1986), Nisi et al. (2016) or Schemm et al. (2016) use radar data for the analysis of thunderstorms.

Based on radar data, Dixon and Wiener (1993) created a method to forecast the storm initiation, evolution and movement in such situations called Thunderstorm Identification, Tracking, Analysis and Nowcasting (hereafter TITAN). In this master thesis, the TITAN output is used for the definition of the time and location of thunderstorm initiations. Today, the nowcasting (short-term forecasting) with thunderstorm tracking algorithms is an important application of radar data, which enables the forecast and research of thunderstorms. Tailored to the complex topographic situation in Switzerland, Hering et al. (2004) developed such an algorithm for operational use in Switzerland called TRT (Thunderstorms Radar Tracking). In addition, for supplementing the research, most thunderstorm (case) studies combine radar data with other data sets like climate models, reanalysis model data, and so on.

2.4 Thunderstorm Processes

Deep cumulus convection is responsible for most of the precipitation in the tropics and over the continents of the summer hemisphere (Wallace & Hobbs, 2006). Further, it is often accompanied with heavy precipitation (sometimes flash floods) and strong wind gusts reaching hurricane force (Bott, 2016). The basic ingredients for thunderstorm initiation were in detail presented in 1.1 State of Knowledge. Here, the focus will be set on the evolution and more general processes regarding thunderstorms.

As already mentioned in the introduction (see 1.1 State of Knowledge), the vertical wind profile is of importance regarding the intensity and duration of thunderstorms. For the development of severe convection, high values of wind shear and CAPE are important (Brooks, 2009). If there is a strong vertical wind shear present, then the thunderstorm is capable of sustaining the updraft and the supply with low level moisture. Afterwards the air parcels rises until they reach their EL, where they lose their buoyancy and spread out to form the characteristic anvil shape. Otherwise with a weak shear, the downdrafts quickly isolate the updraft and therefore also the moisture supply. Veering (clockwise) and backing (anti-clockwise) of the wind with height also play an important role (especially for rotating supercell storms) in the dynamics of a thunderstorm (Wallace & Hobbs, 2006) or squall lines (Rotunno et al., 1988). With this turning of the wind-shear vector, a thunderstorm can be classified as a left- or right-moving storm. In Switzerland, the analysis of the data from the "Grossversuch IV" (see 2.1 Historical Overview) revealed an equal distribution of left- and right-moving storms (Houze et al., 1993).

Wallace and Hobbs (2006, p. 350) classify convective storms as follows:

- "relatively small, benign, single cell storms that form under conditions of weak vertical wind shear;
- more dangerous multicell storms that develop under conditions of strong vertical wind shear; and
- intense, robust, long-lived supercell storms with rotating updrafts formed from the splitting of multicell storms."

Single cell storms or just ordinary thunderstorms emerge from single cumulonimbus clouds. The initiation mostly happen due to local convection in an unstable atmosphere, rather than large-scale weather phenomena (e.g. fronts). The typical life cycle of an ordinary thunderstorm (see Figure 2.4.1) consists of three stages: (a) cumulus, (b) mature and (c) dissipating (Wallace & Hobbs, 2006). This idealised model is a result of the before mentioned Thunderstorm Project (see 2.1 Historical Overview). The life cycle of an ordinary thunderstorm takes from 30 (45 in mid-latitudes) up to 60 minutes (Klose, 2016).

The thunderstorm cell consists of warm and ascending air during the cumulus stage (see Figure 2.4.1a). With increasing height inside the cumulus cloud, the updraft and the cloud top rises strongly (up to 10 m s^{-1}). At the clouds lateral boundaries, the air is entrained by the strong updrafts, which transport supercooled raindrops aloft the freezing level (zero degree line). In the mature stage (see Figure 2.4.1b), a strong downdraft circulation is developing, where also most of the precipitation falls. The downward drag force of the cloud drops is causing this downdraft motion. Along their fall cloud drops evaporate and cool thereby the environmental air. This evaporative cooling can lead to an enhancement of the downdrafts (Wallace & Hobbs, 2006). In accordance with several different measurements, downdrafts can reach wind speeds greater than 20 m s^{-1} after the findings of Cotton and Anthes (1992). Very strong downdrafts during less than 30 minutes are called downbursts, which expand over an area of 1 to 10 km (Bott, 2016).

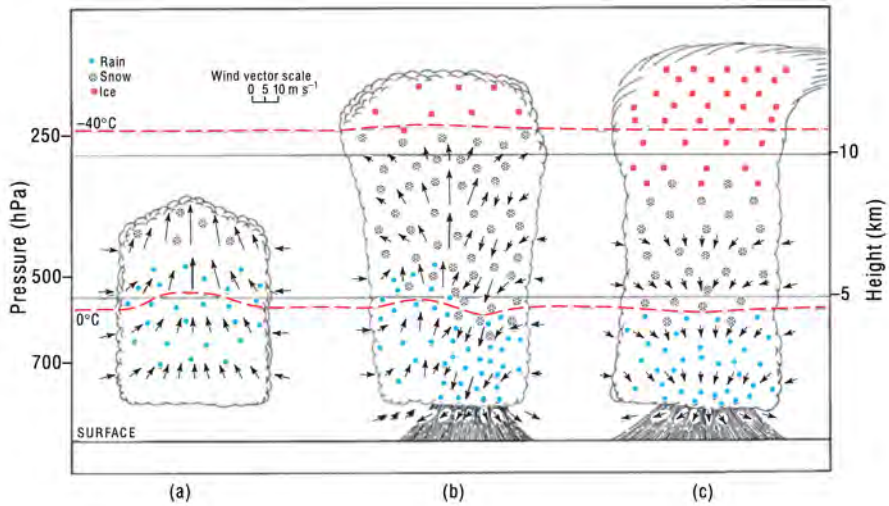

Figure 2.4.1: Schematic of a typical ordinary single-cell thunderstorm in three stages of its life cycle showing (a) cumulus stage, (b) mature stage, and (c) dissipating stage. The horizontal scale is compressed by about 30% relative to the vertical scale in the figure. The 0 °C and -40 °C isotherms are indicated in red. [Adapted from (Byers & Braham, 1949).] (Wallace & Hobbs, 2006, p. 351).

The maximum updraft area is located in the middle of the cloud and can exceed updraft speeds of 30 m s^{-1} (Cotton & Anthes, 1992). On the updraft side of the cloud (see Figure 2.4.1b, left), supercooled raindrops can be transported above the freezing level. While on the downdraft side (right) snowflakes or ice pellets can be found below the freezing line. If the top of the cloud reaches the tropopause and begins to spread out horizontally in an anvil shape, this marks the transition to the dissipating stage (see Figure 2.4.1c). Therein, precipitation and thus downdraft is spreading throughout the cloud. This results in a disconnection of the cloud droplets with supersaturated air from the updrafts, which in turn decays the growth of the cloud drops and precipitation subsides. This self-destruct mechanism of ordinary thunderstorms determines their duration and can only be eliminated by a vertical wind shear (Wallace & Hobbs, 2006).

Multicell storms consist of several single cell storms in different stages, which grow and decay with a duration of about half an hour. The vertical wind shear plays in this category an important role in the organisation of the multicell storms (Markowski & Richardson, 2010; Stull, 2015; Wallace & Hobbs, 2006). The degree of organisation increases with stronger vertical wind shear, until they merge into larger scale and/or longer lived entities. Often new cells build along the forward propagating gust front (see 1.1 State of Knowledge). The single cells survive until they fall behind the gust front. This repetitive process (of growth and decay of single cell storms) can keep the multicell storm alive for several hours (see Wallace and Hobbs (2006, p. 352) for a schematic).

If the cloud droplets have grown enough by the accumulation of condensed water vapour, their weight exceeds the updraft speed and they begin to fall. At the same time, dry air is entering the downdraft on the storms rear side. If the falling cloud droplets reach these areas, they evaporate and cool the ambient air. This results in an intensification of the downdrafts and the formation of a cold pool filled with cold and moist air. The strong updrafts along the downwind side of the multicell storm, produce at the tropopause an overshooting cloud top and an anvil with a wide expansion (Wallace & Hobbs, 2006). Because the occurrence of a supercell storm in Switzerland is a rare phenomena, I will left this category out of this thesis. Further information can be found in e.g. Schmid et al. (1997) or Wallace and Hobbs (2006).

3 Data

The data used in this master thesis are simulations of the Weather Research and Forecasting (WRF) model. The convection-permitting WRF model was developed by the National Center for Atmospheric Research (NCAR) in the late 20th century, and is one of the most widely used numerical weather prediction (NWP) models worldwide (Powers et al., 2017). Since the model's release in 2000, a 4th version of the WRF model has been developed, which is called the Advanced Research WRF (ARW). The ARW is a subset of the WRF model and "encompasses physics schemes, numerics/dynamics options, initialisation routines, and a data assimilation package" (Skamarock et al., 2019, p. 1). In this study, the parameterisation of cloud (ice-phase) microphysics in the simulations is done with the predicted particle properties (P3) scheme (Morrison & Milbrandt, 2014). The state of the atmosphere is output with a temporal resolution set at 5 minute intervals and a spatial resolution (grid size) of 1.5x1.5 km. This high resolution is necessary for the analysis of mesoscale atmospheric phenomena like thunderstorms and their cell tracking (e.g. with TITAN). There exist higher spatially resolved models (e.g. COSMO), but the high temporal resolution is of particular importance for the research in this master thesis with Lagranto.

From the two nested WRF model domains, only the model output from the (smaller-scale) inner domain is used for the analysis ((3.70°E, 43.85°N), (13.81°E, 49.49°N); see extent of Figure 1.0.1). The WRF model data contains close to 200 different variables (see Table 1 for a selection) in a 4D grid (x, y, z and t) and on 50 model levels. The WRF simulations, with external forcing of the ECMWF operational analysis, are made for May 2018 and also for climate conditions at the end of the century, by following a RPC8.5 scenario (IPCC, 2013). These future simulations were implemented by the method of Schär et al. (1996). In their paper, Schär et al. (1996) present a methodology for generating surrogate climate change scenarios with a regional climate model. The idea behind this simple, but dynamically consistent methodology, is to separate the external dynamic from the thermodynamic forcing. Thermodynamic forcing is modified by a temperature increase according to climate change scenarios and a specification of the relative humidity (hereafter RH) values, which implies a change of the atmospheric water vapour content. The implementation of these modifications is simple, and the system's characteristic dynamic and thermodynamic balances are preserved (Schär et al., 1996). In the present master thesis, the WRF simulations contain a 5-degree higher temperature and 10% less RH, which are average values for the climate change by the end of the 21st century in an RPC8.5 scenario.

4 Methods

The methods section of this master thesis explains how the case studies were conducted and how the pre-storm environments of all thunderstorms in May 2018 and end of the century climate conditions were analysed.

4.1 Case Studies

This study follows an ingredients-based methodology after Doswell et al. (1996), who developed an approach to forecasting the potential for storms to produce flash floods. The idea behind their approach is to determine basic ingredients (atmospheric conditions and processes) of these extreme weather events and allocate the relative importance of each basic ingredient to the future occurrence of such an event. In this master thesis, however, the procedure of Doswell et al. (1996) is implemented in reverse order. In contrast to their approach, the event (a thunderstorm in this case) has already occurred, and the goal is to determine the basic ingredients (atmospheric conditions and processes) required to initiate a thunderstorm.

Hence, important variables for the initiation of thunderstorms (see Table 1 for an incomplete list of available variables) are investigated in this thesis from a Eulerian and a Lagrangian point of view. The Eularian investigation of these variables is conducted based on generated analysis tools like horizontal maps, vertical cross-sections, pseudo-soundings, and maps of the variables' temporal evolution at a specified location.

Table 1: Variables and their corresponding units for the investigation of thunderstorm initiation:

Variable	**Units**
Convective Available Potential Energy (CAPE)	Jkg^{-1}
Convective Inhibition (CIN)	Jkg^{-1}
Divergence	$10^{-3}s^{-1}$
Equivalent Potential Temperature (Theta-E)	K
Horizontal Wind Direction	$^{\circ}$
Horizontal Wind Speed	ms^{-1}
Reflectivity	dBZ
Relative Humidity (RH)	%
Temperature @ 2 m	K
Updraft	ms^{-1}
Vertical Motion (Omega)	Pas^{-1}
Vertical Wind Shear 500-850 hPa	ms^{-1}
Water Vapor Mixing Ratio (WVMR)	gkg^{-1}

Before changing to Lagrangian perspective, the thunderstorm initiation locations need to be defined in order to specify the starting locations of the trajectories. This definition of the initiation locations is based on the data output from TITAN. TITAN identified and tracked thunderstorms in the WRF model data

from May 2018, whose reflectivity values exceeded the threshold of 39 dBZ (manually set after sensitivity analysis). The TITAN locations of the thunderstorms are then used for tracing with Lagranto (Wernli & Davies, 1997), one of many different Lagrangian analysis tools available for atmospheric research. They all numerically solve the following trajectory equation:

$$\frac{Dx}{Dt} = u(x)$$

"where x = (λ, ϕ, p) is the position vector in geographical coordinates and u = (u, v, ω) the 3-D wind vector" (Sprenger & Wernli, 2015, p. 2569). By solving this equation, trajectories of air parcels can be calculated backwards in time. This master thesis uses the second version of Lagranto (Sprenger & Wernli, 2015). The starting points for Lagranto are chosen at the thunderstorm initiation location and in its surroundings (8 points with 0.05° spatial distance in each direction from initiation location, see e.g. Figure 1, Appendix). In addition, by starting from the same location, trajectories are calculated starting 30 minutes before and after the thunderstorm initiated (investigation of the pre- and post-storm environment). Based on these varying starting times, the trajectory analysis can then be divided into three stages: before, during and after the initiation.

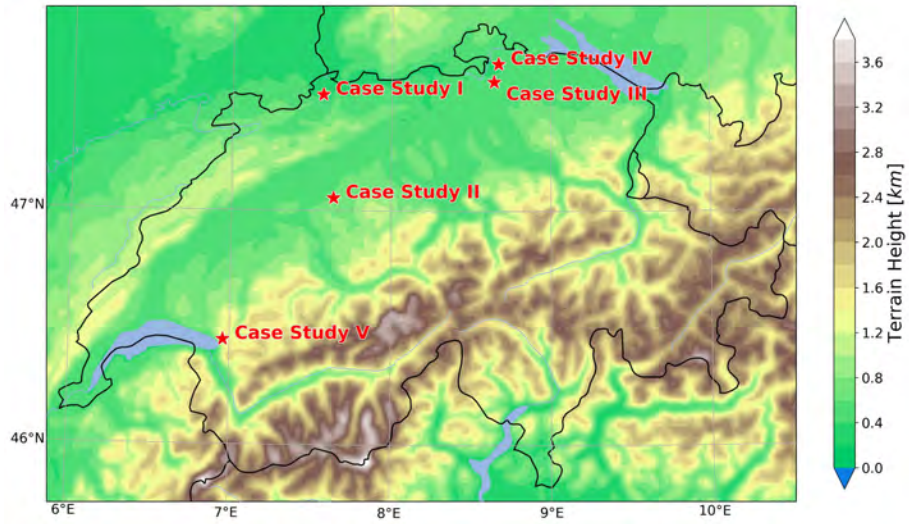

Figure 4.1.1: Location of the selected case studies in Switzerland (for selection criteria see 4.1 Case Studies) sorted from 'Case Study I' to 'Case Study V' (highest to lowest maximum reflectivity value). The background represents the terrain height [km] derived from the WRF (ARW) model.

The vertical starting points of the trajectories are chosen from the entire air column (surface up to approx. tropopause at 10 km), and from height levels that are equal in distance to each other (100 m vertical distance). The calculated trajectories can be afterwards separated according to a specific height range (e.g. surface up to 2.5 km height) regarding the respective stratification of the atmosphere. Once the spatial and temporal starting points are defined, one can choose the variables of interest which are traced along the trajectories. Variables of interest in this master thesis are height, water vapour mixing ratio (hereafter WVMR), updraft and equivalent potential temperature (hereafter Theta-E). The selection of the variables is chosen accordingly for the investigation of the basic ingredients of thunderstorm initiation (see 1.1 State of Knowledge): WVMR for determining a substantial amount of ground level moisture, Theta-E for assessing a conditional instability (and moisture content) and updraft, as well as height and Theta-E, for identifying the triggering process. The Lagranto outputs are coordinates of the computed trajectories and that output gives us information about the development of different variables along the trajectories that were traced. Afterwards, based on the Eulerian analysis of variables and Lagrangian

analysis of trajectories, the conditions and processes for thunderstorm initiation can be interpreted. This procedure is conducted for five case studies (i.e. individual model-based thunderstorms in May 2018 in Switzerland).

The case studies are identified based on the following criteria: First, the thunderstorms needed to last longer than 10 minutes. This should eliminate short-lived cells (so-called 'popcorn' cells). Second, only thunderstorms without 'parents' were selected. This means, that they did not originate through merging or splitting of earlier thunderstorms. Third, the thunderstorms with the highest maximum reflectivity values were selected. From these storms, the time step of the first detection was taken as the initiation time of the respective thunderstorm. Lastly, the five thunderstorms initiated over Switzerland with the highest maximum reflectivity values were picked for the in-depth case study analysis (see Figure 4.1.1 for their location).

4.2 Pre-Storm Environments of All Thunderstorms

In a further step, the atmospheric conditions for the whole month of May 2018 are of interest. The pre-storm environments of all May 2018 thunderstorms are researched with another analysis tool. This tool combines the thunderstorm information of the TITAN data output with the variables from the WRF data. In the preprocessing of the TITAN output data conducted at the beginning, only tracked thunderstorm were selected with a duration longer than 10 minutes and an initiation location over Switzerland (blue plus signs in Figure 4.2.2 with extent of (5.90°E, 45.75°N), (10.50°E, 47.85°N)). Second, for each initiation in the TITAN output data, four 30 minutes time steps are calculated. This two hour temporal evolution before the thunderstorm initiation builds the basis for collecting the variables in the WRF data in the following third step. In this step, for the initiation time and each time step before, the variables are extracted at the initiation location. Based on this extraction for each initiation, the mean, 10th and 90th percentiles are calculated in a last step before the visualisation part.

This combination technique of TITAN and WRF data reveals new details regarding the temporal evolution of different variables in the pre-storm environment of all thunderstorms occurred in that time period. The following important variables for thunderstorm initiation were extracted from the WRF data: CAPE, CIN, WVMR at 850 hPa, Theta-E at 850 hPa, horizontal wind divergence at 850 hPa, updraft and

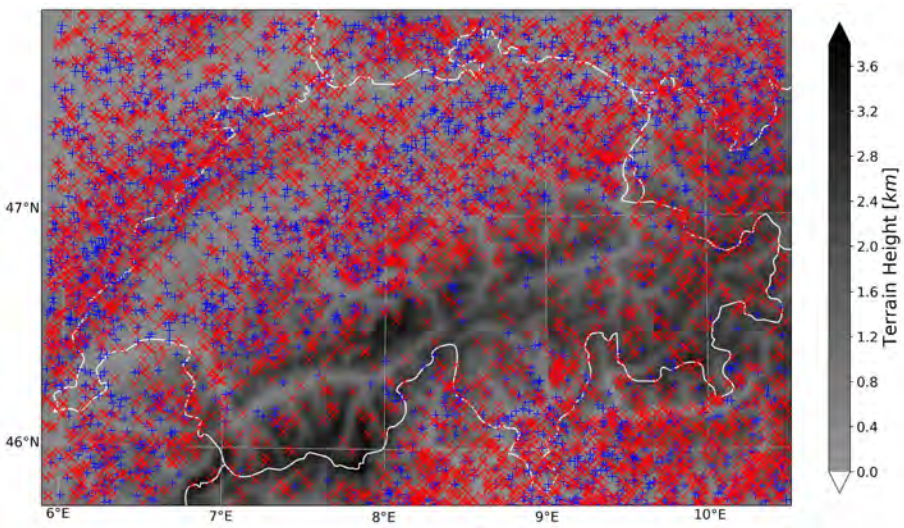

Figure 4.2.2: Locations of thunderstorm initiations tracked by TITAN for May 2018 (blue plus signs) and for end of the century climate conditions (red crosses). The background represents the terrain height [km] derived from the WRF (ARW) model.

three kinds of vertical wind shear 500-850 hPa (see Table 1). Based on the temporal evolution information of these variables and their magnitudes, inferences can be drawn about the general atmospheric patterns of this particular month.

The same approach is applied to the surrogate climate change model data for end of the century climate conditions (see 3 Data). Based on the TITAN output, 4311 thunderstorm initiations can be identified in these climate conditions (see Figure 4.2.2, red crosses). In May 2018, the identical selection of thunderstorms revealed only 2686 thunderstorm initiations (see Figure 4.2.2, blue plus signs). The locations of these initiations lie the basis for the analysis of the pre-storm environments of all thunderstorms in end of the century climate conditions. Afterwards, a comparison is conducted of the two analyses with data from May 2018 and end of the century climate conditions. Consequently, statements can be made about how the thunderstorm initiation conditions may change in future climate conditions.

5 Results

This section presents the results for five case studies and the investigation of their basic ingredients for thunderstorm initiation along with an analysis of the pre-storm environments of all thunderstorms in May 2018 and in end of the century climate conditions at the end.

5.1 Case Study I

The thunderstorm studied in this case study has the highest maximum reflectivity value of all five case studies (58.4 dBZ), while matching the selection criteria (see 4.1 Case Studies). The initiation of this

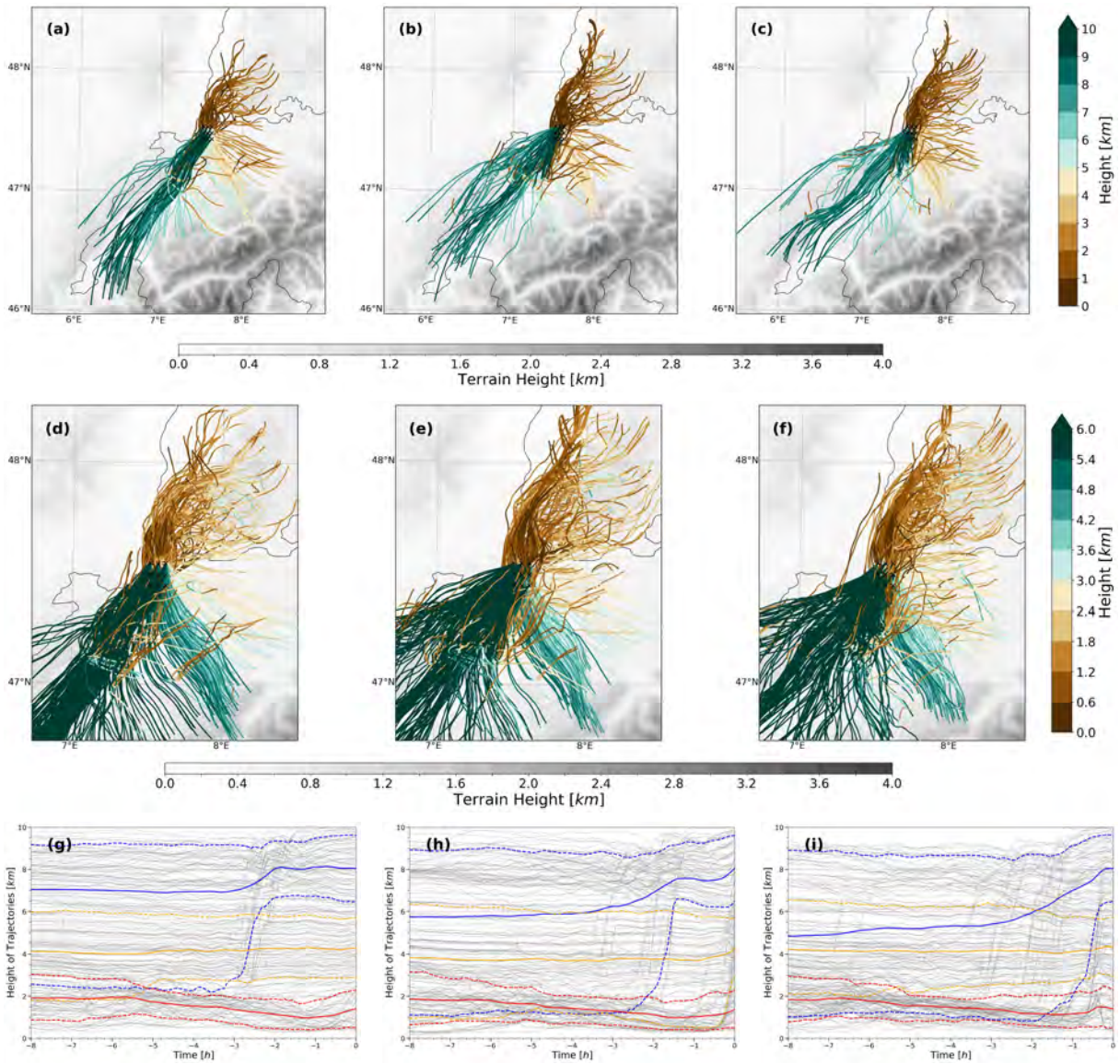

Figure 5.1.1: Height [km] along 8 hours backwards calculated trajectories started 30 minutes before (left), during (middle) and 30 minutes after (right column) thunderstorm initiation (22.05.2018 - 17:00 UTC). The starting points of the trajectories consist of the initiation location (7.56971° E, 47.4961° N) and 8 starting points 0.05° in each direction (crosses). The background of the panels in the upper two rows represents the terrain height [km] for the area of northern Switzerland. (a)-(c): Horizontal maps of trajectories with starting heights every 100 m from surface (SFC) up to 10 km (every 5th trajectories is plotted). (d)-(f): Horizontal maps of trajectories with starting heights every 100 m from surface up to 6 km (every 2nd trajectories is plotted). The figures show a smaller spatial extent, compared to the figures of the first row. (g)-(i): Temporal evolution along trajectories separated in three categories corresponding to their starting height: SFC up to 2.5 km (red), 2.5 up to 6 km (orange) and 6 up to 10 km (blue) with solid (dashed) lines for mean (10th and 90th percentile).

thunderstorm was on 22.05.2018 at 17:00 UTC over Northwestern Switzerland (7.56971°E, 47.4961°N; see Figure 4.1.1 for case study location). Figure 1 (Appendix) contains spatial information regarding the thunderstorm initiation location, the vertical cross-section path and the extent of the figures in the subsequent case study analysis.

The eight hours backwards calculated trajectories are presented in Figure 5.1.1 with their altitude indicated by colours (Figure 5.1.1a-f). Each column represents a different starting time: 30 minutes before (left), during (middle) and 30 minutes after the initiation (right). On the first row (Figure 5.1.1a-c), the trajectories with starting heights from the surface up to 10 km are shown (if they stayed in the domain). The panels of the second row (Figure 5.1.1d-f) provide a closer look on the trajectories from the surface up to 6 km (in each case study this upper threshold is different according to the particular atmospheric stratification, see 4.1 Case Studies). Besides the initiation location, I started the trajectories from eight points (crosses) in the surrounding of the thunderstorm initiation (see Figure 1, Appendix). Finally, the panels in the third row (Figure 5.1.1g-i) provide another perspective on the calculated trajectories by leaving out the spatial dimension and focusing only on the temporal evolution of the respective variable. For the analysis of different atmospheric layers, the trajectories are divided into categories in accordance to their starting heights (red, orange and blue). For the comparison of these categories, the mean values of the respective trajectories of each category (coloured solid lines) serve as appropriate indicators.

The trajectories approach the initiation location from different directions (Figure 5.1.1a). At lower altitudes (SFC up to 2.5 km, brown) they arrive from the north, while at higher altitude they approach from southeast (2.5 up to 6 km, light brown/green) to southwest (6 up to 10 km, green). This pattern holds during (Figure 5.1.1b) and after the initiation (Figure 5.1.1c), except a slightly westward shift of the southwest approaching trajectories. During the initiation (Figure 5.1.1e), some trajectories from the north have lower altitude levels (from 1-2 to 0-1 km) compared to 30 minutes before (Figure 5.1.1d) and after (Figure 5.1.1f) the thunderstorm initiation. After the initiation (Figure 5.1.1f), the trajectories do not anymore approach only from the previously described directions, but they are arriving from almost every direction to the initiation area.

On the temporal evolution panels (Figure 5.1.1g-i), I could detect a descending (ascending) tendency of the lower (higher) trajectories in red (blue). The mean of the trajectories from SFC up to 2.5 km (red) descends from 2 km (6 hours before initiation) to 1 km until 1 hour before the thunderstorm initiation (Figure 5.1.1g). On the other hand, the mean of the highest trajectories (6 up to 10 km, blue) rises

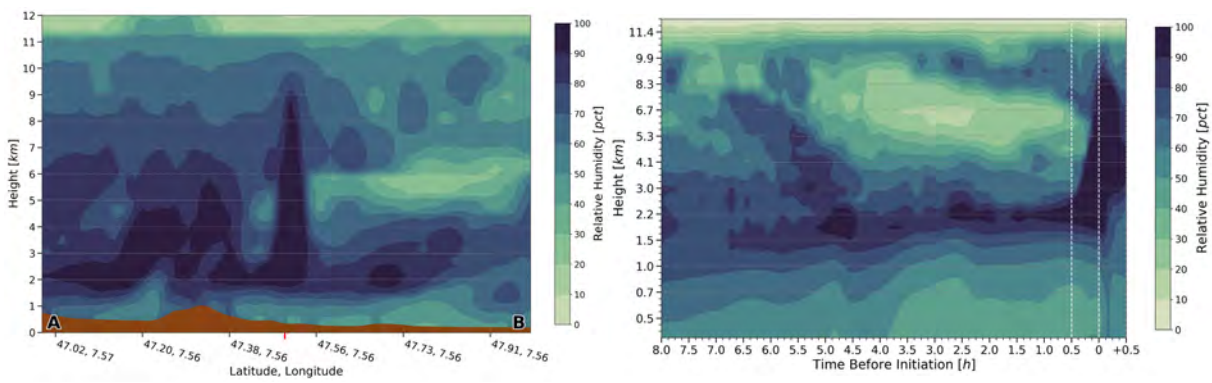

Figure 5.1.2: Left: Vertical cross-section (VCS) of relative humidity (RH) [%] on 22.05.2018 at 17:00 UTC. VCS in north-south direction with initiation location indicated by red tick on x-axis, starts at A (7.5697° E, 46.9961° N) and ends at B (7.5697° E, 47.9961° N). Right: Temporal evolution of RH [%] at the location of initiation (7.56971° E, 47.4961° N) and its surroundings until 8 hours before the thunderstorm initiation (see above). Vertical dashed lines indicate 30 minutes before, during and after the initiation time (starting times of trajectories).

abruptly in only 1 hour (-3 to -2 hours) from 7 km to 8 km altitude (Figure 5.1.1g). During the initiation (Figure 5.1.1h), all the mean values rise shortly before the initiation time (0 hours on x-axis rightmost). But the higher starting trajectories already begin 4 hours before the initiation their ascent at 6 km altitude. This ascent reaches its peak at 7.5 km altitude 1.5 hours before thunderstorm initiation (Figure 5.1.1h). Afterwards, this ascending tendency is stabilised. The same pattern after the strong ascent can be detected along the highest trajectories (6 up to 10 km) 30 minutes before (Figure 5.1.1g) and after the thunderstorm initiation (Figure 5.1.1i).

With the VCS of RH (see Figure 5.1.2, left), I can infer the presence of moisture in the different atmospheric layers. Besides maximum RH values (90-100 %) of the thunderstorm cell (above the red tick on x-axis), the atmosphere has north of the initiation location (from red tick towards B) a higher percentage of RH from 1.5 to 4 km altitude (70-100 %), compared to the layers at ground level (SFC up to 1.5 km, 40-80 %) and aloft (4 up to 7 km, 20-80 %). Further, I calculated the temporal evolution of RH (see Figure 5.1.2, right). This figure presents the evolution of RH in the atmosphere above the initiation location and its surroundings over eight hours before the thunderstorm initiation (mean of the values from initiation location and the trajectory starting locations, see Figure 1). The vertical dashed lines

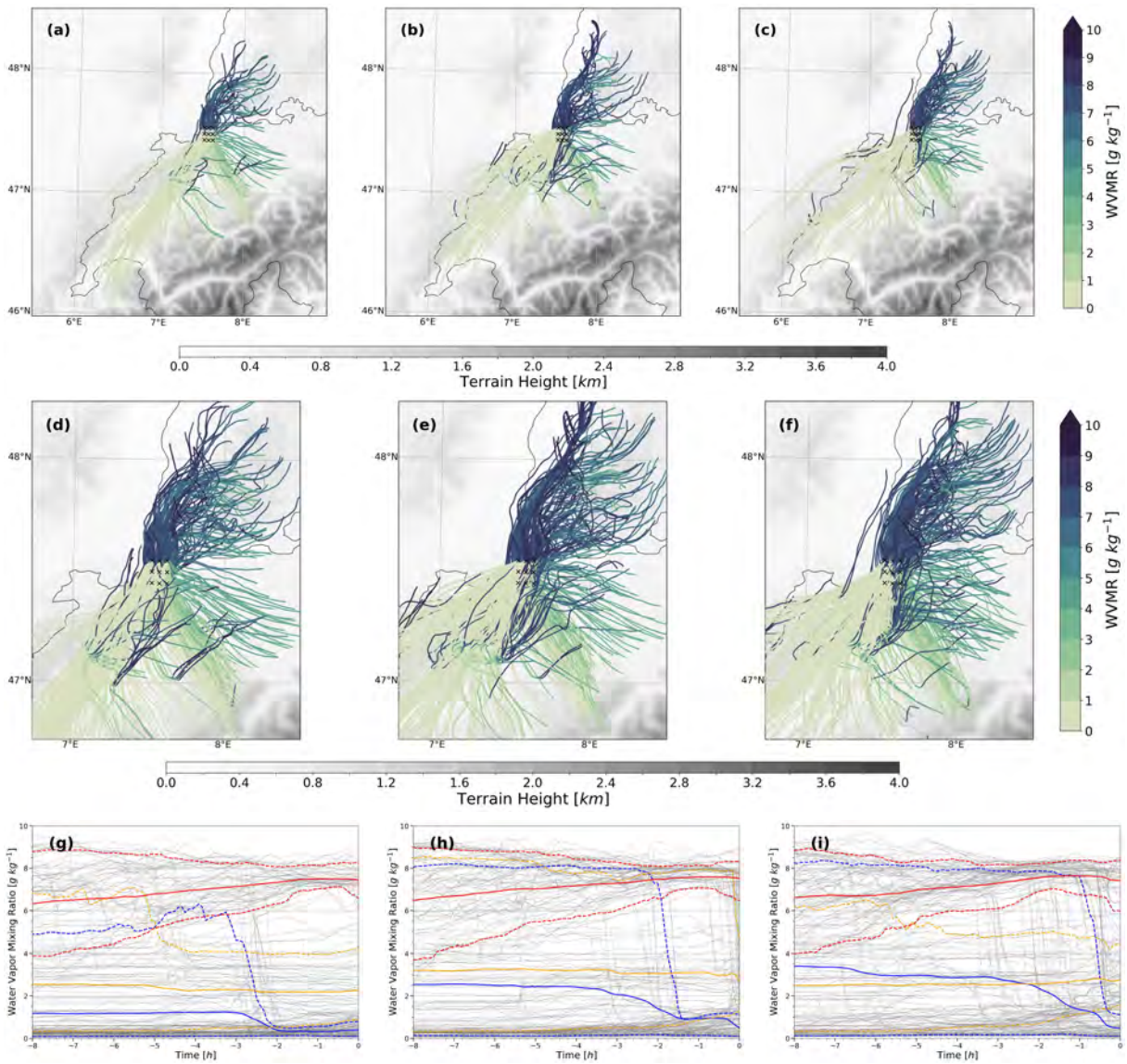

Figure 5.1.3: Same as Figure 5.1.1, but for water vapour mixing ratio (WVMR) [g kg^{-1}].

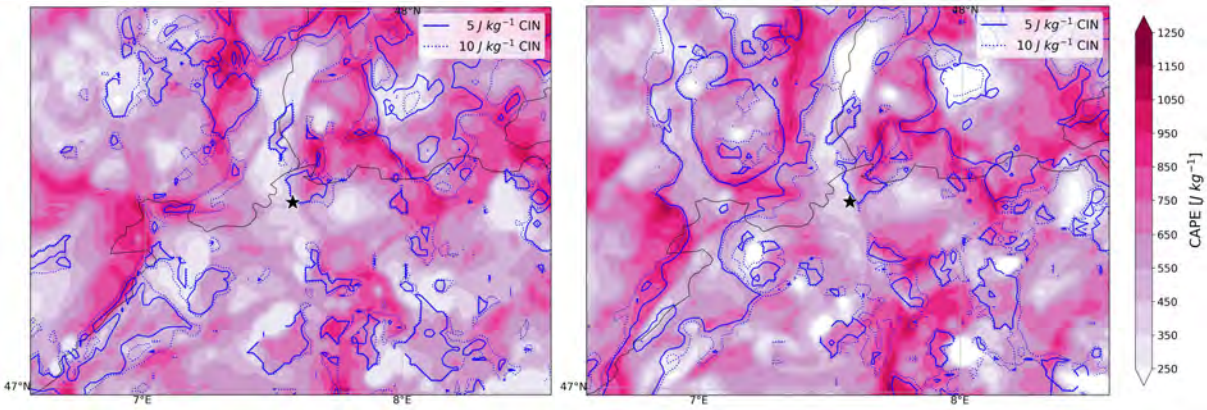

Figure 5.1.4: Horizontal map of Convective Available Potential Energy (CAPE) [J kg^{-1}] and 5 and 10 J kg^{-1} contour lines (solid and dotted blue) of Convective Inhibition (CIN) [J kg^{-1}] on 22.05.2018 at initiation time 17:00 UTC (left) and 30 minutes before initiation 16:30 UTC (right) with initiation location (7.56971° E, 47.4961° N, asterisk) for northern Switzerland.

indicate the starting times of the trajectories calculated with Lagranto. Based on the temporal evolution figure, I can infer that, approximately 4 hours before the initiation, the RH has decreased in the PBL (SFC up to 1.5 km, 50-80 to 40-70%) and tropospheric layers above 4.1 and up to 9.9 km altitude (20-90 to 0-50 %). At the same time, in the mid-troposphere from 1.5 to 3 km altitude RH values increased and reached maximum values (90-100 %) at 2.2 km altitude.

The traced air parcels with their WVMR are shown in Figure 5.1.3. These trajectories enable the assessment of moisture content in the atmosphere from a Lagrangian perspective. Trajectories with high amounts of water vapour (5-10 g kg^{-1}) are approaching the initiation location from the northeast, while drier trajectories originate from southeast (2-5 g kg^{-1}) to southwest (0-2 g kg^{-1}). This separation of the trajectories is coupled to the height of the trajectories (see Figure 5.1.1). After the thunderstorm initiation (Figure 5.1.3f), some trajectories with higher starting levels carry more moisture (from 0-2 to

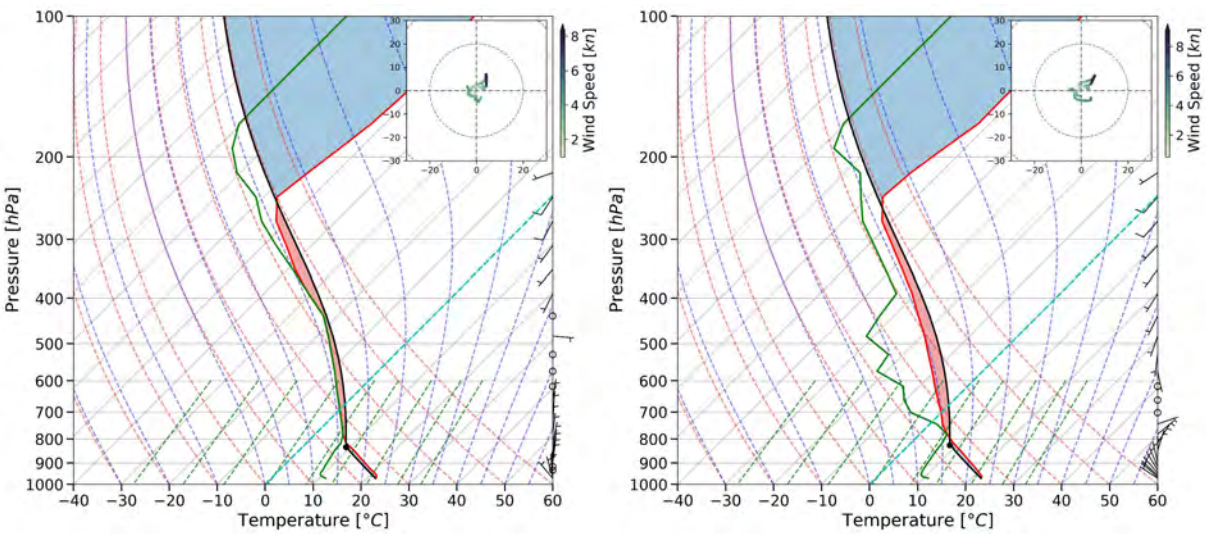

Figure 5.1.5: Skew T-log p diagram at location of initiation (7.56971° E, 47.4961° N) on 22.05.2018 at initiation time 17:00 UTC (left) and 30 minutes before initiation 16:30 UTC (right). The figure shows isotherms (skewed grey gridlines and marked zero degree line in turquoise) and isobars (horizontal grey gridlines), as well as lines of equal saturation mixing ratio (isohumes, green dashed line), potential temperature (dry adiabats, red dashed line) and pseudo-equivalent potential temperature (moist adiabats, blue dashed line). Included are the simulated absolute temperature (red line), dewpoint temperature (green line), the calculated path of a vertically rising air parcel (black line), and the lifted condensation level (LCL, black dot). The inset in the top right corner of the figure shows a hodograph, with direction line path and colored wind speed [kn]. The wind speed [kn] and direction are also presented with the wind barbs along the right y-axis.

4-8 g kg^{-1}) compared to the time steps before (Figure 5.1.3d-e). This humidification of the upper level trajectories (6 up to 10 km) is also detectable on the temporal evolution figures (Figure 5.1.3g-i). Eight hours before thunderstorm initiation, the mean of these trajectories (6 up to 10 km, blue) increases from 1 g kg^{-1} before the initiation (Figure 5.1.3g), to 2.5 g kg^{-1} during the initiation (Figure 5.1.3h) and up to 3.5 g kg^{-1} after the initiation (Figure 5.1.3i). Furthermore, the WVMR along the trajectories slightly increases (6.5 to 7.5 g kg^{-1}) in the lower troposphere (SFC up to 2.5 km; red solid) and decreases (from the aforementioned differing starting values to 0.5 g kg^{-1}) in the upper troposphere (6 up to 10 km; blue solid) by approaching the starting time (0 hours rightmost). During thunderstorm initiation (Figure 5.1.3h), the mean (solid lines) decreases shortly before the initiation at all height levels.

Figure 5.1.4 shows horizontal maps of Convective Available Potential Energy (CAPE, coloured) and Convective Inhibition (CIN, contours) at the time of initiation (left) and 30 minutes before (right). At the initiation location (asterisk), CIN is non-zero (>10 J kg^{-1}) and CAPE between 250 and 350 J kg^{-1} half an hour before thunderstorm initiation (see Figure 5.1.4, right). Until the initiation (see Figure 5.1.4, left), CAPE has increased (350-450 J kg^{-1}) and CIN is still bigger than 10 J kg^{-1}, but the 5 and 10 J kg^{-1} contour lines (solid and dotted blue) are located closer to the initiation location.

How stable the atmospheric stratification is can be further assessed with a skew T-log p diagram (see Figure 5.1.5), derived from a pseudo-sounding. Here, CAPE (CIN) is calculated and presented in this diagram with a red (blue) shade area. The before-mentioned increase in CAPE was also visible in the analysis of the pre-storm environment based on skew T-log p diagrams. CAPE started to increase half an hour before the initiation (see Figure 5.1.5, right) and then decreased to its value at the time of thunderstorm initiation (see Figure 5.1.5, left). Attention should be paid to the area below the CAPE shade, where the CIN area has slightly decreased from 30 minutes before initiation (see Figure 5.1.5, right) until the thunderstorm initiation (see Figure 5.1.5, left). In addition 30 minutes before the initiation, I can identify an conditional unstable layer from the Lifted Condensation Level (hereafter LCL, black dot) up to approximately 500 hPa (see Figure 5.1.5, right). The dry layer in the mid-troposphere (700 up to 450 hPa, Figure 5.1.5, right) gets saturated until the time of initiation (see Figure 5.1.5, left). The wind barbs along the right y-axis and the hodograph indicate an directional wind shear in the troposphere from the surface up to 750 hPa (see Figure 5.1.5, right), which will be weaker at time of thunderstorm initiation (see Figure 5.1.5, left).

In the VCS of Figure 5.1.6, the Theta-E stratification consists of higher Theta-E values in the lower

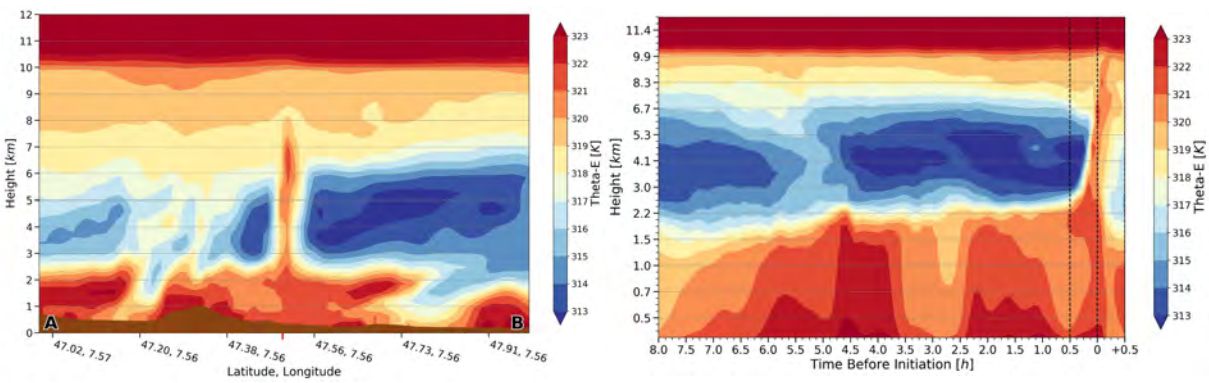

Figure 5.1.6: Left: Vertical cross-section (VCS) of equivalent potential temperature (Theta-E) [K] on 22.05.2018 at 17:00 UTC. VCS in north-south direction with initiation location indicated by red tick on x-axis, starts at A (7.5697° E, 46.9961° N) and ends at B (7.5697° E, 47.9961° N). Right: Temporal evolution of Theta-E [K] at the location of initiation (7.56971° E, 47.4961° N) and its surroundings until 8 hours before the thunderstorm initiation (22.05.2018 - 17:00 UTC). Vertical dashed lines indicate 30 minutes before, during and after the initiation time (starting times of trajectories).

troposphere (320-323 K, SFC up to 2 km), compared to the mid-troposphere (313-316 K, 3 up to 6 km). In addition, the temporal evolution of Theta-E (see Figure 5.1.6, right) reveals an intensification of this Theta-E gradient from 8 hours to half an hour before the thunderstorm initiation. The trajectories of Theta-E values (see Figure 5.1.7) indicate the origin of the air for the before mentioned layers. The trajectories approaching the initiation area from southwest in the upper troposphere have higher Theta-E values (324-325 K) than their lower counterparts (320-322 K) approaching from the north (especially before the initiation, Figure 5.1.7a and Figure 5.1.7d). The temporal evolution of Theta-E, shown in Figure 5.1.7g), enable also the detection of the Theta-E gradient intensification shortly before the thunderstorm initiation by comparing the means of the different layers in the last 2 hours.

The analysis of the maximum updraft values along the trajectories (see Figure 3, Appendix) reveal a strong updraft signal along the trajectories approaching from southwest (Figure 3a). This concentrated signal of strong updraft values emerge in the following two time steps closer to the initiation location (Figure 3b-c). During the initiation (Figure 3b), more trajectories experience updrafts, which are stronger and further spatially distant from the initiation location (in the west and east). By focusing on the lower starting trajectories up to 6 km altitude (Figure 3e), the initiation signal is well detectable at the location

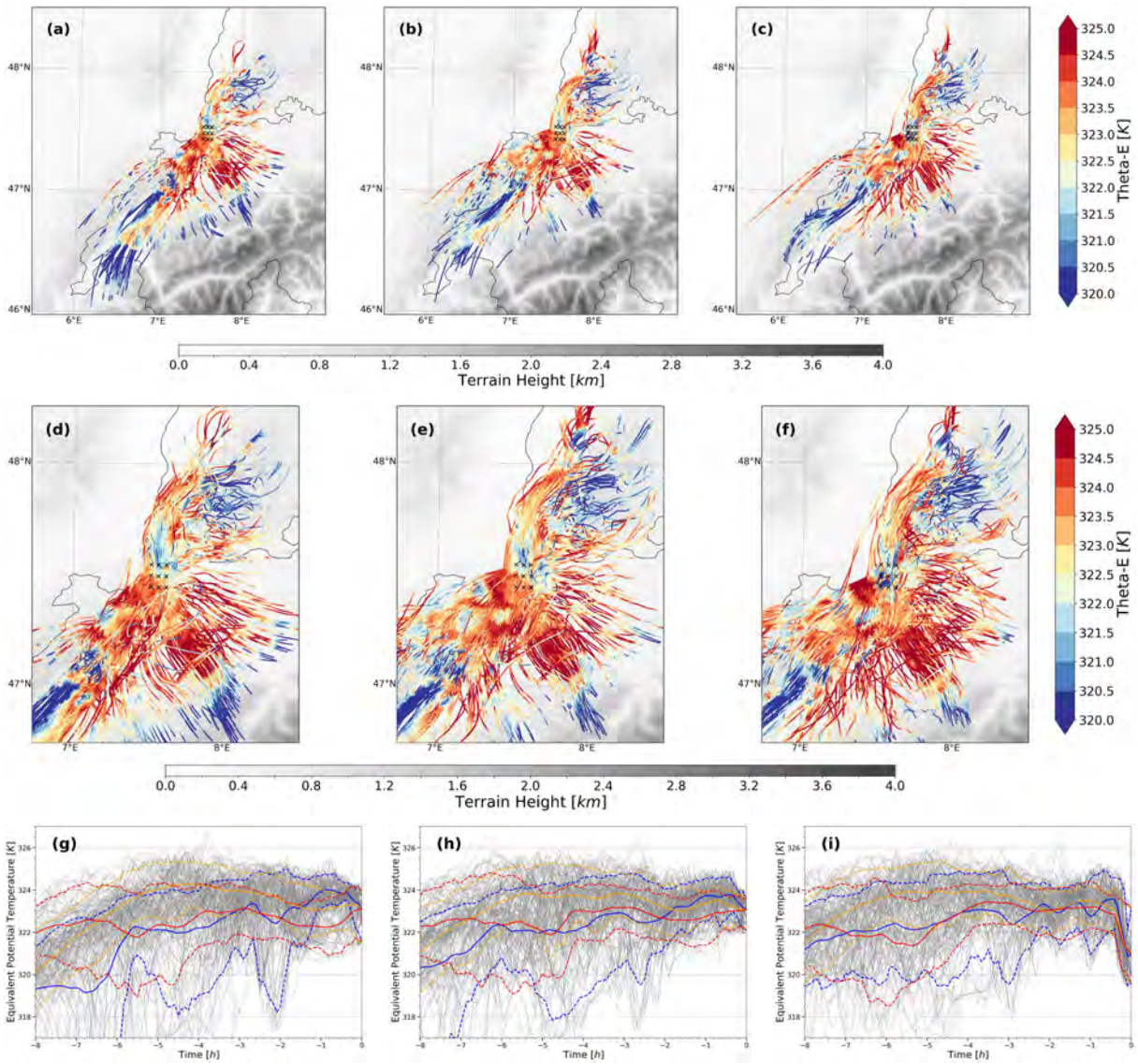

Figure 5.1.7: Same as Figure 5.1.1, but for equivalent potential temperature (Theta-E) [K].

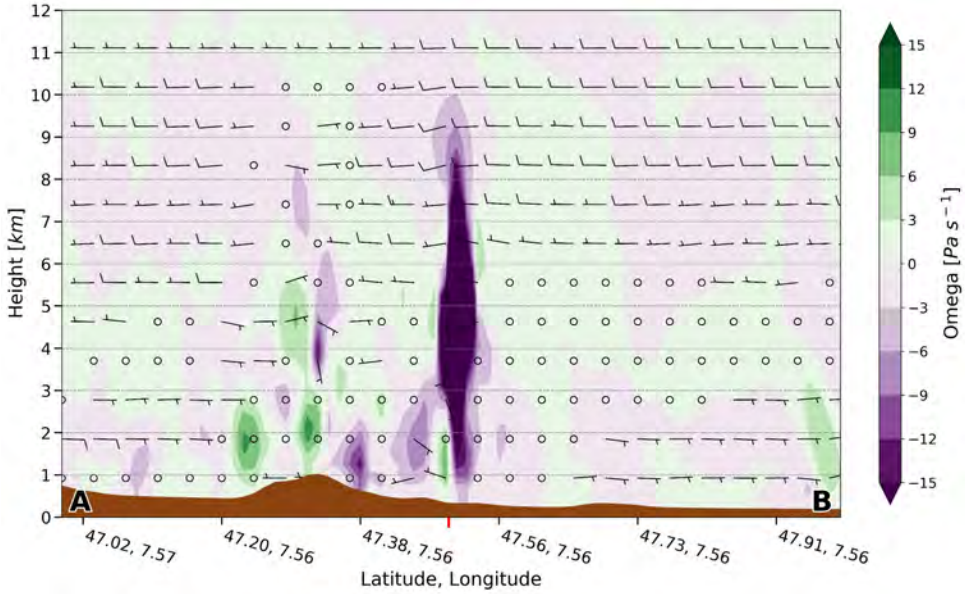

Figure 5.1.8: Vertical cross-section (VCS) of vertical motion (Omega) [Pas^{-1}] on 22.05.2018 at 17:00 UTC. VCS in north-south direction with initiation location indicated by red tick on x-axis, starts at A (7.5697° E, 46.9961° N) and ends at B (7.5697° E, 47.9961° N).

of initiation. After the initiation (Figure 3f), updrafts occur on a larger scale and slightly more in the eastern part of the initiation area. Additionally, the trajectories with these signals change their direction of approach from southeast (Figure 3e) to east (Figure 3f). The temporal evolution panels in the bottom row (Figure 3g-i) show as well the movement of the strong updraft signal closer to the initiation time (shift of the peak towards the right in the blue mean). The updraft signal of the thunderstorm initiation is equally strong in all atmospheric layers (Figure 3h).

The location of thunderstorm initiation lies in a small depression north of a low-rise hill range (see Figure 5.1.9, left). On the VCS of Omega (see Figure 5.1.8), descending winds can be detected along the southern flank of the hill. Further, Figure 5.1.9 (right) indicates at the initiation location a northerly wind blowing at 850 hPa and on the same altitude a strong signal of negative divergence values (see Figure 5.1.9, left).

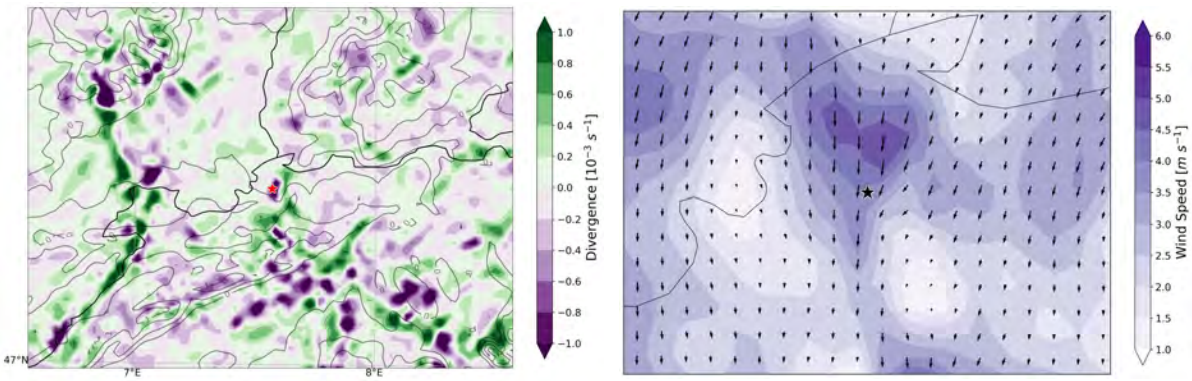

Figure 5.1.9: Left: Horizontal map of wind divergence @ 850 hPa [10^{-3} s^{-1}] on 22.05.2018 at 17:00 UTC with initiation location (7.56971° E, 47.4961° N, asterisk). The contour lines indicate the terrain height [km] for the area of northern Switzerland. Right: Horizontal map of wind speed [m s^{-1}] and direction @ 850 hPa on time and location of initiation (see above) for northern Switzerland.

Hence in the analysis of this case study, I could find a separation in the direction of approach from north to southeast up to southwest with increasing starting height of the trajectories. Further, I identified

a layer of high RH values (90-100 %) in the mid-troposphere, which was located above (40-80 %) and beneath (20-80 %) layers of lower RH values (i.e. potential instability). Based on the calculated WVMR along the trajectories, the moisture was transported from the north to the initiation location. Until the the initiation, CAPE values were slightly increasing (250-350 to 350-450 J kg^{-1}) and CIN was non-zero (>10 J kg^{-1}). The skew T-log p diagram revealed a conditional unstable layer (LCL up to 500 hPa) half an hour before the initiation. Further, the inversion of the vertical Theta-E gradient indicates a potential instability in the atmosphere. The low mid-tropospheric Theta-E values (313-316 K) originated from the trajectories approaching from the north. Finally, at the location of initiation in a small depression, northerly winds were blowing and the divergence values were strongly negative (<-1 10^{-3} s^{-1}).

Based on these results, the basic ingredients for thunderstorm initiation can be assessed. During the thunderstorm initiation, the analysis tools revealed an saturated atmosphere (high RH, 90-100 %) in the mid-troposphere (location of thunderstorm cell). Although, the RH in the boundary layer was lower (40-80 %), the approaching trajectories in these height levels carried a lot of moisture with them (high WVMR, 5-10 g kg^{-1}). With this ground-level moisture inflow from the north, water vapour was transported into the area of initiation. Combined with the already present substantial amount of mid-tropospheric moisture, I can infer that this basic ingredient is fulfilled.

Although the slight build up, CAPE was still small at the time of initiation (350-450 J kg^{-1}) and I would have expected higher values for the strongest thunderstorm of all case studies. But CIN was small too at least (>10 J kg^{-1}, area skew T-log p diagram small) and could not inhibit the initiation of the thunderstorm. Further, the environmental lapse rate indicated a conditional unstable layer (LCL up to 500 hPa) and vertical stratification of the Theta-E a potential instability before the initiation. The lower Theta-E values (313-316 K, 3 up to 6 km) located above the higher Theta-E values (320-323 K, SFC up to 2 km) lead to an inversion of the Theta-E gradient and a potential unstable atmospheric stratification. The low mid-tropospheric Theta-E originated from the trajectories on the lowest altitudes (SFC up to 2.5 km). This could be a sign for an ascent of the lowest trajectories to the mid-troposphere, where they would also be responsible for the moisture inflow. All these findings lead to the conclusion that the basic ingredient of a conditional instability was existing in atmosphere.

The trajectories approach from different directions with varying starting height, which infers a directional vertical wind shear present at the thunderstorm location. The wind barbs and hodograph on the skew T-log p diagram confirm this finding, where they indicate especially in the lower tropospheric layers a directional vertical wind shear. But the directional shear is not as pronounced as well as the differences in wind speed. This leads me to the conclusion, that the vertical wind shear did not play an important role in the initiation of this thunderstorm.

The location of initiation lies in a small depression north of a low-rise hill range and the prevailing winds at 850 hPa blew out of the north. This combination could lead to an ascending motion at the location of initiation due to the topography. This ascending motion is also confirmed by the calculated trajectories. At the same time, the near surface wind descends along the hill and results in convergence at the location of thunderstorm initiation. The combination of orographic-related forcing mechanisms and convergence is the most plausible instability triggering process for thunderstorm initiation in this case study.

5.2 Case Study II

The second strongest thunderstorm tracked by TITAN (max. reflectivity value of 57.9 dBZ) builds the subject of this case study. The initiation location (7.63891°E, 47.0546°N; see Figure 4.1.1 for case study location) lies close to the Napf region (Emmental Alps), where the thunderstorm initiated on 09.05.2018 at 14:05 UTC (see Figure 2, Appendix for more spatial information). Figure 5.2.1 shows the back trajectories coloured by their height level. The air parcels approach the initiation area (crosses) all from northwest to northeast (Figure 5.2.1a-f). This pattern changes from before to after the thunderstorm initiation (left to right column) by concentrating more to a northerly approach. Before the initiation (Figure 5.2.1d), the lowest trajectories (SFC up to 1.4 km) arrive to the initiation location from northwest, some individuals even more westerly. Air parcels on a little higher altitude (1.4 up to 4.2 km) move from northeast to

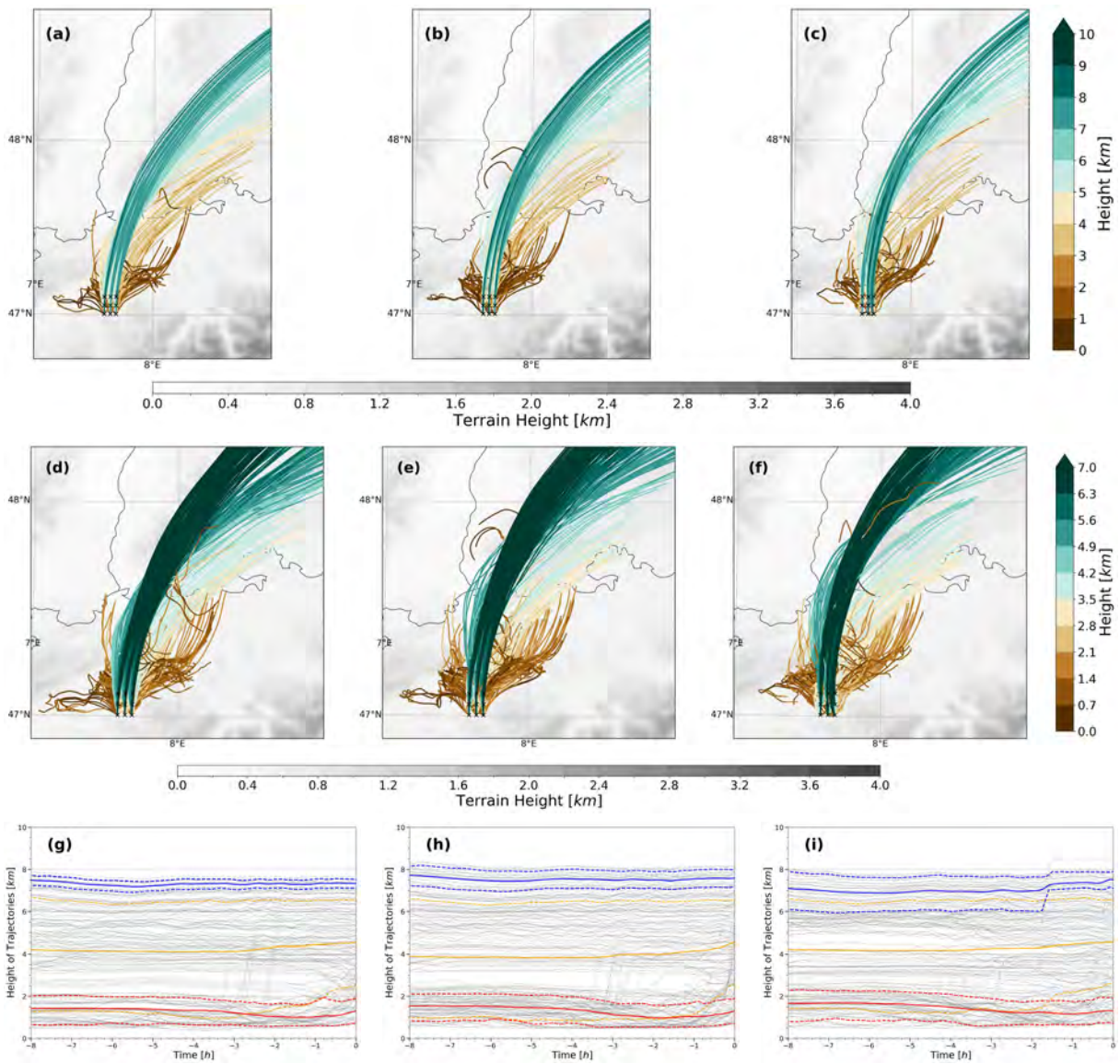

Figure 5.2.1: Height [km] along 8 hours backwards calculated trajectories started 30 minutes before (left), during (middle) and 30 minutes after (right column) thunderstorm initiation (09.05.2018 - 14:05 UTC). The starting points of the trajectories consist of the initiation location (7.63891° E, 47.0546° N) and 8 starting points 0.05° in each direction (crosses). The background of the panels in the upper two rows represents the terrain height [km] for the area of northern Switzerland. (a)-(c): Horizontal maps of trajectories with starting heights every 100 m from surface (SFC) up to 10 km (every 5th trajectories is plotted). (d)-(f): Horizontal maps of trajectories with starting heights every 100 m from surface up to 6 km (every 2nd trajectories is plotted). The figures show a smaller spatial extent, compared to the figures of the first row. (g)-(i): Temporal evolution along trajectories separated in three categories corresponding to their starting height: SFC up to 2 km (red), 2 up to 7 km (orange) and 7 up to 10 km (blue) with solid (dashed) lines for mean (10th and 90th percentile).

the area of initiation and the trajectories on the highest altitudes (4.2 up to 7 km) from the north. On the temporal evolution panels can be seen (Figure 5.2.1g-i), that mostly trajectories from the mid-troposphere (2 up to 7 km, orange) rise while approaching the initiation location. The ascent of these trajectories is most pronounced during the initiation of the thunderstorm. From 4 km altitude 3 hours before the initiation, the mean value rises to 4.5 km altitude until the thunderstorm initiation (Figure 5.2.1h). Concurrently, the trajectories in the lowest part of the atmosphere (SFC up to 2 km, red) are descending (from 1.5 to 1 km) until they slowly ascend again (from 1 to 1.25 km) in the last 2 hours before the initiation (Figure 5.2.1g-h).

The VCS of Figure 5.2.2 (left) reveals high RH values (90-100 %) over the initiation location (red tick on x-axis). In the mid-troposphere (higher than 5.5 km), there exists also some dry layers (0-30 %) on either side of the thunderstorm cell (more pronounced signal northwards of the initiation location, towards B). Until 6 hours before the initiation, there was maximum RH (90-100 %) present in the lower troposphere at the initiation locations and its surroundings (see Figure 5.2.2, right). From that point until the thunderstorm initiation, the atmospheric layers close to the surface (SFC up to 1.3 km) lost some moisture content and/or got warmer (lowering of RH values to 50-80 %). By looking at the WVMR along the trajectories (see Figure 5.2.3), a separation between the lower and higher trajectories is identifiable. The traced air parcels closer to the surface have a higher amount of water vapour (7-10 g kg^{-1}) compared to their counterparts in higher altitude (highest with 0-1 g kg^{-1}; see Figure 5.2.1 for height information). 30 minutes after the thunderstorm initiation (Figure 5.2.3f), the water vapour content along the lower trajectories has decreased (from 9-10 g kg^{-1} to 7-9 g kg^{-1}). This signal can also be detect in the in the comparison of the temporal evolution panels (Figure 5.2.3h-i). The trajectories with starting heights between SFC and 2 km (red) as well as 2 and 7 km (orange), have a lower amount of water vapour after the initiation (6.5 and 2.5 g kg^{-1} 8 hours before the initiation, Figure 5.2.3i) compared to the time during the thunderstorm initiation (6.75 and 3 g kg^{-1} 8 hours before the initiation, Figure 5.2.3h).

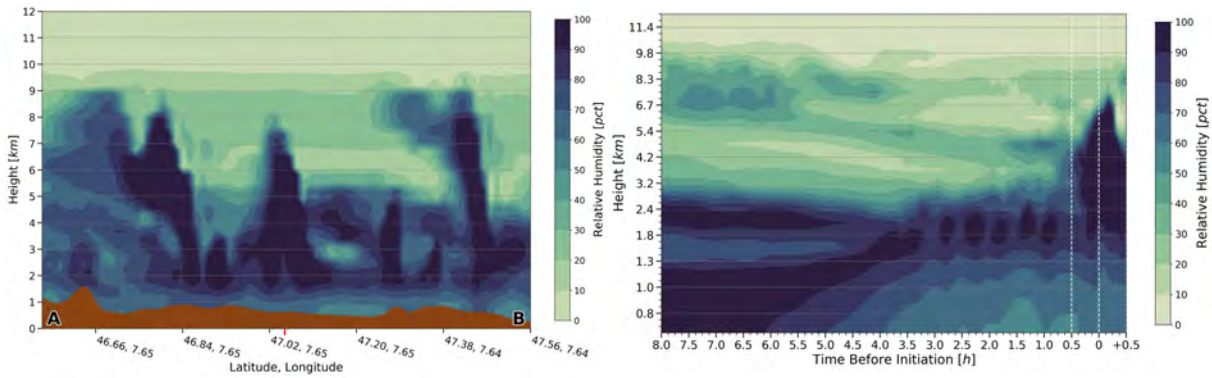

Figure 5.2.2: Left: Vertical cross-section (VCS) of relative humidity (RH) [%] on 09.05.2018 at 14:05 UTC. VCS in north-south direction with initiation location indicated by red tick on x-axis, starts at A (7.63891° E, 46.5546° N) and ends at B (7.63891° E, 47.5546° N). Right: Temporal evolution of RH [%] at the location of initiation (7.63891° E, 47.0546° N) and its surroundings until 8 hours before the thunderstorm initiation (see above). Vertical dashed lines indicate 30 minutes before, during and after the initiation time (starting times of trajectories).

For assessing the potential for convection in the atmosphere, Figure 5.2.4 shows CAPE and CIN for the time of thunderstorm initiation (left) and 30 minutes before the initiation (right). During the initiation of the thunderstorm (see Figure 5.2.4, left), CAPE was low (325-400 J kg^{-1}) and CIN higher than 10 J kg^{-1} (blue dotted contour line). Half an hour before (see Figure 5.2.4, right), CAPE was much higher (700-775 J kg^{-1}) and CIN below 5 J kg^{-1}. Consequently, CAPE has decreased, while CIN has built up values over 10 J kg^{-1} until the initiation. For the same time steps, Figure 5.2.5 shows the corresponding skew T-log p diagrams derived from pseudo-soundings. The decrease in CAPE (red area) and increase

in CIN (lower blue area) is eye-catching by comparing the situation 30 minutes before (see Figure 5.2.5, right) and during the initiation (see Figure 5.2.5, left). Further, drier atmospheric layers can be detected above 600 hPa, which got saturated up to 450 hPa until the thunderstorm initiation. Moreover, the wind barbs indicated a vertical wind shear in the PBL, which decreased until the thunderstorm initiation. Also the extent of the conditional unstable layer decreases from 30 minutes before (LCL up to 400 hPa) until the initiation of the thunderstorm (SFC up to 750 hPa and 500 up to 450 hPa).

In a following step, the stratification of Theta-E is assessed (see Figure 5.2.6). Although, at the time of initiation the influence of the thunderstorm cell on the vertical Theta-E stratification is already detectable and hence, Theta-E does not strongly change with height above the initiation location (red tick on x-axis in Figure 5.2.6, left). But the temporal evolution of Theta-E (see Figure 5.2.6, right) reveals another picture only half an hour before the thunderstorm initiation. At the initiation location and its surroundings, a strong vertical Theta-E gradient is detectable before and until 30 minutes the initiation. Theta-E is lower (310-313 K) in the mid-troposphere (2.4 up to 5.4 km) compared to the boundary layer (318-320 K, 0 up to 1.3 km). Figure 5.2.7a-f) shows Theta-E along the trajectories, where the gradual increase of the air parcels Theta-E is obvious (from 313 to 323 K), when they get closer to the initiation

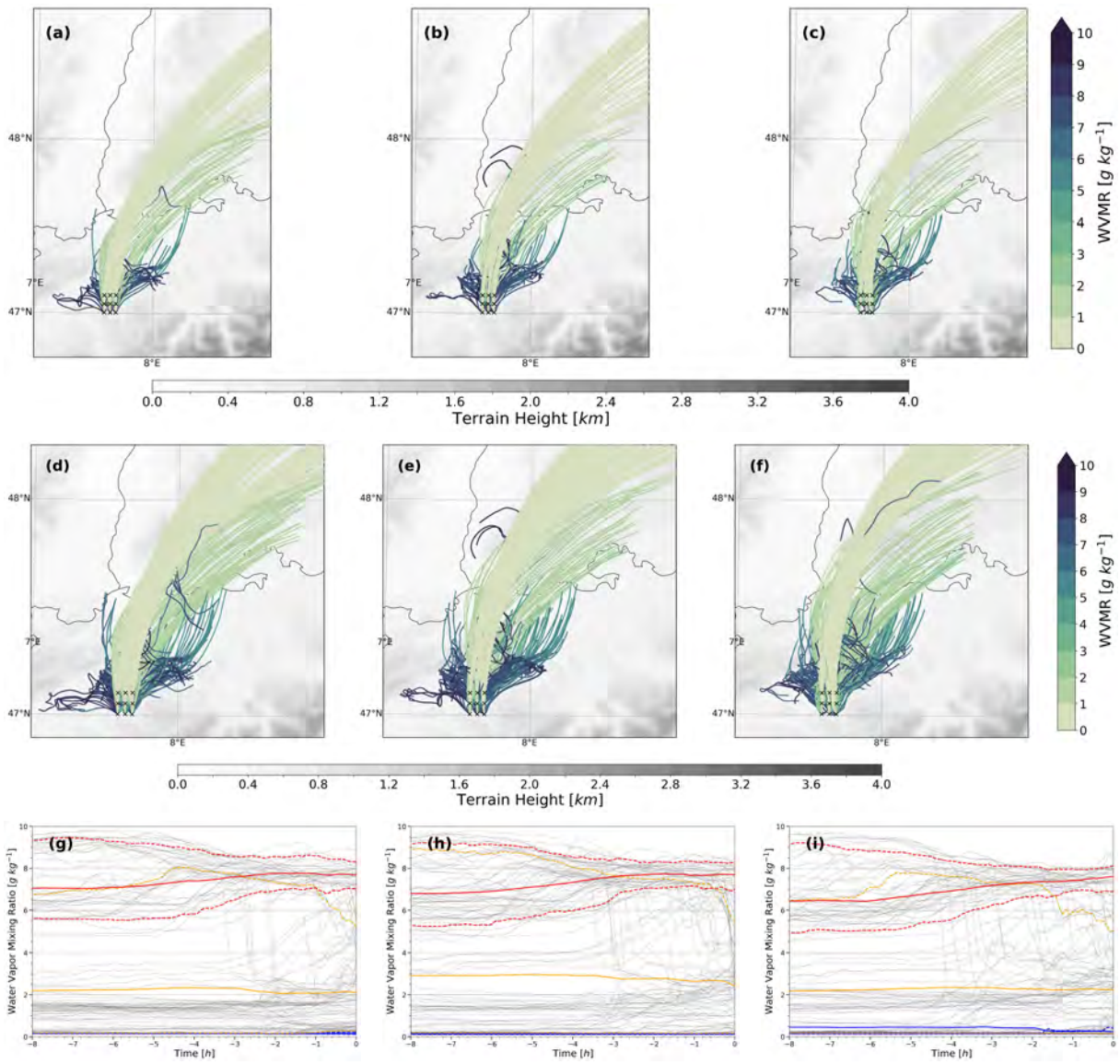

Figure 5.2.3: Same as Figure 5.2.1, but for water vapour mixing ratio (WVMR) [g kg^{-1}].

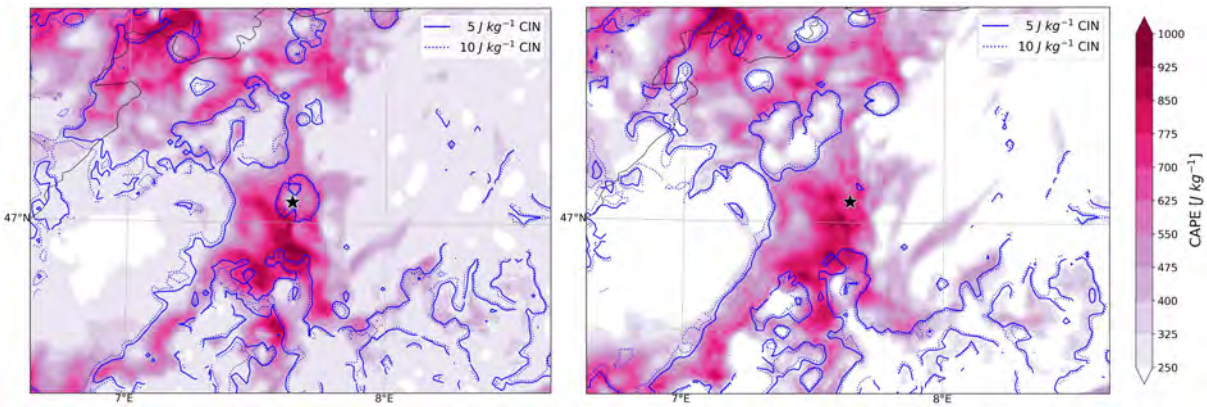

Figure 5.2.4: Horizontal map of Convective Available Potential Energy (CAPE) [J kg^{-1}] and 5 and 10 J kg^{-1} contour lines (solid and dotted blue) of Convective Inhibition (CIN) [J kg^{-1}] on 09.05.2018 at initiation time 14:05 UTC (left) and 30 minutes before initiation 13:35 UTC (right) with initiation location (7.63891° E, 47.0546° N, asterisk) for northern Switzerland.

time. After the thunderstorm initiation (Figure 5.2.7f), the trajectories in the area of initiation have lower Theta-E values (318-320 K) compared to the time step before the initiation (322-323 K, Figure 5.2.7d). The before mentioned gradient is better visible in the temporal evolution plots (Figure 5.2.7g-i), when the means of the trajectories of the lowest starting height (SFC up to 2 km, red) are compared with the trajectories starting from highest (7 up to 10 km, blue) or middle (2 up to 7 km, orange) altitudes.

The tracing of maximum updraft (see Figure 5, Appendix) did not produced many remarkable patterns. Most of the updrafts signals popped up along the high starting trajectories. Updrafts were already in progress before the thunderstorm initiation (Figure 5a) in the area of initiation, which intensified during the initiation (Figure 5b). While after the initiation (Figure 5c), the further distant signals in higher altitudes were more pronounced. Based on the closer look at Figure 5d-f), the strongest updrafts signals in the area of initiation shift from north to south, while the time elapses from before to after the initiation. The temporal evolution panels (Figure 5g-i) confirm the impression gained in the beginning regarding augmented updraft in mid-troposphere (2 up to 7 km, orange) and higher (7 up to 10 km, blue). In addition, a strong updraft signal is striking (Figure 5i) in the highest trajectories (beginning 2 hours before start).

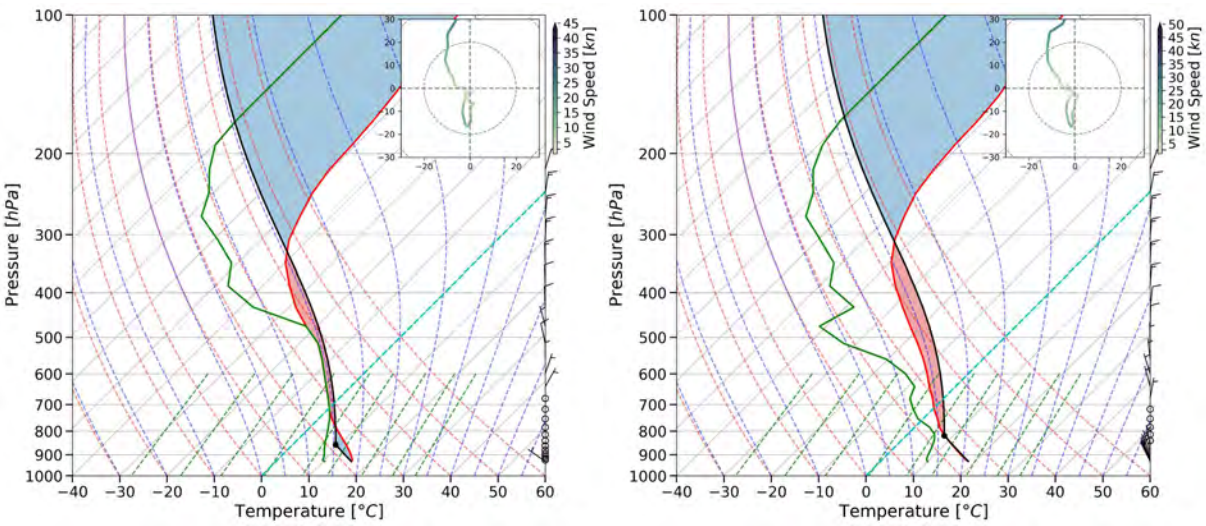

Figure 5.2.5: Skew T-log p diagram at location of initiation (7.63891° E, 47.0546° N) on 09.05.2018 at initiation time 14:05 UTC (left) and 30 minutes before initiation 13:35 UTC (right). See Figure 5.1.5 for description.

The horizontal wind on the 900 hPa level is shown in Figure 5.2.8 (left), which displays a northwesterly

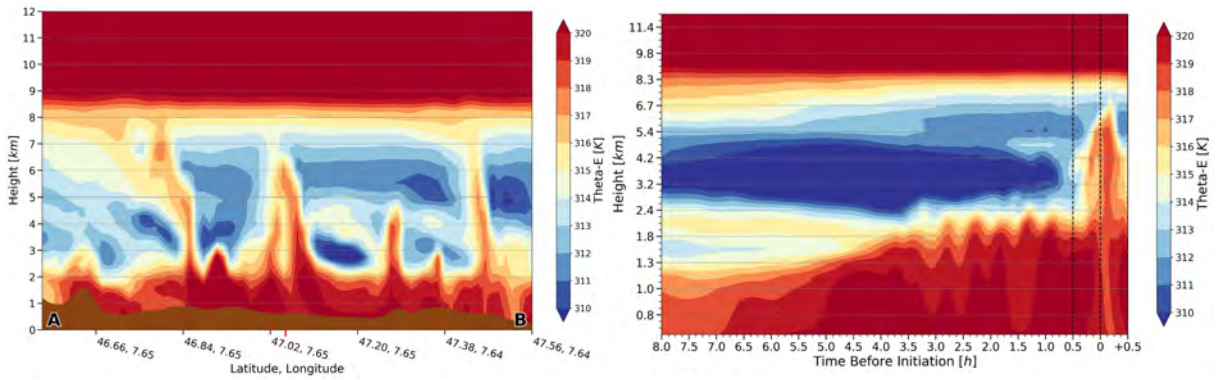

Figure 5.2.6: Left: Vertical cross-section (VCS) of equivalent potential temperature (Theta-E) [K] on 09.05.2018 at 14:05 UTC. VCS in north-south direction with initiation location indicated by red tick on x-axis, starts at A (7.63891° E, 46.5546° N) and ends at B (7.63891° E, 47.5546° N). Right: Temporal evolution of Theta-E [K] at the location of initiation (7.63891° E, 47.0546° N) and its surroundings until 8 hours before the thunderstorm initiation (see above). Vertical dashed lines indicate 30 minutes before, during and after the initiation time (starting times of trajectories).

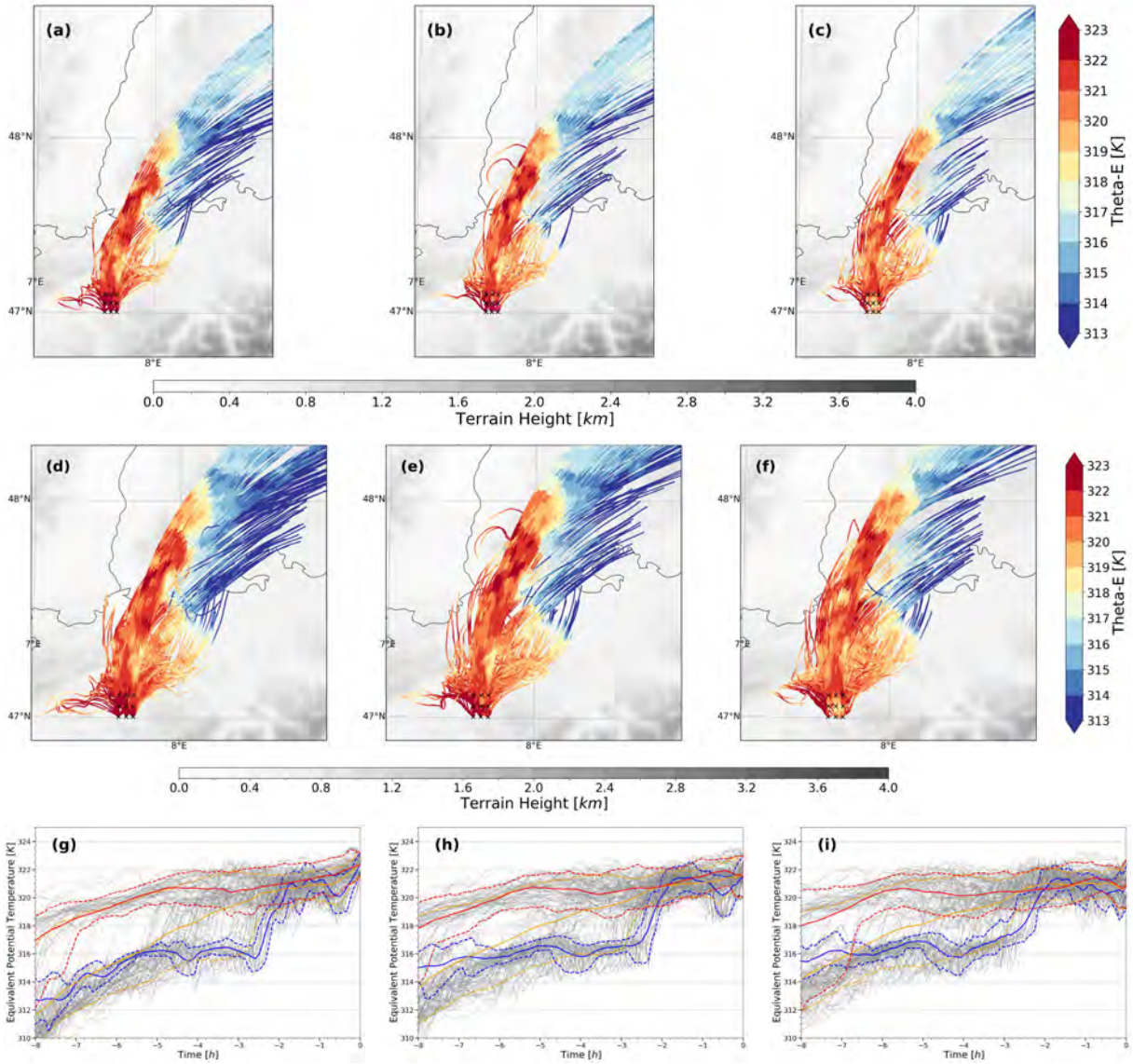

Figure 5.2.7: Same as Figure 5.2.1, but for equivalent potential temperature (Theta-E) [K].

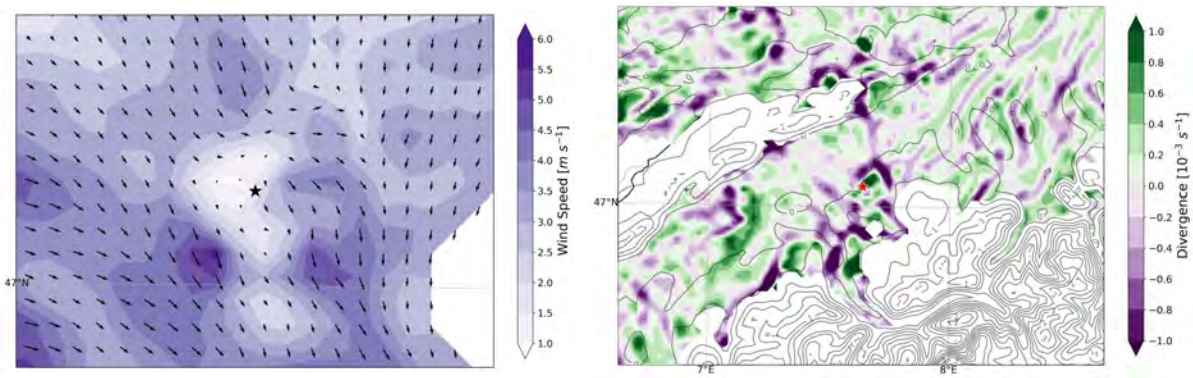

Figure 5.2.8: Left: Horizontal map of wind speed [m s^{-1}] and direction @ 900 hPa on 22.05.2018 at 17:00 UTC with initiation location (7.56971° E, 47.4961° N, asterisk) for northern Switzerland. Right: Horizontal map of wind divergence @ 900 hPa [10^{-3} s^{-1}] on time and location of initiation (see above). The contour lines indicate the terrain height [km] for the area of northern Switzerland.

wind northwest and a northerly wind northeast of the initiation location (asterisk). As already mentioned in the beginning of this case study, the initiation location lies south of the Napf region (Emmental Alps) in a hilly environment (see Figure 5.2.8, right). Figure 5.2.9 presents a VCS of vertical wind speed (hereafter Omega), which indicates strong downwinds (>15 Pa s^{-1}) close to the initiation location. Next to it, strong upwind signals (<-15 Pa s^{-1}) are allocated on each side of the downwind signal. Furthermore, strong negative divergence (<-1 10^{-3} s^{-1}) areas are located close to the initiation location in the north (see Figure 5.2.9, right).

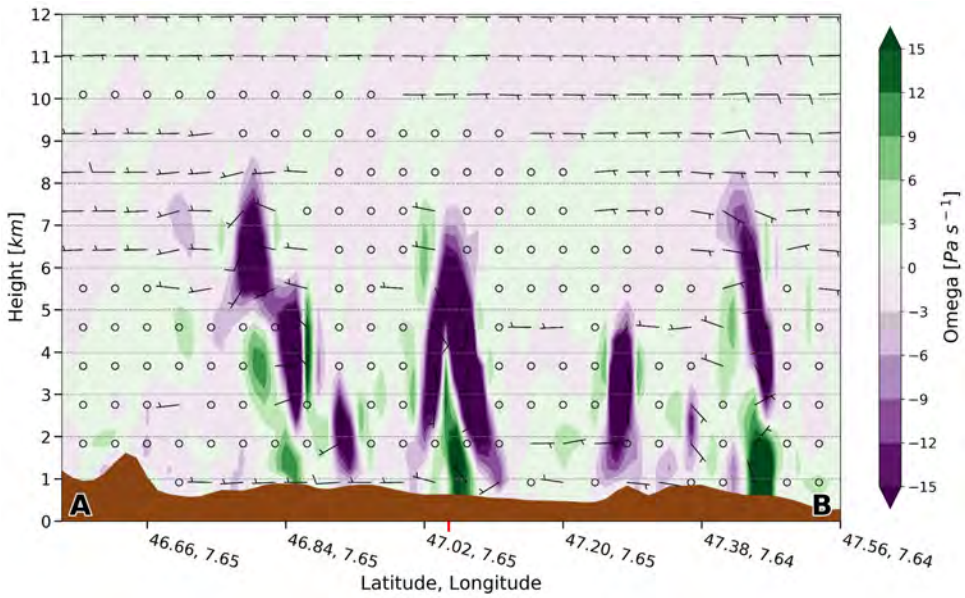

Figure 5.2.9: Left: Vertical cross-section (VCS) of vertical motion (Omega) [Pas^{-1}] on 09.05.2018 at 14:05 UTC. VCS in north-south direction with initiation location indicated by red tick on x-axis, starts at A (7.63891° E, 46.5546° N) and ends at B (7.63891° E, 47.5546° N).

Summarising the results of this case study, I initially emphasised the approach to the initiation location of all the air parcels from the north. By presenting the WVMR along trajectories, I could show that this separation coincides with the moisture content of the air parcels. This is mainly related to the decreasing air temperature with height, whereby the water vapour capacity of the air parcels decreases correspondingly. The VCS of RH showed high values of RH (90-100 %) from the surface up to the mid-troposphere. This finding was complemented by the detection of saturated layers in the skew T-log p

diagram. There, I could further identify a conditional unstable layer (LCL up to 400 hPa). The analysis of the temporal evolution of CAPE and CIN revealed a decrease of CAPE (700-775 to 325-400 J kg^{-1}) and built up of CIN (<5 to >10 J kg^{-1}) until the thunderstorm initiation. On the temporal evolution of Theta-E, a strong vertical gradient of higher (318-320 K, SFC up to 1.3 km) and lower (310-313 K, 2.4 up to 5.4 km) Theta-E was present until half an hour before the initiation. Close to the initiation area in the vicinity of the Emmental Alps, a northwesterly and northeasterly wind was blowing at 900 hPa. Finally, besides a strong downwind (>15 Pa s^{-1}) encompassed by strong upwind signals (<-15 Pa s^{-1}), the divergence was strongly negative (<-1 10^{-3} s^{-1}) close to the initiation location. A strong (directional) wind shear could not be detected, which implies a minor role for the initiation of the thunderstorm in this case study.

These results lay the basis for the assessment of the basic ingredients for thunderstorm initiation. By means of the VCS and temporal evolution of RH, many layers of the atmosphere can be designated as saturated (high RH, 90-100 %). This could also be derived from the skew T-log p diagram, where a saturation was shown of the atmospheric layer between 750 and 450 hPa. Although, the temporal evolution figure displayed a small loss of moisture in the boundary layers (to 50-80 %). The trajectories show ground level moving air parcels with a high moisture content (7-10 g kg^{-1}). All findings combined, I can infer that a substantial amount of boundary-level moisture was present and this basic ingredient was available.

The CAPE values were higher in the pre-storm environment (700-775 J kg^{-1}) and then decreased starting 15 minutes before the thunderstorm initiation (325-400 J kg^{-1}). The reason for that could lie in already started convection (layer between 700 and 600 hPa is saturated, upwind signals already detectable). Although, CIN only built up before the initiation (>10 J kg^{-1}), CAPE was not reduced by previous convection and could build up. In the skew T-log p diagram, a conditional unstable layer can be found (LCL up to 400 hPa). In addition, the strong vertical Theta-E gradient of lower (318-320 K) layered above higher Theta-E (310-313 K), results in an inversion of the vertical Theta-E gradient. This inversion was half an hour before the initiation strong pronounced and infer the presence of potential instability in the atmosphere. The steadily increase of Theta-E along the trajectories could be explained by an increase of the temperature since the morning and/or an increase in the moisture in the atmosphere propagating further southwards. All findings combined indicate an conditional instability present in the atmosphere and hence, the fulfilment of this basic ingredient for thunderstorm initiation.

For the finding of the triggering mechanism, I refer to the already mentioned location of the thunderstorm initiation north of the Emmental Alps. Towards this hilly landscape, a northwesterly and northeasterly wind was blowing, which suggest an orographic-related triggering mechanisms. Moreover, these winds converge in the area of initiation. On the VCS of Omega could be detected, that strong upwinds (<-15 Pa s^{-1}) are located above the initiation location. They could emerge from the up- and downdrafts of the initiating thunderstorm. In addition, the wind barbs indicate southerly winds close to the surface, which enhances the convergence with the northerly winds. This convergence is confirmed by a strong negative divergence value (<-1 10^{-3} s^{-1}) north of the area of initiation. In the end, I would determine the triggering mechanism as a combination of orographic-related forcing and low-level convergence.

5.3 Case Study III

In this case study I analyse a thunderstorm initiated on 12.05.2018 at 20:15 UTC in northeastern Switzerland (8.64449°E, 47.5522°N; see Figure 4.1.1 for case study location). The thunderstorm has a maximum reflectivity value of 57.6 dBZ, which is the third highest value of all case studies. Figure 4 (Appendix) contains spatial information regarding the thunderstorm initiation location, the vertical cross-section path and the extent of the figures in the subsequent case study analysis. The trajectories of air parcels traced 8 hours backwards in time are shown in Figure 5.3.1 with their indicated levels of altitude. On the figures in the first row (Figure 5.3.1a-c), three different directions of approach are distinguishable to the initiation location (cross in the middle): northeast, south and southwest. The directional change of approach corresponds to the increasing starting height. The lowest traced air parcels are approaching the initiation location from northeast, while the highest arrive from the opposite direction. By looking at the trajectories from the surface up to 6.5 km in more detail (Figure 5.3.1d-f), two sharp directional changes are detectable along the lower trajectories on altitudes up to 2.6 km (especially during initiation, Figure 5.3.1e). Furthermore, the temporal evolution panels (Figure 5.3.1g-i) show a strong ascent (from

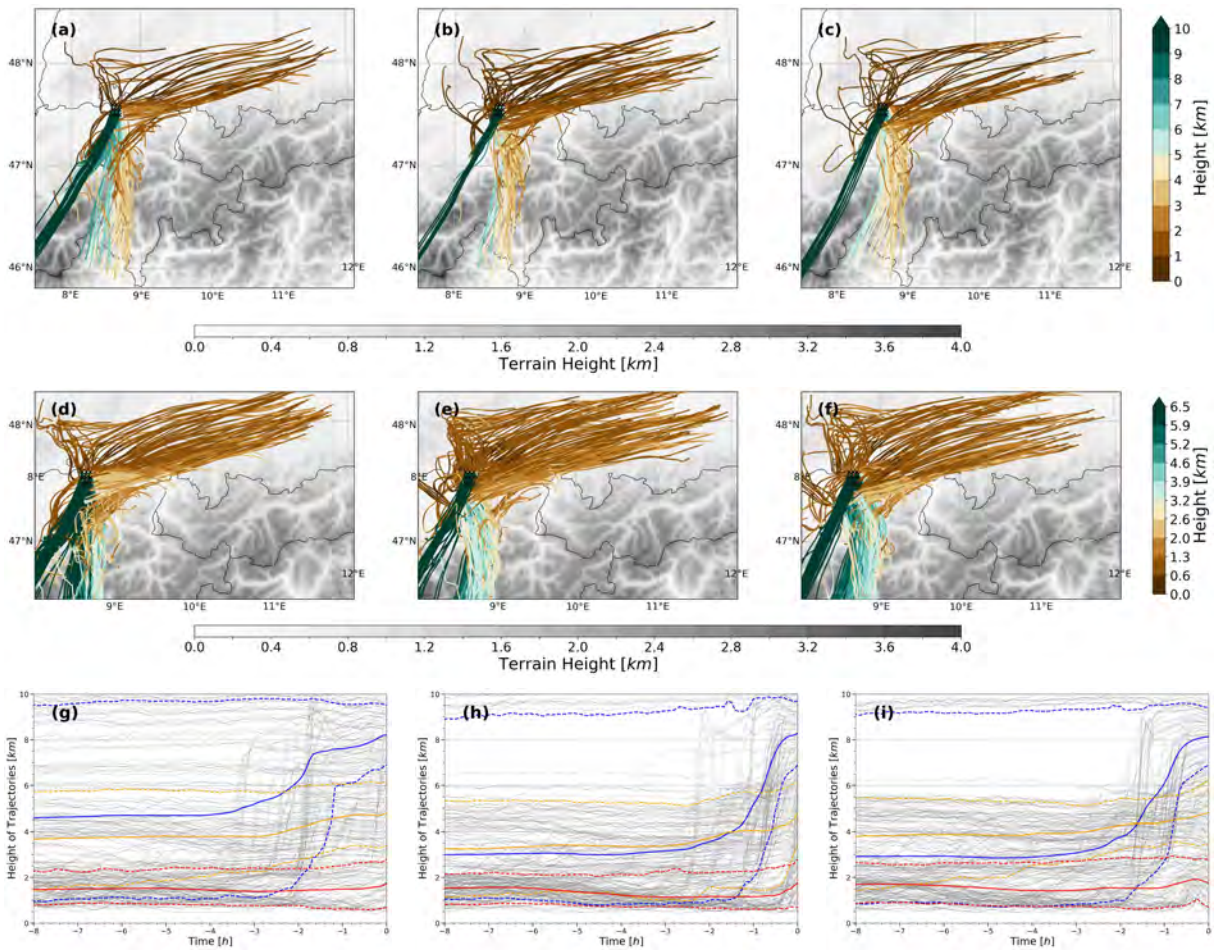

Figure 5.3.1: Height [km] along 8 hours backwards calculated trajectories started 30 minutes before (left), during (middle) and 30 minutes after (right column) thunderstorm initiation (12.05.2018 - 20:15 UTC). The starting points of the trajectories consist of the initiation location (8.64449° E, 47.5522° N) and 8 starting points 0.05° in each direction (crosses). The background of the panels in the upper two rows represents the terrain height [km] for the area of northeastern Switzerland. (a)-(c): Horizontal maps of trajectories with starting heights every 100 m from surface (SFC) up to 10 km (every 5th trajectories is plotted). (d)-(f): Horizontal maps of trajectories with starting heights every 100 m from surface up to 6 km (every 2nd trajectories is plotted). The figures show a smaller spatial extent, compared to the figures of the first row. (g)-(i): Temporal evolution along trajectories separated in three categories corresponding to their starting height: SFC up to 3 km (red), 3 up to 6.5 km (orange) and 6.5 up to 10 km (blue) with solid (dashed) lines for mean (10th and 90th percentile).

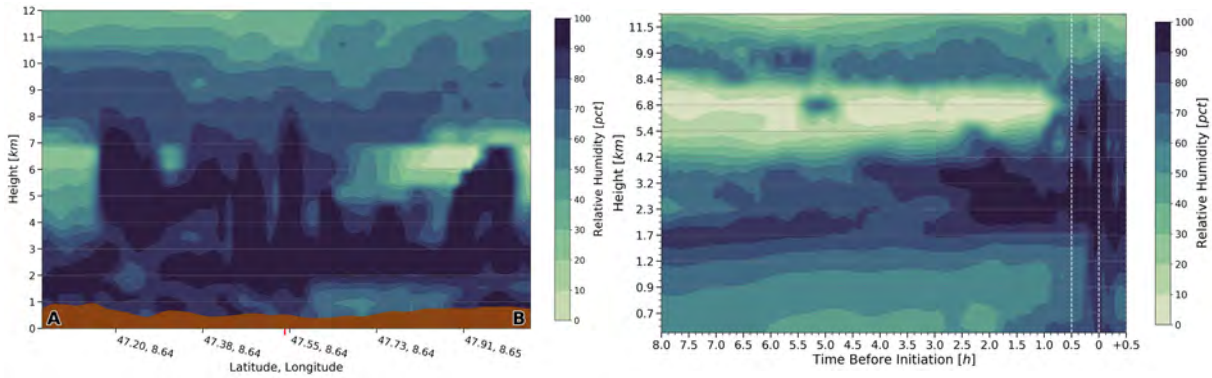

Figure 5.3.2: Left: Vertical cross-section (VCS) of relative humidity (RH) [%] on 12.05.2018 at 20:15 UTC. VCS in north-south direction with initiation location indicated by red tick on x-axis, starts at A (8.64449° E, 47.0522° N) and ends at B (8.64449° E, 48.0522° N). Right: Temporal evolution of RH [%] at the location of initiation (8.64449° E, 47.5522° N) and its surroundings until 8 hours before the thunderstorm initiation (see above). Vertical dashed lines indicate 30 minutes before, during and after the initiation time (starting times of trajectories).

3 to 8.25 km during the initiation Figure 5.3.1h) of trajectories with starting height from 6.5 up to 10 km (blue).

The RH in the PBL is some percentages lower (80-90 %) compared to the maximum RH values (90-100 %) found in the layers from 1.5 to 8 km above the thunderstorm initiation location (red tick on x-axis in see Figure 5.3.2, left). Starting from 2 hours before the initiation, RH values increased in the PBL

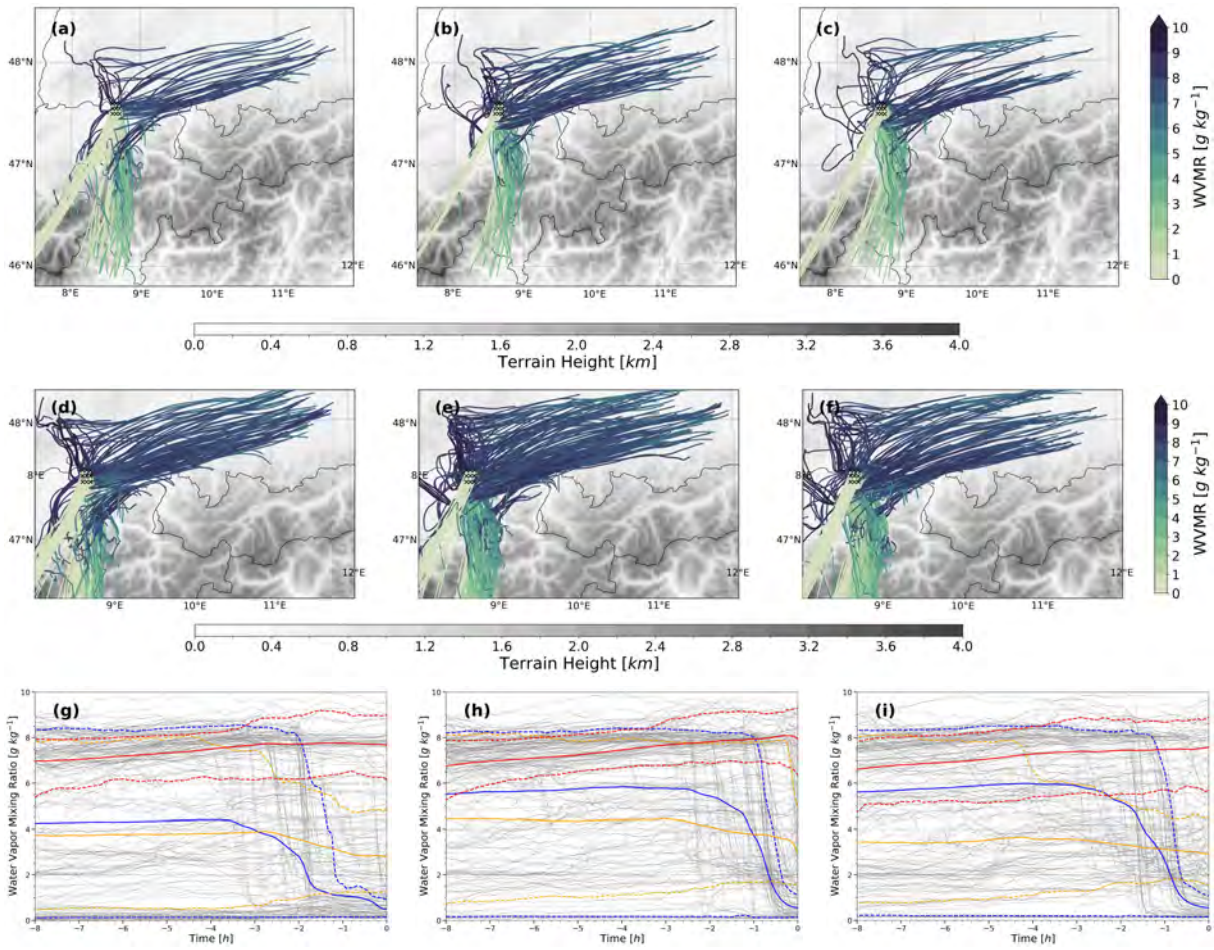

Figure 5.3.3: Same as Figure 5.3.1, but for water vapour mixing ratio (WVMR) [g kg^{-1}].

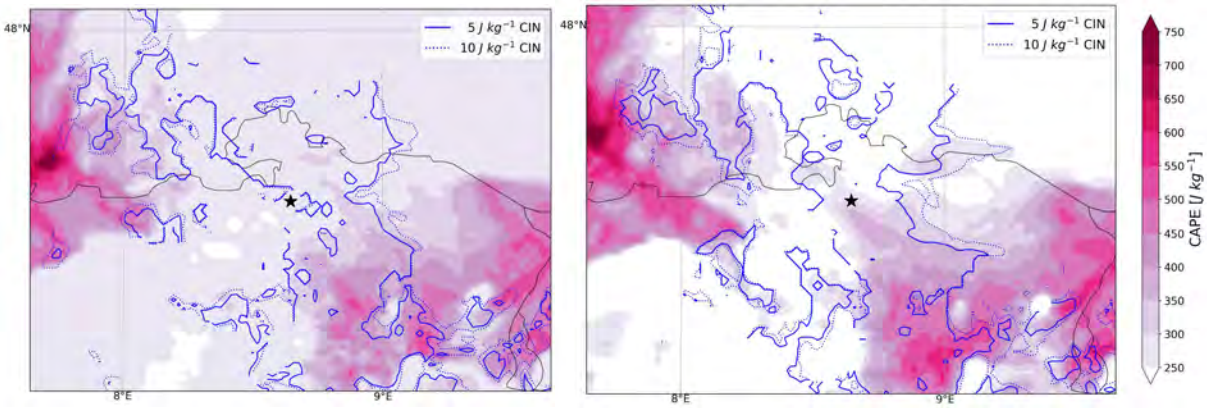

Figure 5.3.4: Horizontal map of Convective Available Potential Energy (CAPE) [J kg^{-1}] and 5 and 10 J kg^{-1} contour lines (solid and dotted blue) of Convective Inhibition (CIN) [J kg^{-1}] on 12.05.2018 at initiation time 20:15 UTC (left) and 30 minutes before initiation 19:45 UTC (right) with initiation location (8.64449° E, 47.5522° N, asterisk) for northeastern Switzerland.

from 40-50 % to 80-90% (see Figure 5.3.2, right). The corresponding trajectories, which are coloured according to their WVMR are presented in Figure 5.3.3a-f). The air parcels approaching from northeast have a higher water vapour content (6-10 g kg^{-1}), than air parcels approaching from the south (0-5 g kg^{-1}) and southwest (0-1 g kg^{-1}). Figure 5.3.3g) reveals that trajectories starting above 3 km (3 up to 6.5 km, orange and 6.5 up to 10 km, blue) already start losing moisture 4 hours before initiation (orange: 3.75 to 2.75 g kg^{-1} and blue: 4.25 to 0.5 g kg^{-1}). At the same time, the moisture content increases along the 8 hours trajectories below this altitude threshold (SFC up to 3 km, red) from 7 to 7.75 g kg^{-1}. During the initiation (Figure 5.3.3h), this increase is more pronounced (6.75 to 8 g kg^{-1}) until shortly before the initiation, when in all atmospheric layers the WVMR decreases.

At the time and location of initiation (asterisk in Figure 5.3.4, left), there was almost no CAPE (<250 J kg^{-1}) and CIN with non-zero values present (>10 J kg^{-1}). Half an hour before the thunderstorm initiation (see Figure 5.3.4, right), CAPE was between 300 and 350 J kg^{-1} and CIN already greater than 10 J kg^{-1}. This decrease of CAPE is also detectable in the skew T-log p diagram (see Figure 5.3.5). The comparison of the areas of CIN (blue) infers a decrease of CIN until the initiation of the thunderstorm. Further, the skew T-log p diagram indicates an increase of the simulated absolute temperature (red line)

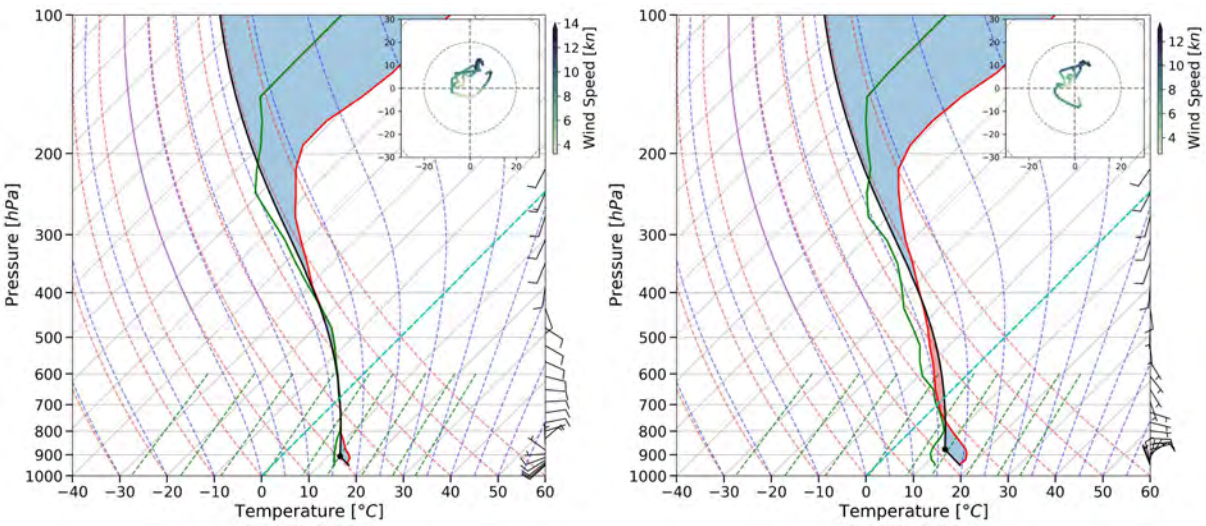

Figure 5.3.5: Skew T-log p diagram at location of initiation (8.64449° E, 47.5522° N) on 12.05.2018 at initiation time 20:15 UTC (left) and 30 minutes before initiation 19:45 UTC (right). See Figure 5.1.5 for description.

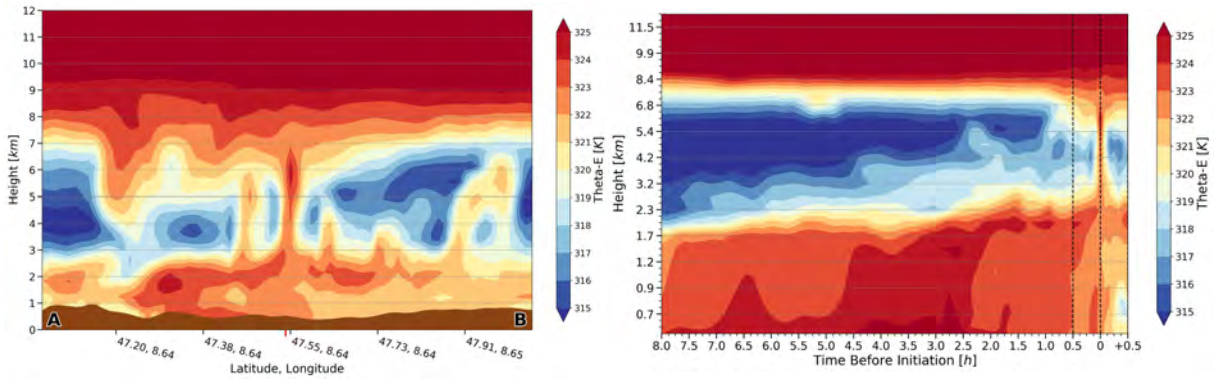

Figure 5.3.6: Left: Vertical cross-section (VCS) of equivalent potential temperature (Theta-E) [K] on 12.05.2018 at 20:15 UTC. VCS in north-south direction with initiation location indicated by red tick on x-axis, starts at A (8.64449° E, 47.0522° N) and ends at B (8.64449° E, 48.0522° N). Right: Temporal evolution of Theta-E [K] at the location of initiation (8.64449° E, 47.5522° N) and its surroundings until 8 hours before the thunderstorm initiation (see above). Vertical dashed lines indicate 30 minutes before, during and after the initiation time (starting times of trajectories).

close to the surface. This increase is much more pronounced 30 minutes before the initiation (see Figure 5.3.5, right). Above this temperature inversion, a conditional unstable layer is existing up to 700 hPa. This unstable layer is shrunk at the time of initiation and the atmosphere is saturated up to 400 hPa (see Figure 5.3.5, left). Further, the wind barbs along the right y-axis indicate a change in wind direction on the 800 and 500 hPa height levels.

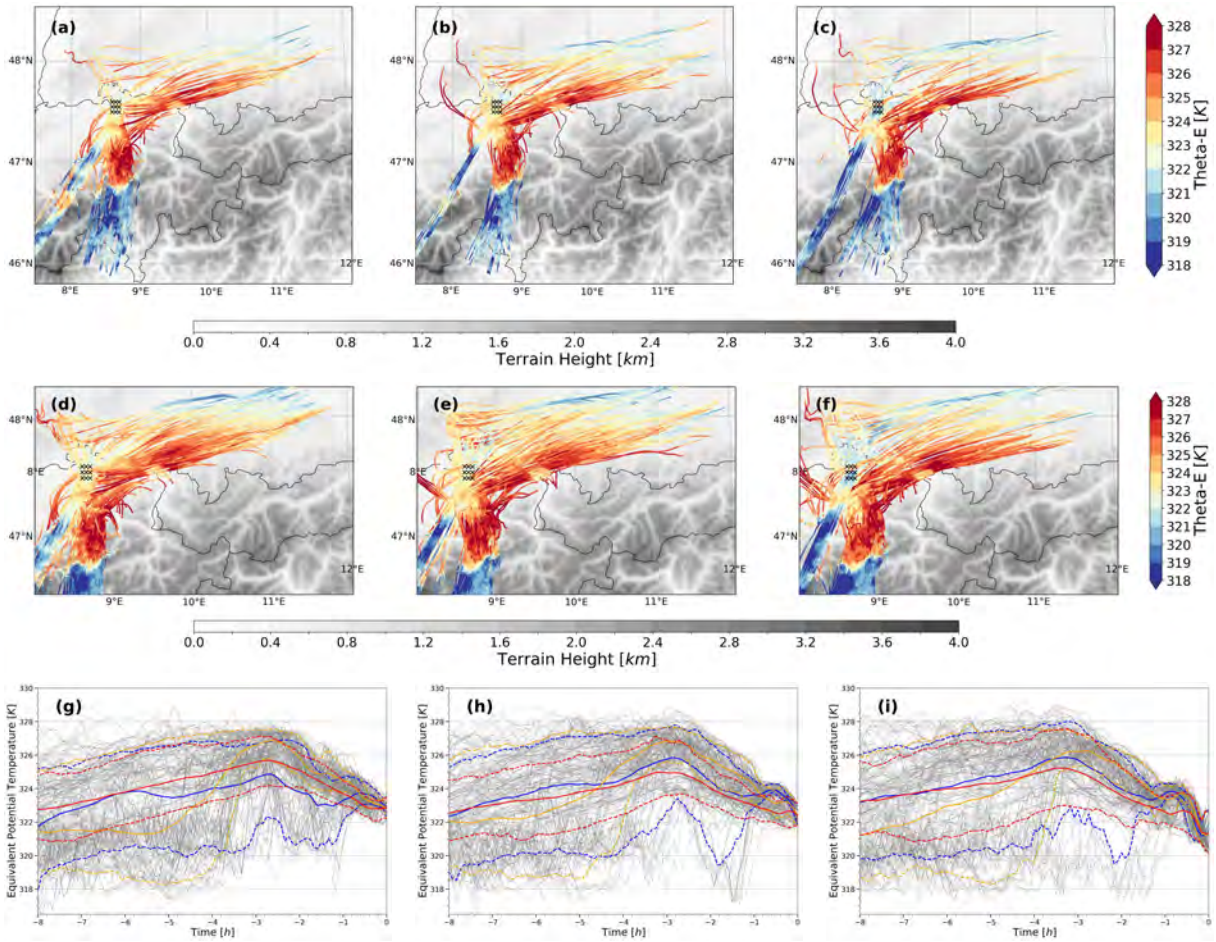

Figure 5.3.7: Same as Figure 5.3.1, but for equivalent potential temperature (Theta-E) [K].

The vertical Theta-E gradient (layering of lower above higher Theta-E) is not as pronounced during the thunderstorm initiation of this case study (see Figure 5.3.6, left above red tick). In the temporal evolution figure (see Figure 5.3.6, right) a stronger gradient can be detected 4.5 to 2.5 hours before the initiation (323-325 K from SFC up to 1.7 km and 315-319 K from 3.2 up to 6.8 km) and its subsequent declination until the thunderstorm initiation. The mean of the three height categories (see Figure 5.3.7g-i) indicate an ascent in Theta-E until approximately 2.5 hours before thunderstorm initiation. The following decrease of the mean values, is steady before the initiation (Figure 5.3.7g) and abrupt intensified during as well as after the initiation (Figure 5.3.7h-i). The mean of the lowest trajectories (SFC up to 3 km) is in the last 4 hours always the lowest during the initiation (Figure 5.3.7h). Trajectories from the starting heights between 3 and 6.5 km (orange) have in each case the highest Theta-E mean value (326-327 K). Subsequently, all of the means drop to an even level at the time of initiation, which level is higher before (323 K) than during (322.5 K) and after the initiation (321.25 K).

Figure 5.3.8 presents the maximum updraft values along the calculated trajectories. Before the initiation (Figure 5.3.8a), updraft occurs along many trajectories. But eye-catching are the widespread updraft signals along the upper level trajectories, which origin in the southwest. Around the initiation location, the updraft signals are the most pronounced (>5 m s^{-1}) during the initiation (Figure 5.3.8b). Compared to the situation 30 minutes before the thunderstorm initiation, more updraft signals are detectable after the initiation north and east of the initiation area (Figure 5.3.8c). By taking a closer look at the trajectories with a starting height up to 6.5 km before the initiation (Figure 5.3.8d), I can identify updraft signals in vicinity of the southwest starting location. During thunderstorm initiation (Figure 5.3.8e),

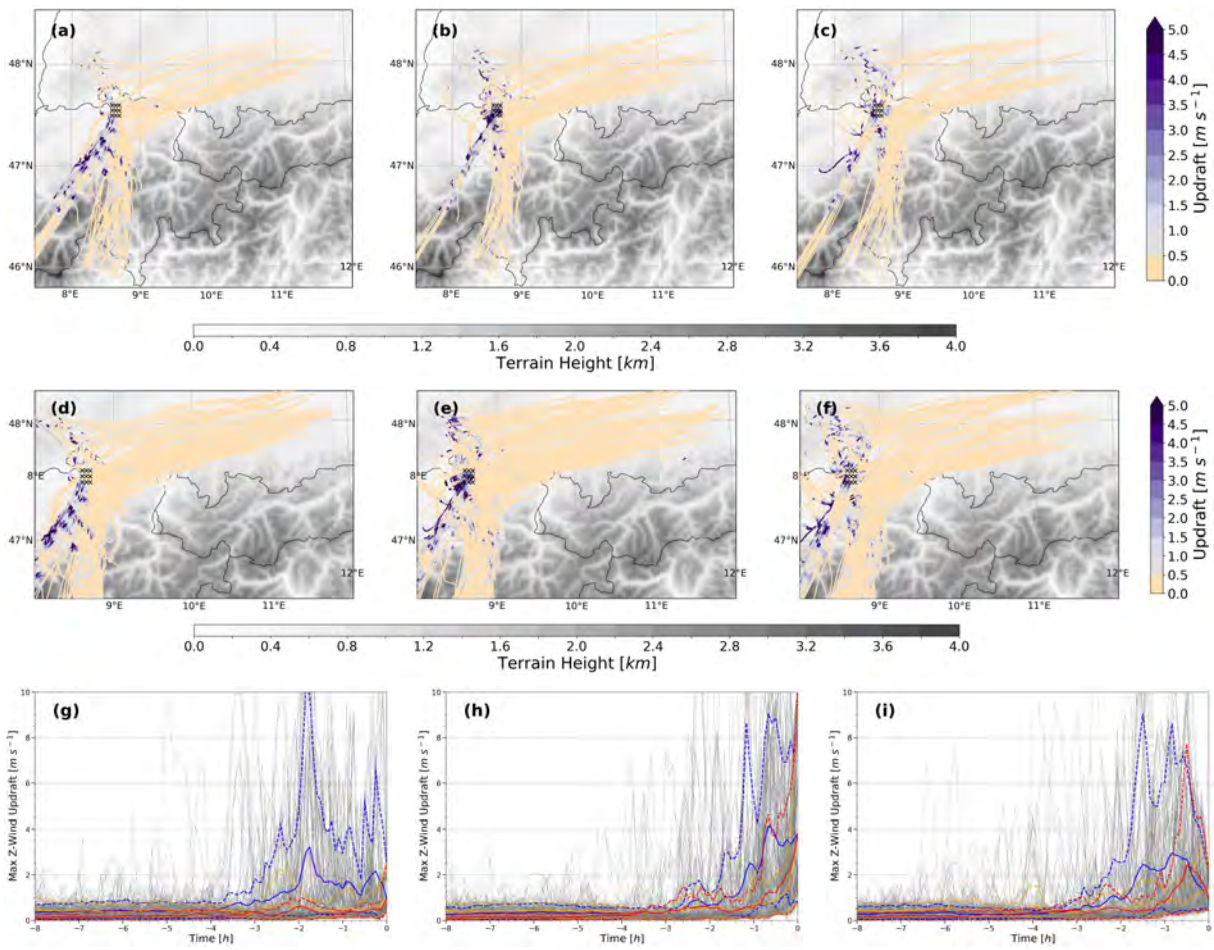

Figure 5.3.8: Same as Figure 5.3.1, but for maximum z-wind updraft [m s^{-1}].

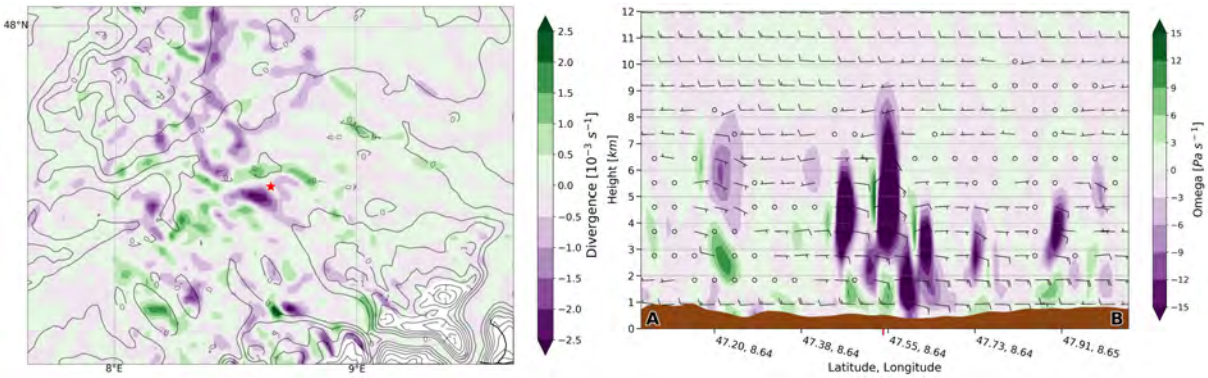

Figure 5.3.9: Left: Horizontal map of wind divergence @ 850 hPa [10^{-3} s^{-1}] on 12.05.2018 at 20:15 UTC with initiation location (8.64449° E, 47.5522° N, asterisk). The contour lines indicate the terrain height [km] for the area of northeastern Switzerland. Right: Vertical cross-section (VCS) of vertical motion (Omega) [Pa s^{-1}] on initiation time (see above). VCS in north-south direction with initiation location indicated by red tick on x-axis, starts at A (8.64449° E, 47.0522° N) and ends at B (8.64449° E, 48.0522° N).

these southwest updrafts intensified from the west. Air parcels with high updraft values (>5 m s^{-1}) approaching the location (cross in the middle) from southeast. The mentioned above updraft signals in higher altitude (6.5 up to 10 km, blue) before the initiation, are clearly visible on the temporal evolution panel (Figure 5.3.8g) with a rapid increasing mean 2 hours (1.5 to 3.25 m s^{-1}) before the reaching the initiation area. The strongest increase in the mean updraft during the initiation (Figure 5.3.8h), can be found in the mid-troposphere (3 up to 6.5 km, orange) in the last 1.5 hours before the thunderstorm initiation (0.5 to 3.75 m s^{-1}).

The initiation area lies in an area of negative divergence and northeast of strong negative divergence values (<-2.5 10^{-3} s^{-1}) see Figure 5.3.9, left). Above, as well as south and north of the initiation location (red tick in x-axis), areas of strong upwinds (<-15 Pa s^{-1}) are detectable on the VCS of Omega (see Figure 5.3.9, right). Beneath this strong upwind is also a downwind signal (0-12 Pa s^{-1}) detectable over the initiation location. In addition, southwest of the initiation location lies an area with strong updraft (>11 m s^{-1}) and high reflectivity values (>45 dBZ, see Figure 5.3.10, left). Moreover, on Figure 5.3.10 (right) lower Theta-E values (316-319 K) are found southwest of the initiation location.

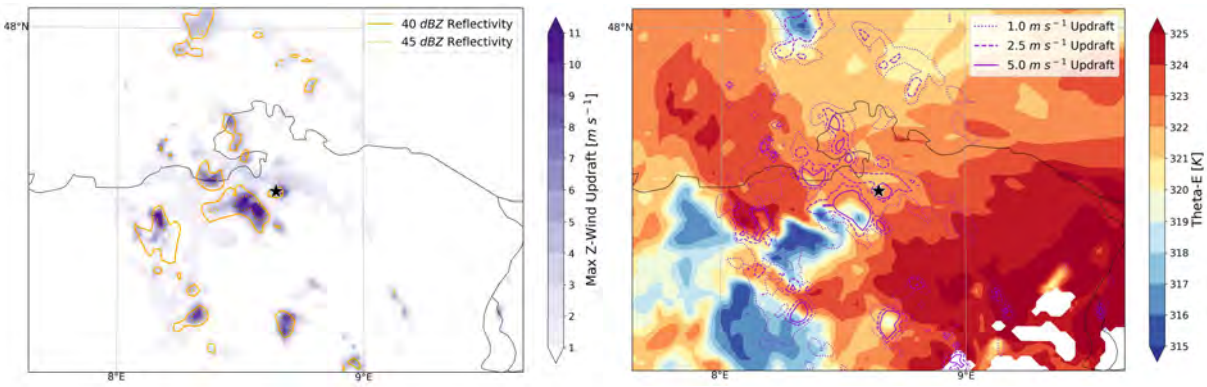

Figure 5.3.10: Left: Horizontal map of maximum z-wind updraft [m s^{-1}] and 40 and 45 dBZ contour lines (solid and dotted orange) of maximum derived radar reflectivity [dBZ] on 12.05.2018 at 20:15 UTC with initiation location (8.64449° E, 47.5522° N, asterisk) for northeastern Switzerland. Right: Horizontal map of equivalent potential temperature (Theta-E) @ 850 hPa [K] on time and location of initiation (see above) for northeastern Switzerland.

Consequently, the results of this case study showed that a reversal of the approach direction was ascertainable between the lowest and the highest trajectories. Next, I could detect a high amount of moisture present in the atmosphere (90-100 %, 1.5 up to 8 km) and as well along the lower trajectories

(6-10 g kg^{-1}, SFC up to 3 km). CAPE and CIN were higher before (300-350 and >10 J kg^{-1}) and decreased until the initiation of the thunderstorm (<250 and >10 J kg^{-1}). A temperature inversion in the PBL, a conditional unstable layer above (up to 700 hPa) and a change in wind direction was identifiable in certain altitudes (800 and 500 hPa). During the initiation, the strongest updrafts (>5 m s^{-1}) occurred in the western part of the initiation area along the trajectories from the west. The trajectories with high updraft values at the initiation location originated from southeast. At the time and location of initiation, signals of strong upwinds (<-15 Pa s^{-1}) and downwinds (0-12 Pa s^{-1}) could be detected. Finally, I showed the presence of negative divergence (<-2.5 10^{-3} s^{-1}), strong updraft (>11 m s^{-1}), high reflectivity (>45 dBZ) and low Theta-E values (316-319 K) southwest of the location of thunderstorm initiation.

Based on these results, RH was high (90-100 %) at the time and location of initiation, which corresponds to a saturated atmosphere. This was confirmed by the skew T-log p diagram. Although, this saturation dominated the atmospheric layers only shortly before the initiation. The moisture originated from the northeast and was transported along the lowest trajectories (SFC up to 3 km, 6-10 g kg^{-1}) to the initiation area. Hence, a boundary-layer moisture inflow was existing. Regarding the basic ingredient, these points lead me to the conclusion that a substantial amount of boundary-layer moisture was present at the time and location of initiation.

The skew T-log p diagram showed a small residue of a temperature inversion. Although this presence of an inversion (hence CIN, >10 J kg^{-1}), which was more pronounced half an hour before the initiation, CAPE could not built up (maximum values of 300-350 J kg^{-1} half an hour before the initiation) and was lower than 250 J kg^{-1} at the time of initiation. But due to this inversion, an conditional unstable layer (up to 700 hPa) could develop aloft (more pronounced with a stronger inversion 30 minutes before initiation). The Theta-E stratification supports this statement with an inversion of the vertical Theta-E gradient and a resulting potential instability in the atmosphere. Similar as for the strength of the inversion, the Theta-E gradient inversion was also more pronounced during the hours before the initiation. At the time of initiation, the thunderstorm cell already influenced the Theta-E stratification and decomposed the inversion. These findings allow to infer a certain degree of conditional instability present in the atmosphere.

Based on the height levels along the trajectories and the wind barbs of the skew T-log p diagram, I can infer a strong directional vertical wind shear in the atmosphere from the surface up to 10 km altitude. This indicates the existence of conditions for potentially strong deep convection.

In consideration of the instability assessed before, there is a need for a strong triggering mechanism. Although, convergence values are existing at the initiation location, they are much stronger in the aforementioned area southwest (<-2.5 10^{-3} s^{-1}). According to the high reflectivity (>45 dBZ) and updraft values (>11 m s^{-1}) in this area, thunderstorm cells are present and influence with their outflow boundaries the initiation of other thunderstorms. The outflow of these cells forms a cold pool, which is detectable by the lower Theta-E values in this area (316-319 K). The updraft increases at the gust front of this cold pool (>11 m s^{-1}), which spreads towards the initiation location of the thunderstorm discussed in this case study. This spreading is indicated by the wind barbs along the surface levels. These southwesterly winds strongly converge (<-2.5 10^{-3} s^{-1}) then with the northerly winds and lead to the initiation of convection and hence the thunderstorm. The strong directional wind shear present in the atmosphere, builds favourable conditions for long-lasting thunderstorms. To conclude, the propagating cold pool with its gust front and the associated convergence could have initiated the thunderstorm and is the most plausible triggering mechanism of this case study.

5.4 Case Study IV

A thunderstorm initiated on 10.05.2018 at 01:00 UTC over northeastern Switzerland (8.67235°E, 47.629°N, see Figure 4.1.1 for case study location) builds the basis for the fourth case study (see Figure 6, Appendix for more spatial information). It was the forth strongest thunderstorm tracked by TITAN with a maximum reflectivity value of 57.5 dBZ. In Figure 5.4.1 the calculated trajectories for this case studies are presented. With increasing starting height (SFC to 10 km, brown to greener colours), the trajectories approach the initiation location more from the north. The air parcels following the lower trajectories (SFC up to 2 km height levels) are approaching from the southwest. Comparing the evolution from before (Figure 5.4.1a) to after (Figure 5.4.1c) the thunderstorm initiation, then the trajectories from the upper and mid-levels (2 up to 10 km height levels) change their direction of approach to more westerly. With a closer look at the trajectories with starting heights from the surface up to 6 km (Figure 5.4.1d), there are unusual trajectories detectable in the lowest part of the atmosphere (SFC up to 1.2 km height levels). First, they move southwestwards and past the initiation location. Second, they make a sharp (180°) turn and approach finally from the southwest to the location of thunderstorm initiation. During the initiation

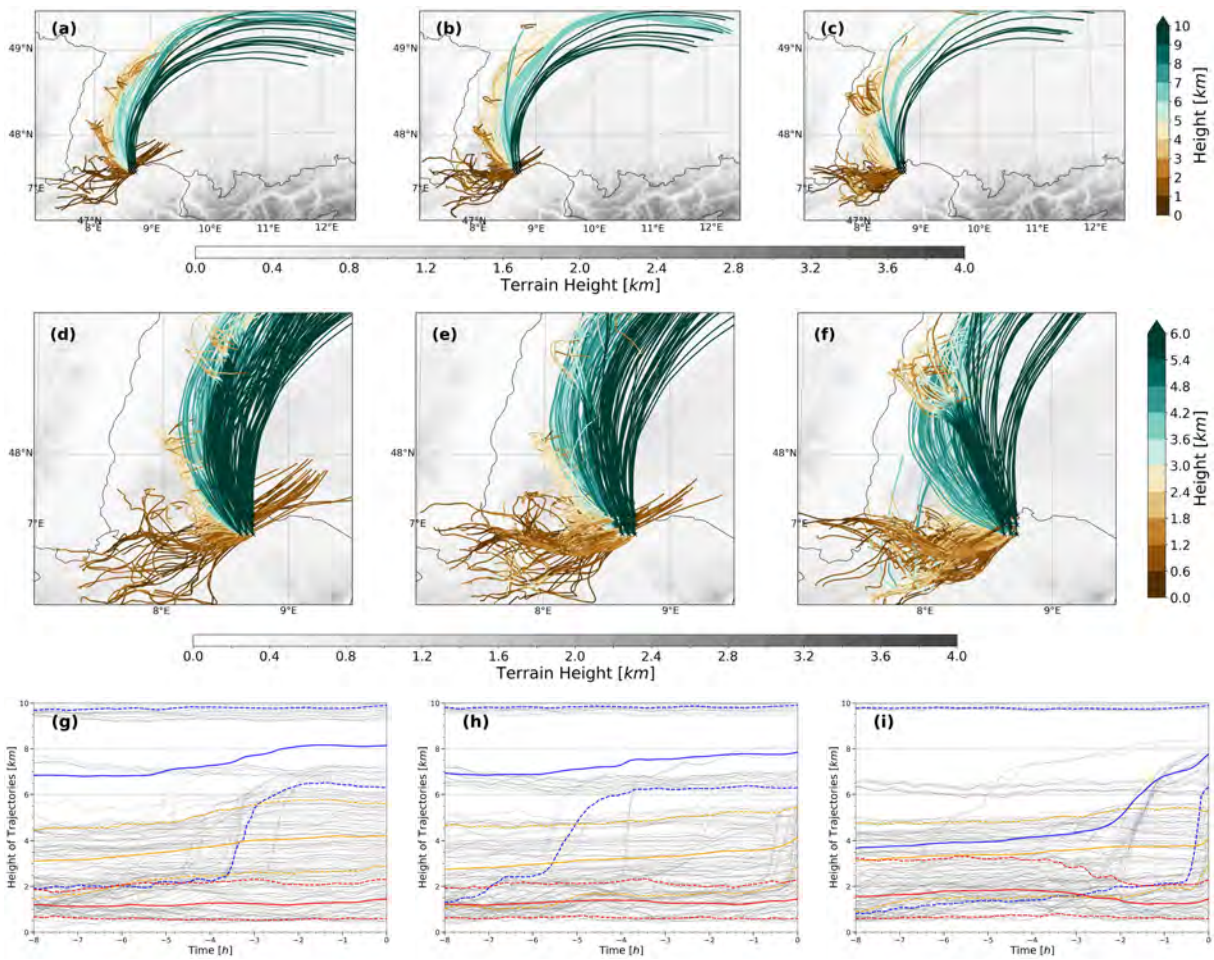

Figure 5.4.1: Height [km] along 8 hours backwards calculated trajectories started 30 minutes before (left), during (middle) and 30 minutes after (right column) thunderstorm initiation (10.05.2018 - 01:00 UTC). The starting points of the trajectories consist of the initiation location (8.67235° E, 47.629° N) and 8 starting points 0.05° in each direction (crosses). The background of the panels in the upper two rows represents the terrain height [km] for the area of northeastern Switzerland. (a)-(c): Horizontal maps of trajectories with starting heights every 100 m from surface (SFC) up to 10 km (every 5th trajectories is plotted). (d)-(f): Horizontal maps of trajectories with starting heights every 100 m from surface up to 6 km (every 2nd trajectories is plotted). The figures show a smaller spatial extent, compared to the figures of the first row. (g)-(i): Temporal evolution along trajectories separated in three categories corresponding to their starting height: SFC up to 2.5 km (red), 2.5 up to 6 km (orange) and 6 up to 10 km (blue) with solid (dashed) lines for mean (10th and 90th percentile).

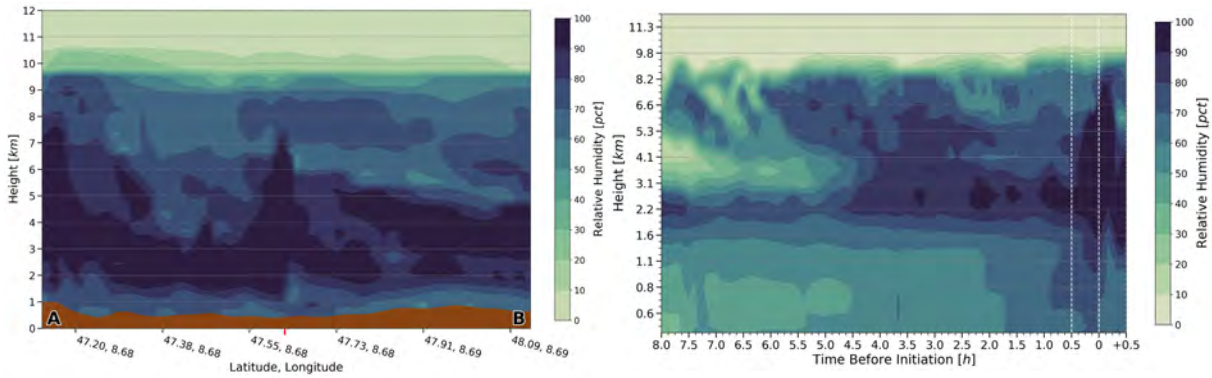

Figure 5.4.2: Left: Vertical cross-section (VCS) of relative humidity (RH) [%] on 10.05.2018 at 01:00 UTC. VCS in north-south direction with initiation location indicated by red tick on x-axis, starts at A (8.67235° E, 47.129° N) and ends at B (8.67235° E, 48.129° N). Right: Temporal evolution of RH [%] at the location of initiation (8.67235° E, 47.629° N) up to 8 hours before the thunderstorm initiation (see above). Vertical dashed lines indicate 30 minutes before, during and after the initiation time (starting times of trajectories).

(Figure 5.4.1e), these air parcels move further before they make a turnaround. After the initiation, this special pattern has disappeared (Figure 5.4.1f).

In the temporal evolution panel of the trajectories started 30 minutes before the initiation (Figure 5.4.1g), the mean of the high starting trajectories (6 up to 10 km, blue) ascends from 7 to 8 km altitude in a time period from 5.5 to 2 hours before thunderstorm initiation. This ascent is less pronounced (7

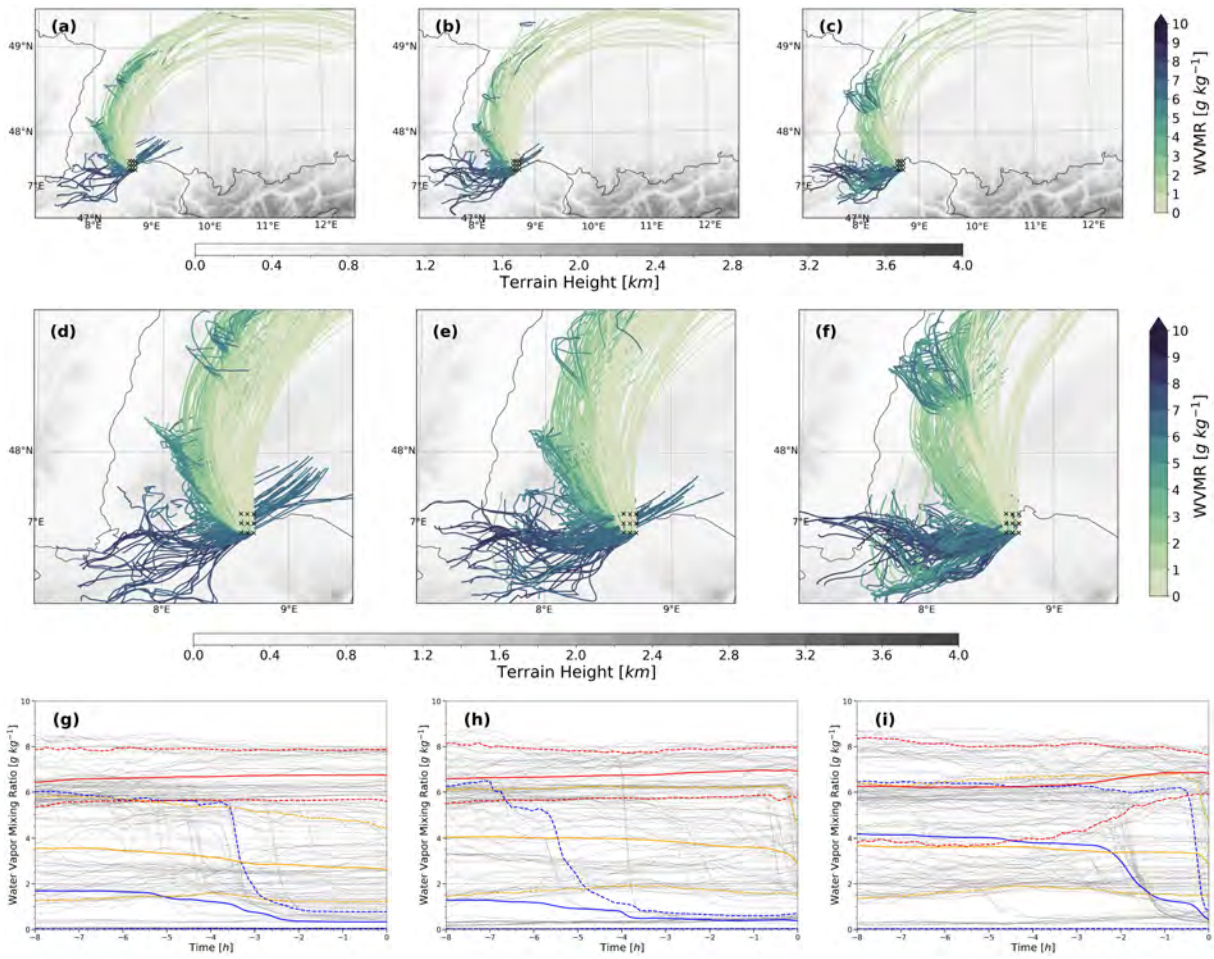

Figure 5.4.3: Same as Figure 5.4.1, but for water vapour mixing ratio (WVMR) [g kg^{-1}].

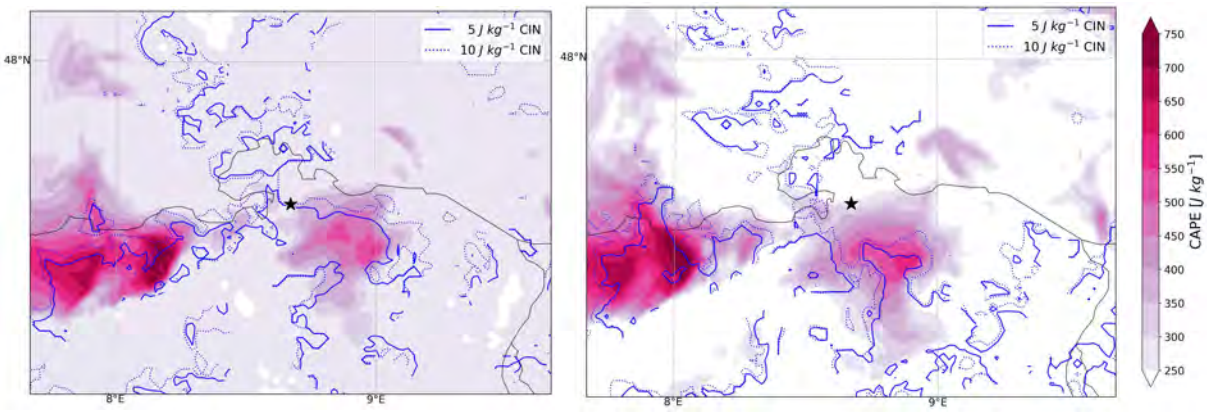

Figure 5.4.4: Horizontal map of Convective Available Potential Energy (CAPE) [J kg^{-1}] and 5 and 10 J kg^{-1} contour lines (solid and dotted blue) of Convective Inhibition (CIN) [J kg^{-1}] on 10.05.2018 at initiation time 01:00 UTC (left) and 30 minutes before initiation 00:30 UTC (right) with initiation location (8.67235° E, 47.629° N, asterisk) for northeastern Switzerland.

to 7.5 km) during the initiation (Figure 5.4.1g), but stronger after the initiation. Then, the mean of the trajectories experiences a strong ascent from 4.5 to 7.75 km altitude in the last 2.5 hours before the trajectories started (Figure 5.4.1i). In the eight hours, the mean of the trajectories with starting heights between 2.5 to 6 km (orange) increase from 3 to 4.25 km before thunderstorm initiation. This ascent is slightly stronger during the initiation (2.75 to 4.25 km) and weaker after the initiation (3 to 4 km). The only remarkable pattern along the lowest trajectories (SFC up to 2.5 km starting height) occurs after the initiation (Figure 5.4.1i). During the 8 hours, the mean of the trajectories first slightly increases until 4.5 hours before the initiation (1.5 to 1.75 km) and then decreases to 1.25 km altitude in the remaining hours.

On the VCS of RH (see Figure 5.4.2, left), maximum values (90-100 %) of RH are present in the mid-troposphere (1.5 up to 7 km altitude). Further, the RH ranges between 60 and 80 % in the PBL (SFC up to 1 km). The temporal evolution figure (see Figure 5.4.2, right) reveals an increase in RH from 30-40 to 70-90 % in the lower troposphere (SFC up to 1.6 km) until the thunderstorm initiation (-8 until 0 hours). Starting from 7.5 hours until the thunderstorm initiation, an slight increase in RH (70-80 to 90-100 %) is detectable in the mid-troposphere (1.6 up to 3.1 km). In addition, RH increases

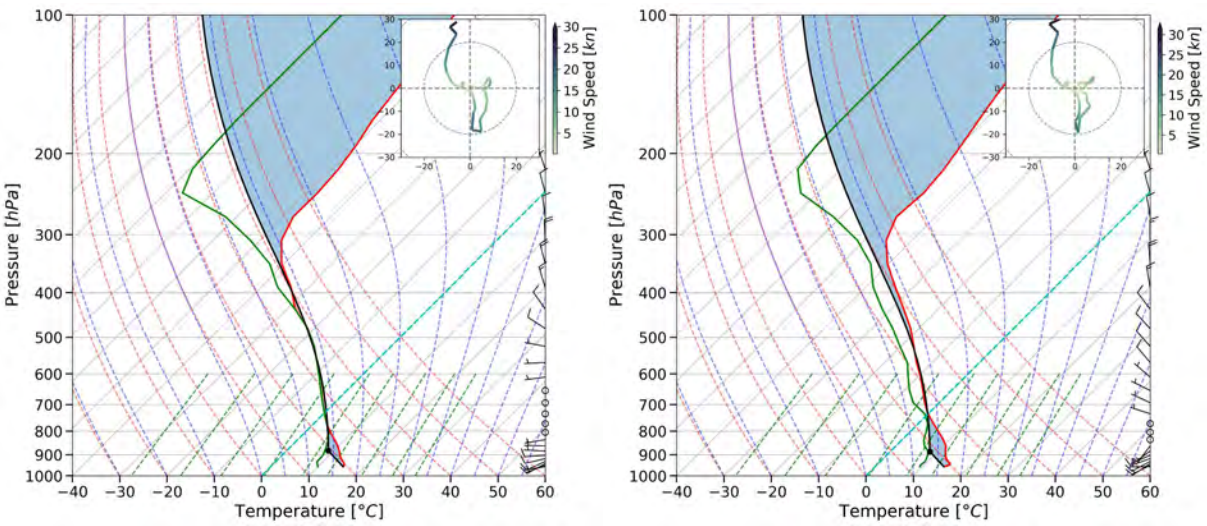

Figure 5.4.5: Skew T-log p diagram at location of initiation (8.67235° E, 47.629° N) on 10.05.2018 at initiation time 01:00 UTC (left) and 30 minutes before initiation 00:30 UTC (right). See Figure 5.1.5 for description.

the strongest (20-30 to 80-90 %) in the upper troposphere (3.1 up to 9.8 km) from 8 until 3 hours before the initiation. The tracing of WVMR along the trajectories is shown on Figure 5.4.3. The amount of water vapour decreases with increasing starting height of the trajectories. The trajectories with lower starting heights (SFC up to 2.5 km) have a high WVMR (6-8 g kg^{-1}, Figure 5.4.3d). The WVMR along the highest trajectories (6 up to 10 km) decrease in all three time steps. The strongest decrease can be seen after the initiation (Figure 5.4.3i), when the WVMR drops from 4.5 to 0.5 g kg^{-1} (-8 until 0 hours). In the mid-troposphere, the decrease is the strongest (0.5 g kg^{-1}) in the last hour (during the initiation, Figure 5.4.3h) and half an hour (after the initiation, Figure 5.4.3i). During and after the initiation, an increase of 0.5 g kg^{-1} in the WVMR can be detected in the lowest trajectories (SFC up to 2.5 km).

At the time of initiation, CAPE is small (below 250 J kg^{-1}) in the initiation area (see Figure 5.4.4, left) and the contour line of 5 and 10 J kg^{-1} CIN (solid and dotted blue) pass through the location of thunderstorm initiation (asterisk). The CIN values have decreased (from >10 J kg^{-1}) since 1 hour before the storm. In this time period, CAPE built up slightly (250-300 J kg^{-1}, see Figure 5.4.4, right) and decreased again until the time of initiation (to the aforementioned value). By looking at the CAPE and CIN areas, I detected this evolution in the pre-storm environment also in the skew T-log p diagrams of Figure 5.4.5. The CIN area is smaller at the time of initiation (see Figure 5.4.5, left) compared to 30 minutes before (see Figure 5.4.5, right). The built up of CAPE is only 15 minutes before the initiation better visible in the skew T-log p diagrams. During the initiation (see Figure 5.4.5, left), the mid-tropospheric layer (SFC up to 450 hPa) is saturated, which was not the case 30 minutes before (see Figure 5.4.5, right). Close to the surface, the simulated absolute temperature (red) shortly increases with height implying the presence of a temperature inversion. The inversion was more pronounced in the hour before the initiation and the strongest 30 minutes before the thunderstorm initiation (see Figure 5.4.5, right). This coincide with the highest CIN values (blue shade in lower troposphere). By analysing the lapse rate of the simulated absolute temperature (red) at this time step, I could detect a conditional unstable layer (up to 750 hPa) above the inversion. Finally, the wind barbs together with the hodograph indicate a change in wind direction with height.

Figure 5.4.6 shows the Theta-E values along the VCS (left) and their evolution over time at the initiation location and its surroundings (right). Lower Theta-E values (312-313 K) are stratified over higher values (317-318 K) on the surface. This vertical gradient is stronger (310-311 over 317-318 K) south of the initiation location (red tick on x-axis) and some of these lower Theta-E values intrude into the lower parts of the troposphere. The intensification of the vertical Theta-E gradient started approximately

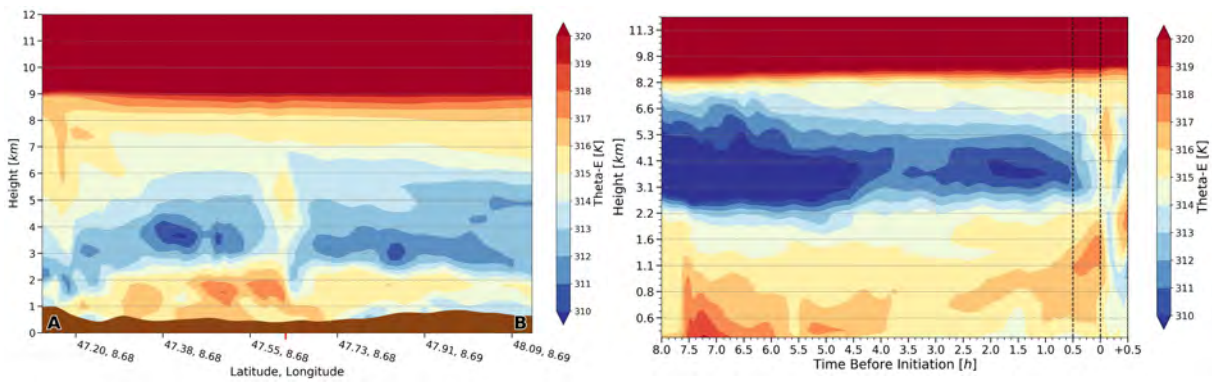

Figure 5.4.6: Left: Vertical cross-section (VCS) of equivalent potential temperature (Theta-E) [K] on 10.05.2018 at 01:00 UTC. VCS in north-south direction with initiation location indicated by red tick on x-axis, starts at A (8.67235° E, 47.129° N) and ends at B (8.67235° E, 48.129° N). Right: Temporal evolution of Theta-E [K] at the location of initiation (8.64449° E, 47.5522° N) and its surroundings until 8 hours before the thunderstorm initiation (see above). Vertical dashed lines indicate 30 minutes before, during and after the initiation time (starting times of trajectories).

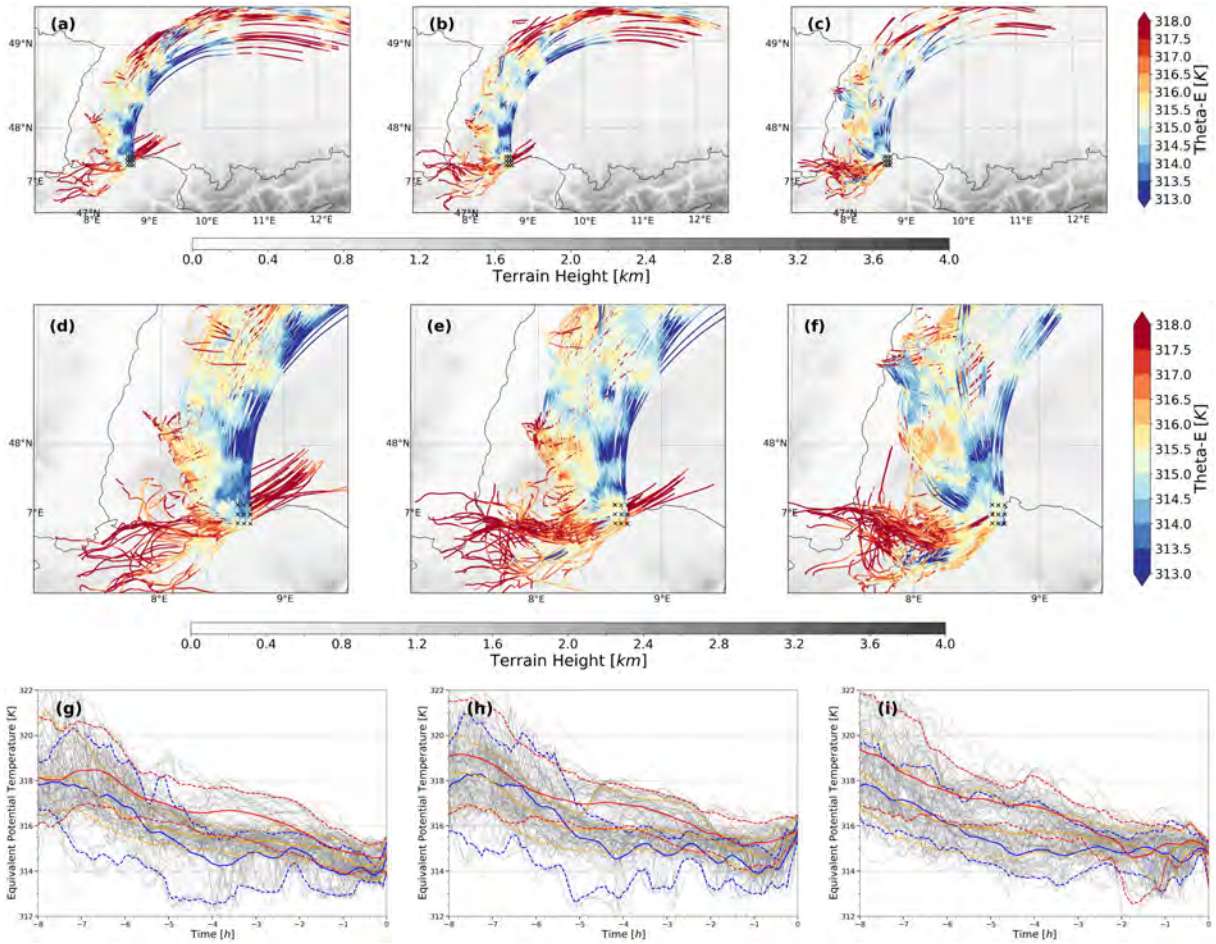

Figure 5.4.7: Same as Figure 5.4.1, but for equivalent potential temperature (Theta-E) [K].

2.5 hours before the initiation. The calculated trajectories of Theta-E are presented in Figure 5.4.7. Therein, one could detect higher Theta-E values along the lower trajectories approaching from southwest (317-318 K) and lower Theta-E values along trajectories in bigger altitude (313-314 K). By looking at the situation before (Figure 5.4.7d), during (Figure 5.4.7e) and after (Figure 5.4.7f) the initiation, Theta-E of the higher starting trajectories increases (313-314 to 315-316 K, i.e. higher temperature and/or moisture content), while it decreases for the lower trajectories approaching from southwest (317-318 to 315-316 K, i.e. lower temperature and/or moisture content). In addition, by following these trajectories from southwest, an area of low Theta-E (313-313.5 K) can be seen in the southwest of the initiation location. What on the temporal evolution panels (Figure 5.4.7g-i) is obvious, are the decreasing mean values of all atmospheric layers by reaching the time of initiation. The mean from the highest trajectories (6 up to 10 km, blue) is most of the time lower compared to the means of the other layers (orange and red). The mean of the lowest trajectories (SFC up to 2.5 km, red) is concurrently mostly higher than the other layers aloft (orange and blue).

The maximum updraft along trajectories (see Figure 5.4.8) indicates some higher updrafts (>5 m s^{-1}) along the lowest and highest trajectories. These areas of updrafts are located southwest and north-northwest of the initiation area (Figure 5.4.8a). Compared to this situation, the spatial distance between the updraft areas and the initiation area gets smaller after the initiation (Figure 5.4.8c). This evolution for the lower trajectories southwest gets also visible in the panels of the trajectories up to 6 km (Figure 5.4.8d-f). Moreover, during the thunderstorm initiation, a strong updraft signal (>5 m s^{-1}) is detectable in the west and northwest area of the initiation (area between the crosses). This pattern relocates 30

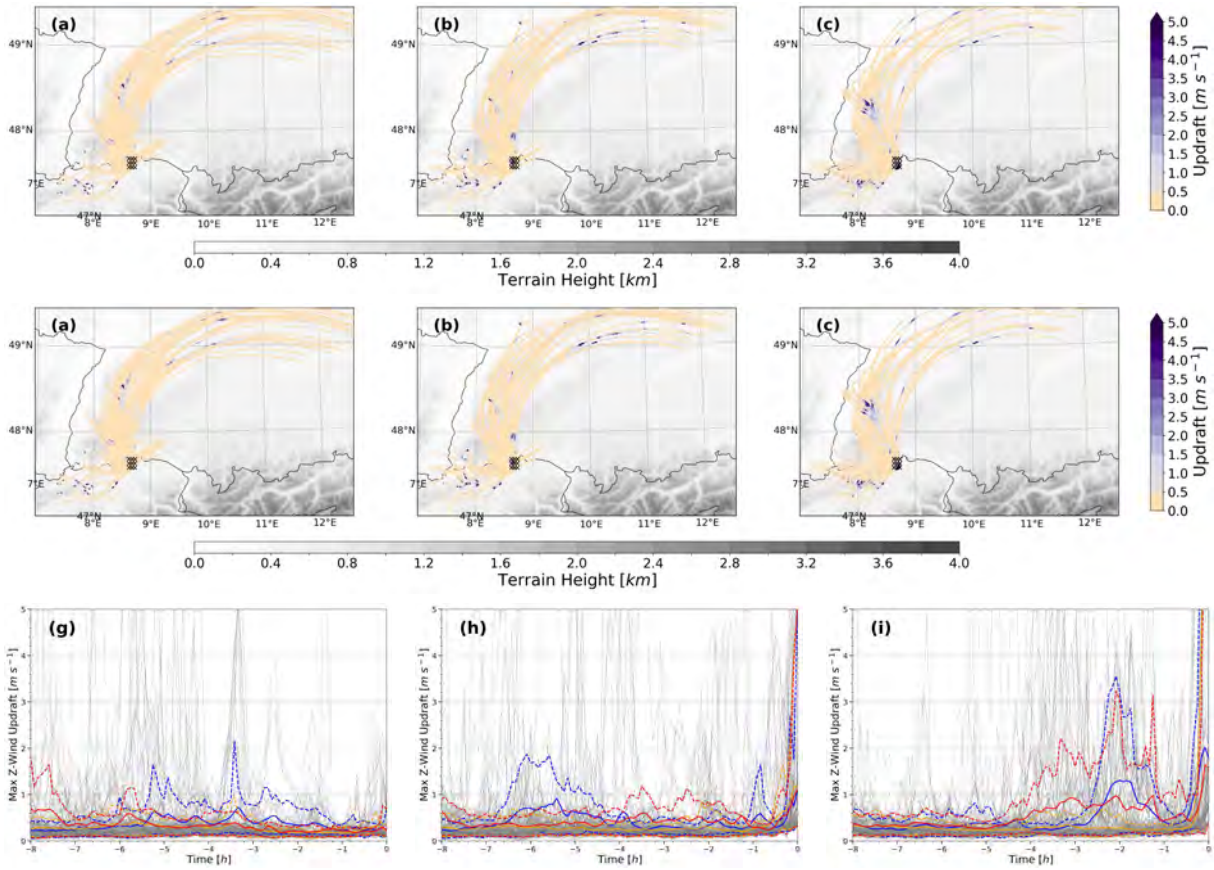

Figure 5.4.8: Same as Figure 5.4.1, but for maximum z-wind updraft [m s^{-1}].

minutes after the initiation to the south and southeast initiation area. The signals of the above-mentioned updraft areas (higher means of red and blue) can also be detected in the temporal evolution panel (Figure 5.4.8i).

At the initiation area on altitude of 850 hPa, a southwesterly wind was blowing with a wind speed gradient (>8 to <3 m s^{-1}) and a change in direction (southwest to west) close to the initiation location (see Figure 5.4.9, left). In the areas southwestwards of the initiation location, a vertical wind shear (10 m s^{-1}, pink) is discernible (see Figure 5.4.9, right). Further, negative divergence values (-0.8 to -1.0 10^{-3}

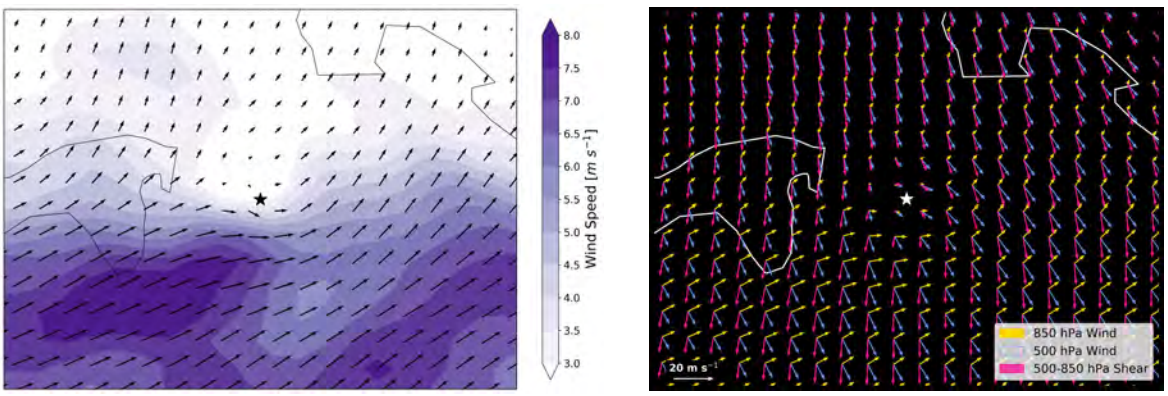

Figure 5.4.9: Left: Horizontal map of wind speed [m s^{-1}] and direction @ 850 hPa on 10.05.2018 at 01:00 UTC with initiation location (8.67235° E, 47.629° N, asterisk) for northeastern Switzerland. Right: Horizontal map of vertical wind shear on time and location of initiation (see above) for northeastern Switzerland. The map contains wind speed @ 850 hPa (yellow), wind speed @ 500 hPa (blue) and the 500 - 850 hPa vertical wind shear (pink).

s^{-1}) are found directly southwards of the initiation location (see Figure 5.4.10, left). Finally, low Theta-E values (311-312 K) are located south-southwestwards of the initiation location (see Figure 5.4.10, right).

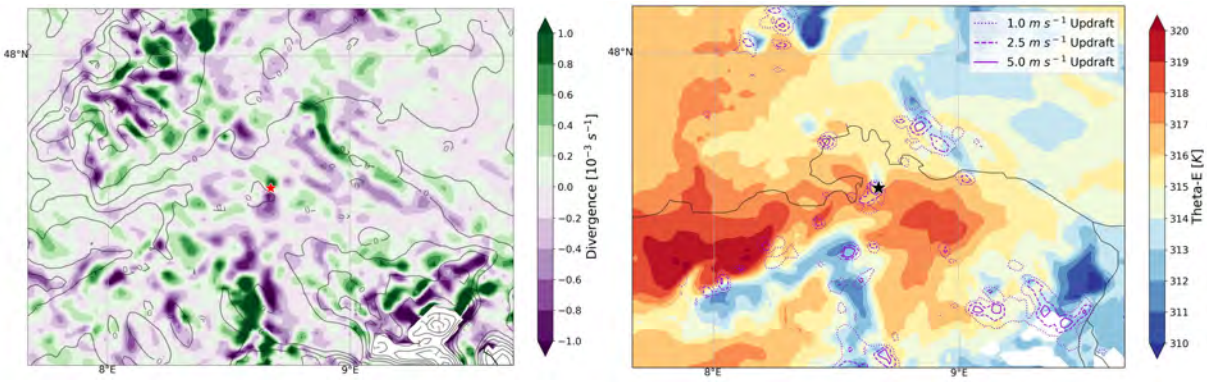

Figure 5.4.10: Left: Horizontal map of wind divergence @ 850 hPa [10^{-3} s^{-1}] on 10.05.2018 at 01:00 UTC with initiation location (8.67235° E, 47.629° N, asterisk). The contour lines indicate the terrain height [km] for the area of northeastern Switzerland. Right: Horizontal map of equivalent potential temperature (Theta-E) @ 850 hPa [K] on time and location of initiation (see above) for northeastern Switzerland.

Hence, the analysis of this case study revealed a northward turn of the trajectories with increasing starting height. The lowest trajectories have a southwesterly direction of approach. Mostly throughout the atmosphere, high values of RH were present (90-100 %), which is the result of an increase of RH until the thunderstorm initiation (from 30-40 %). The trajectories on the lowest levels (SFC up to 2.5 km) carried the most amount of water vapour to the area of initiation (6-8 g kg^{-1}). The values of CAPE and CIN were both small (250-300 and >10 J kg^{-1}) and decreased until the time of initiation (<250 and 5-10 kg^{-1}). The skew T-log p diagram indicated a temperature inversion directly above the surface, a saturated mid-troposphere (SFC up to 450 hPa) and a conditional instability above the inversion present (up to 750 hPa). Further, lower Theta-E values (312-313 K) are stratified above higher Theta-E values (317-318K). This inversion of the vertical Theta-E gradient intensified before the thunderstorm initiation and resulted in a potential instability. In the aforementioned area of low Theta-E values, the updraft values are strong (>5 m s^{-1}) after the initiation of the thunderstorm. Lastly at the location of initiation, a southwesterly wind was blowing on the 850 hPa altitude level. In this southwest direction from the initiation location, I could detect a strong vertical wind shear (10 m s^{-1}), negative divergence values (-0.8 to -1.0 10^{-3} s^{-1}) and low Theta-E values (311-312 K).

The output from the different analysis tools indicate a high amount of moisture present in the atmosphere (from SFC up to upper troposphere high RH, 90-100 %). This moisture was transported into the area before the initiation and originated from the southwest (high WVMR, 6-8 g kg^{-1}). The air parcels from this area transported the moisture along the trajectories on the ground levels to the initiation location (SFC up to 2.5 km). This moisture transport resulted in a saturated atmosphere at the time and location of thunderstorm initiation (90-100% RH in VCS and saturation in skew T-log p diagram). Therefore, a substantial amount of ground level moisture was available and this basic ingredient is satisfied.

CAPE was low (maximum of 300-350 J kg^{-1}, 15 minutes before the initiation) and decreased until the thunderstorm initiation (<250 kg^{-1}). At the same time, CIN was larger than 10 J kg^{-1} (until 20 minutes before the initiation), but decreased as well until the initiation of the thunderstorm (5-10 kg^{-1}). The increase of the simulated absolute temperature with height close to the surface describes the prevalence of an inversion. Due to this temperature inversion in the PBL, CIN could built up and was an half an

hour before the thunderstorm initiation the most pronounced. The same holds true for the inversion (altitude of temperature increase). There was a conditional unstable layer above the inversion in the lower troposphere (up to 750 hPa). This finding is supported by the potential instability caused by the inversion of the vertical Theta-E gradient, which intensified before the initiation. Based on these findings, I can determine a conditionally unstable atmospheric stratification above the capping inversion at the time of thunderstorm initiation. Hence, the basic ingredient of conditional instability is met, but the triggering mechanism needs to be strong enough to overcome the capping inversion.

The trajectories of height, wind barbs and hodograph on the skew T-log p diagram displayed a directional vertical wind shear with increasing altitude. Further, this was complemented with the horizontal map of the vertical wind shear, which indcates high vertical wind shear between 850 and 500 hPa (10 m s^{-1}). Therefore, the wind fields can be assessed as favourable for strong deep convection.

The search after this triggering mechanism led me to the trajectories of updraft and Theta-E. They showed an area southwest of the initiation area with high updraft (>5 m s^{-1}) and low Theta-E values (311-312 K), which are characteristics of ongoing convection in this area. With a southwesterly wind, the downdrafts accumulated in a cold pool are advected to the initiation location (detection based on horizontal maps of Theta-E at 850 hPa in the pre-storm environment). With negative divergence values (-0.8 to -1.0 10^{-3} s^{-1}), there could initiate the thunderstorm. In the following, the vertical wind shear (10 m s^{-1}) enables the thunderstorm to persist over a longer time period. With the approaching cold pool and its gust front from the southwest, the convection of the thunderstorm gets intensified and it reaches 20 minutes after the initiation the strongest reflectivity values. Initially the convergence and hence the cool pool gust front are the most plausible triggers for the initiation of the thunderstorm in this case study.

5.5 Case Study V

The last case study covers the weakest thunderstorm with 57.5 dBZ (rounded, but smaller value than Case Study IV), which initiated on 30.05.2018 at 14:50 UTC over southwestern Switzerland (6.95974°E, 46.4482°N, see Figure 4.1.1 for case study location). The initiation location lies close to the eastern tip of Lake Geneva in the Vaud Alps (see Figure 7, Appendix for more spatial information). In Figure 5.5.1, a distinction is clearly visible between the low starting trajectories (SFC up to 4 km, brown) and the ones from higher altitude (4 up to 10 km, green). The air parcels following low trajectories (SFC up to 2 km) approach the initiation area from the north, while the higher air parcels approach from the southeast (2

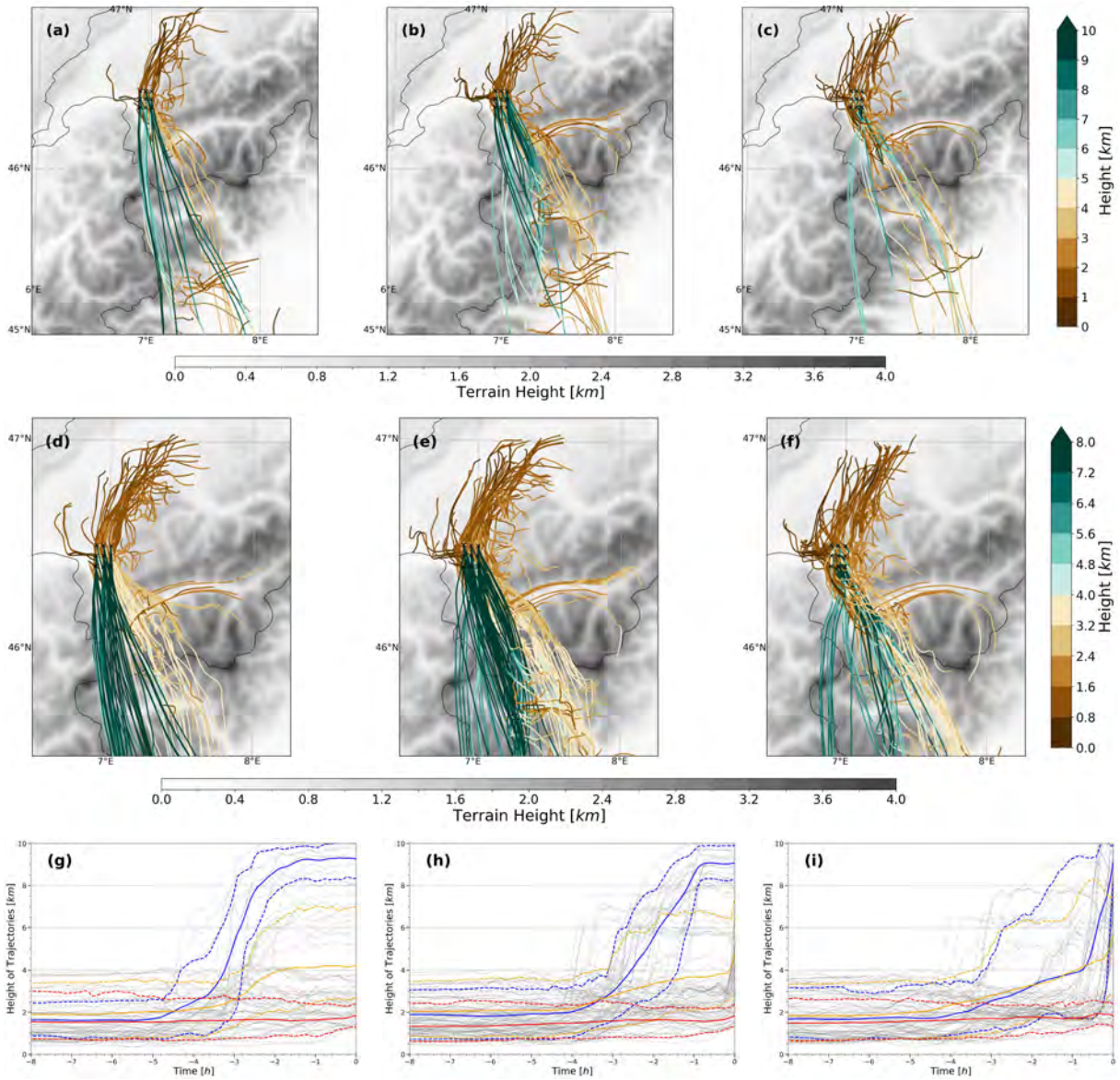

Figure 5.5.1: Height [km] along 8 hours backwards calculated trajectories started 30 minutes before (left), during (middle) and 30 minutes after (right column) thunderstorm initiation (30.05.2018 - 14:50 UTC). The starting points of the trajectories consist of the initiation location (6.95974° E, 46.4482° N) and 8 starting points 0.05° in each direction (crosses). The background of the panels in the upper two rows represents the terrain height [km] for the area of southwestern Switzerland. (a)-(c): Horizontal maps of trajectories with starting heights every 100 m from surface (SFC) up to 10 km (every 5th trajectories is plotted). (d)-(f): Horizontal maps of trajectories with starting heights every 100 m from surface up to 6 km (every 2nd trajectories is plotted). The figures show a smaller spatial extent, compared to the figures of the first row. (g)-(i): Temporal evolution along trajectories separated in three categories corresponding to their starting height: SFC up to 2.5 km (red), 2.5 up to 8 km (orange) and 8 up to 10 km (blue) with solid (dashed) lines for mean (10th and 90th percentile).

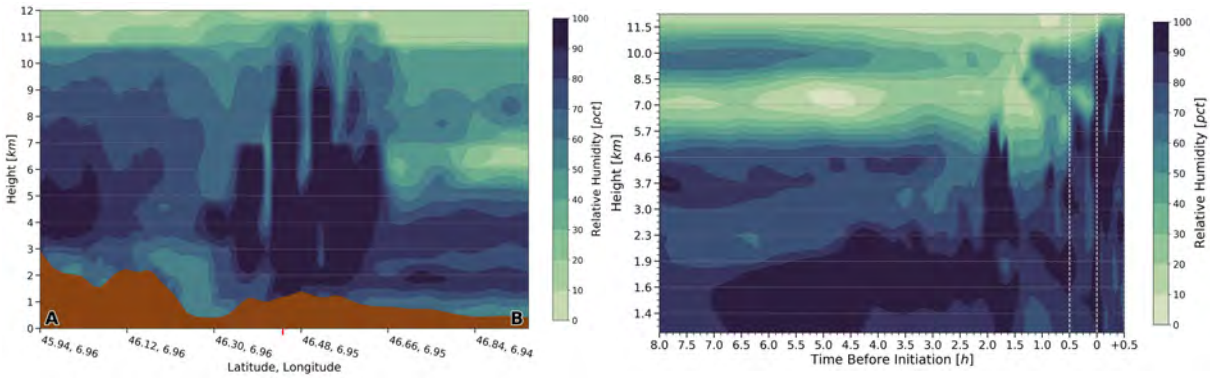

Figure 5.5.2: Left: Vertical cross-section (VCS) of relative humidity (RH) [%] on 30.05.2018 at 14:50 UTC. VCS in north-south direction with initiation location indicated by red tick on x-axis, starts at A (6.95974° E, 45.9482° N) and ends at B (6.95974° E, 46.9482° N). Right: Temporal evolution of RH [%] at the location of initiation (6.95974° E, 46.4482° N) and its surroundings until 8 hours before the thunderstorm initiation (see above). Vertical dashed lines indicate 30 minutes before, during and after the initiation time (starting times of trajectories).

up to 4 km) to south (4 up to 10 km). These high approach trajectories start in low altitudes (0-1 km) in the south before they ascent (5-7 km altitude) over the Alps. 30 minutes after the thunderstorm initiation (Figure 5.5.1f), more air parcels are traced in lower heights approaching from the west (0-1.6 km) and southeast (1.6-2.4 km). Furthermore, I detected a temporal shift in the ascent of the trajectories. Half an hour before the initiation (Figure 5.5.1g), the highest trajectories (8 up to 10 km, blue) start their ascent 5.5 hours before the initiation (1.5 km), which lasted 4 hours (until -1.5 h, 9.25 km). 30 minutes after the thunderstorm initiation (Figure 5.5.1i), the trajectories strongest ascend in the last hour (4 to 9 km). This means, that the trajectories started after the thunderstorm initiation make their major ascent later in comparison to before the initiation.

The atmospheric moisture content can be analysed by looking at the VCS of RH (see Figure 5.5.2, left). This vertical slice through the atmosphere indicates maximum RH (90-100 %) from the surface up to the upper troposphere (10 km altitude). Already hours before the initiation were such high RH values (90-100 %) present in most atmospheric layers (see Figure 5.5.2, right). Only in the lower troposphere, close to the surface, the RH values slightly decreased (to 70-80 %) two times until thunderstorm initiation. The traced WVMR along trajectories (see Figure 5.5.3) confirms the high amount of water vapour along all trajectories (>4.8 g kg^{-1} and up to 12 g kg^{-1}, higher WVMR compared to other case studies) besides those in high altitude (0-2.4 g kg^{-1}). This is during the initiation most recognisable (Figure 5.5.3c), when many air parcels with a high amount of water vapour (9-10 g kg^{-1}) reaches the initiation area from north, west and southeast. Also the temporal evolution panels (Figure 5.5.3g-i) show the increase of the WVMR along these trajectories from the surface up to 2.5 km (red). The increase is most pronounced (8.5 to 9.75 g kg^{-1}) before the initiation (Figure 5.5.3g) and less pronounced during the initiation (9 to 9.5 g kg^{-1}, Figure 5.5.3h). The mean of the trajectories from the other two layers (2.5 up to 8 km, orange and 8 up to 10 km, blue) decrease before (7 to 4.5 g kg^{-1}, -3.5 to -1.5 h, orange and 8 to 0.5 g kg^{-1}, -4.5 to -2 h, blue) and in the last 4 hours during the initiation (7 to 4 g kg^{-1}, orange and 7 to 0.25 g kg^{-1}, blue). This decrease of the WVMR along the higher trajectories (2.5 up to 10 km) is temporally coupled to the ascents detected before (Figure 5.5.1).

At the initiation location, CAPE values were very high (1850-2050 J kg^{-1} for Swiss conditions with a range between 340 to 2340 J kg^{-1}, see 1.1 State of Knowledge) half an hour before the time of initiation (see Figure 5.5.4, right). At the same location, CIN was small (smaller than 5 J kg^{-1}), but right next to the 5 and 10 J kg^{-1} contour lines. Starting from these contour lines, an area with higher CIN values (>10 J kg^{-1}) encloses the thunderstorm initiation location from west to south. These high CAPE values

were built up locally at the location of initiation. At the same time, CIN was smaller than 5 J kg^{-1}, but not always zero (see Figure 5.5.5, right). This small area of CIN disappeared afterwards until the thunderstorm initiation and CIN is smaller than 5 J kg^{-1} at the time of initiation (see Figure 5.5.4, left). Further, I noticed in this pre-storm environment analysis, how stable high (always >1450 J kg^{-1}) the CAPE values were in this time period. But 15 minutes before the initiation, they began to decline and 1450-1650 J kg^{-1} were remaining at the time of initiation (see Figure 5.5.4, left). On the skew T-log p diagram, a dry layer in the mid-troposphere (600 up to 400 hPa) is detectable 30 minutes before the initiation (see Figure 5.5.5, right), which got saturated up to 300 hPa (see Figure 5.5.5, left). One can also detect the change in wind direction by means of the wind barbs and the hodograph, which was more pronounced half an hour before the initiation in the lower troposphere (see Figure 5.5.5, right). Moreover in a lower tropospheric layer (800 up to 600 hPa) above a small temperature inversion, a conditional instability was present until 5 minutes before the initiation.

On the VCS of Figure 5.5.6 (left), high Theta-E values (331-332 K) can be detected in the boundary layer (SFC up to 2 km). On the other hand, the Theta-E values (322-323 K) in the mid-troposphere

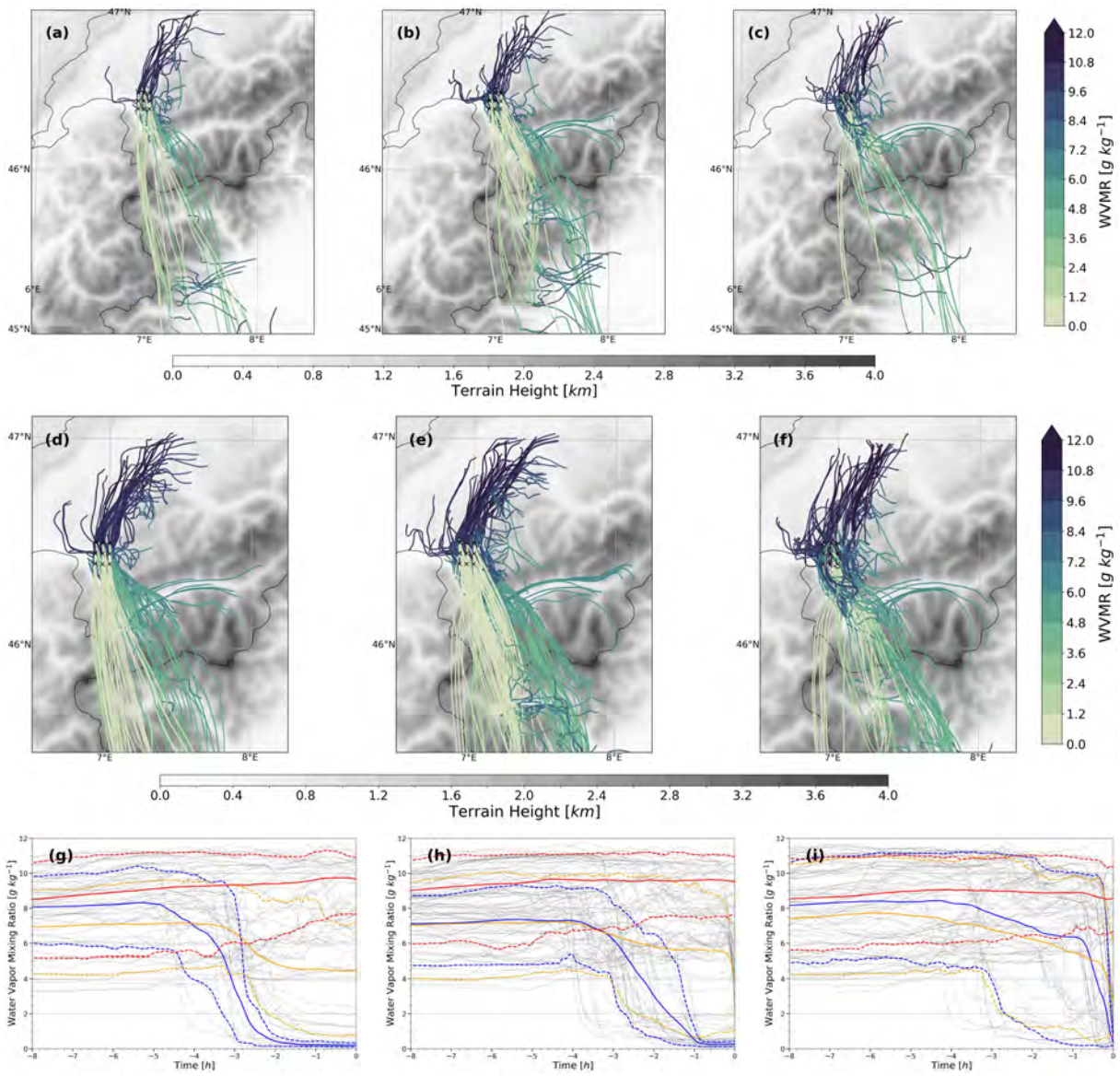

Figure 5.5.3: Same as Figure 5.5.1, but for water vapour mixing ratio (WVMR) [g kg^{-1}].

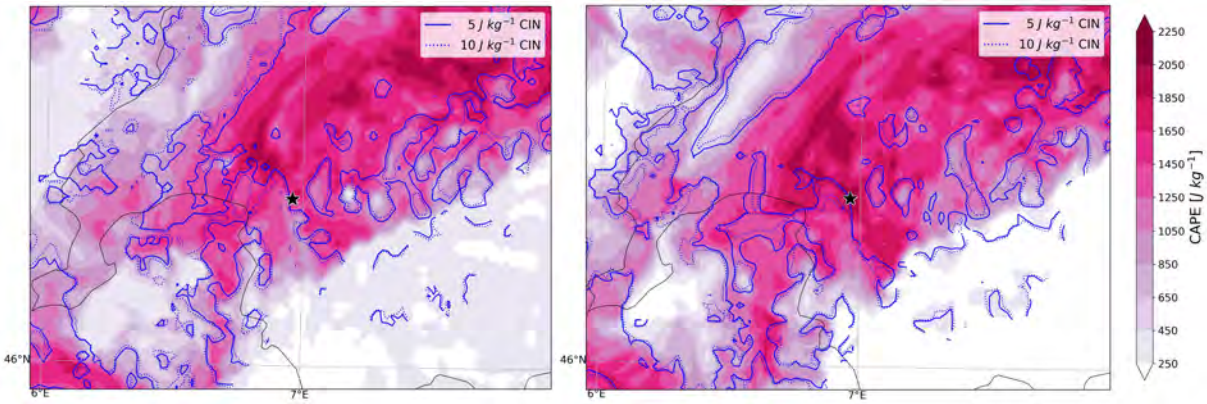

Figure 5.5.4: Horizontal map of Convective Available Potential Energy (CAPE) [J kg^{-1}] and 5 and 10 J kg^{-1} contour lines (solid and dotted blue) of Convective Inhibition (CIN) [J kg^{-1}] on 30.05.2018 at initiation time 14:50 UTC (left) and 30 minutes before initiation 14:20 UTC (right) with initiation location (6.95974° E, 46.4482° N, asterisk) for southwestern Switzerland.

(2.5 up to 8 km altitude) are low. A strong vertical gradient is resulting due to this distribution of Theta-E trough the atmospheric layers. This gradient was building up (increase of Theta-E in PBL from 325-326 to 331-332 K) ever since the 8 hours before the initiation (see Figure 5.5.6, right). Since 3.5 hours before the initiation, the vertical Theta-E gradient is very strong and lost only a little bit of its strength during the time period from 2 to 1 hours before the initiation. On Figure 5.5.7a), the contrast along trajectories from the south is eye-catching. In the beginning, they traced low Theta-E values (326-327 K) and then suddenly high Theta-E values (335-336 K) closer to the initiation area. This pattern still holds during (Figure 5.5.7b) and after the initiation (Figure 5.5.7c). The trajectories on lower altitudes approaching from the north, have also low Theta-E values at their start (326-327 K). But after a shorter spatial distance, compared to the higher starting trajectories, their Theta-E values increased (335-336 K). Before (Figure 5.5.7d) and during (Figure 5.5.7e) the thunderstorm initiation, most of the arriving air parcels have high Theta-E values (335-336 K). In the temporal evolution of Theta-E along the trajectories (Figure5.5.7g-h), an increase in all layers is detectable from -8 to 0 hours. But during the increase along trajectories with starting height above 2.5 km (orange and blue), a sudden drop of Theta-E becomes clearly visible. This decrease corresponds to the decrease in WVMR (see Figure 5.5.3) and can

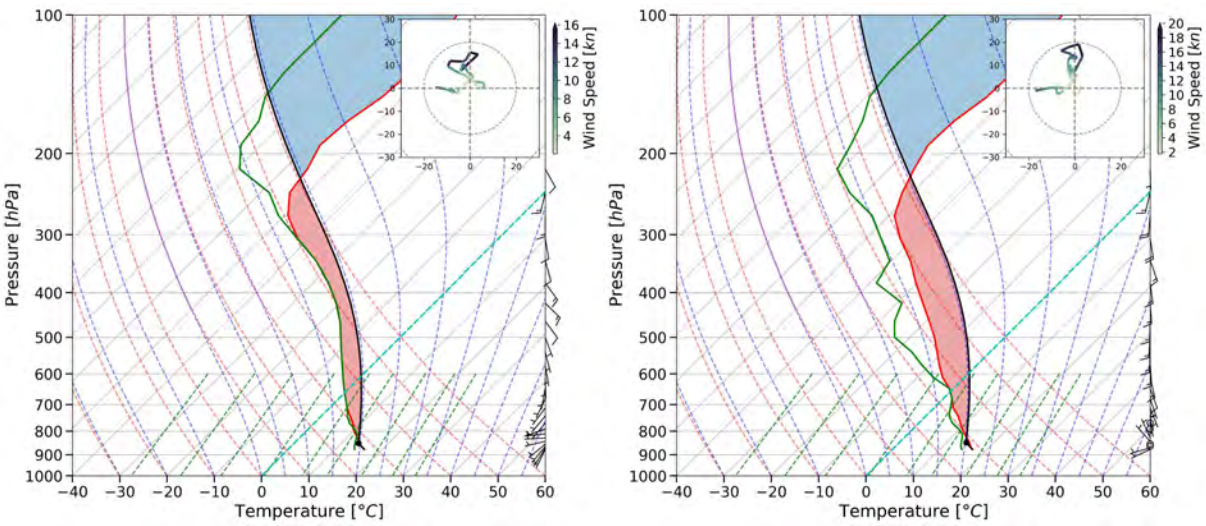

Figure 5.5.5: Skew T-log p diagram at location of initiation (6.95974° E, 46.4482° N) on 30.05.2018 at initiation time 14:50 UTC (left) and 30 minutes before initiation 14:20 UTC (right). See Figure 5.1.5 for description.

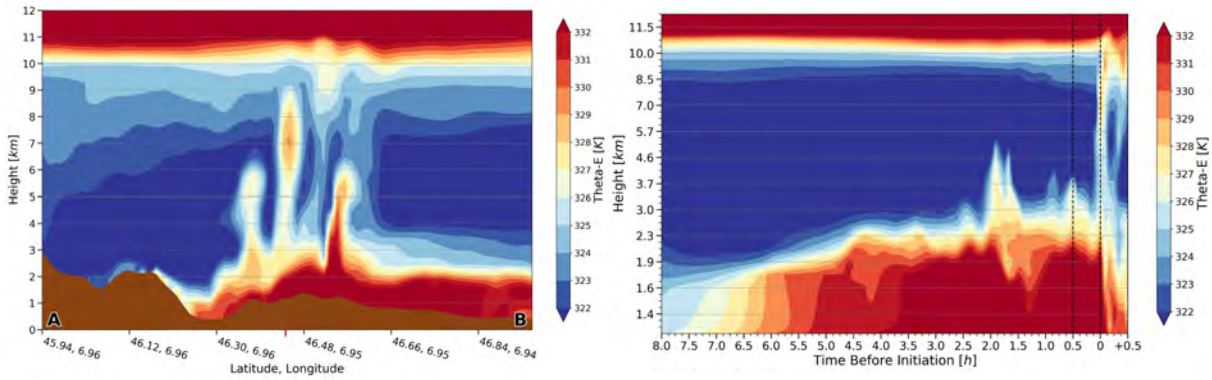

Figure 5.5.6: Left: Vertical cross-section (VCS) of equivalent potential temperature (Theta-E) [K] on 30.05.2018 at 14:50 UTC. VCS in north-south direction with initiation location indicated by red tick on x-axis, starts at A (6.95974° E, 45.9482° N) and ends at B (6.95974° E, 46.9482° N). Right: Temporal evolution of Theta-E [K] at the location of initiation (6.95974° E, 46.4482° N) and its surroundings until 8 hours before the thunderstorm initiation (see above). Vertical dashed lines indicate 30 minutes before, during and after the initiation time (starting times of trajectories).

be linked to the Alpine crossing of these higher trajectories (see Figure 5.5.1). In comparison along the lower trajectories (SFC up to 2.5 km, red), Theta-E increases more steadily during the approach of the initiation location.

Figure 8 (Appendix) shows the maximum updraft speed along trajectories. Before the initiation (Figure 8a), stronger updrafts (4-5 m s^{-1}) mostly occur along the higher approaching trajectories by their alpine crossing from the south. During the initiation (Figure 8b), such strong updrafts are detectable along more trajectories and their occurrence moves closer to the initiation area. In addition, strong updraft signals (>5 m s^{-1}) at the initiation location are detectable. After the initiation (Figure 8c), the updrafts are widespread and strong (>5 m s^{-1}) in the area of initiation. While during the initiation (Figure 8e) the strongest updrafts occur in the southern half of the initiation area, after the initiation (Figure 8f) also the starting points in the north experience strong updrafts. The trajectories with strong updraft values (>5 m s^{-1}) mostly approach from southeast. The temporal evolution panel from before the initiation (Figure 8g) clearly confirms the described updrafts along the highest trajectories (peak in blue mean, 8 up to 10 km). The trajectories with starting height from 2.5 up to 8 km (orange) have the strongest updraft values during the initiation (Figure 8h).

According to Figure 5.5.8 (left), a southwesterly wind was blowing at 800 hPa and accelerated at the location of initiation (from 3-4 to 5.5-6 m s^{-1}). In the atmospheric layers above the initiation location (asterisk), strong vertical wind shears between 800 and 500 hPa (pink) could be detected (10-15 m s^{-1}, Figure 5.5.8, right). The VCS of Omega (see Figure 5.5.9, right) shows the strong upwinds (<-15 Pa s^{-1}) above the initiation location (red tick on x-axis). The topography shown in the Omega VCS is complemented with the terrain height contours in Figure 5.5.9 (left). The thunderstorm initiated close to the eastern tip of Lake Geneva in the Vaud Alps. Finally, areas of strong negative divergence values (<-2.5 10^{-3} s^{-1}) at 800 hPa are located south- and northeastern of the initiation location at the top of the mountain ridge (see Figure 5.5.9, right).

Summarising the results of this case study, a separation became apparent between the lower (north) and higher starting trajectories (southeast to south). In the following research of the moisture content, I detected high values of RH (90-100 %) throughout the atmosphere and high amounts of water vapour (>4.8 and up to 12 g kg^{-1}) along all trajectories (except the highest from 8 up to 10 km). Further, there were high CAPE (1450-1650 J kg^{-1}) and small CIN values (<5 J kg^{-1}) at the time and location of thunderstorm initiation (CAPE was even higher half an hour before the initiation, 1850-2050 J kg^{-1}).

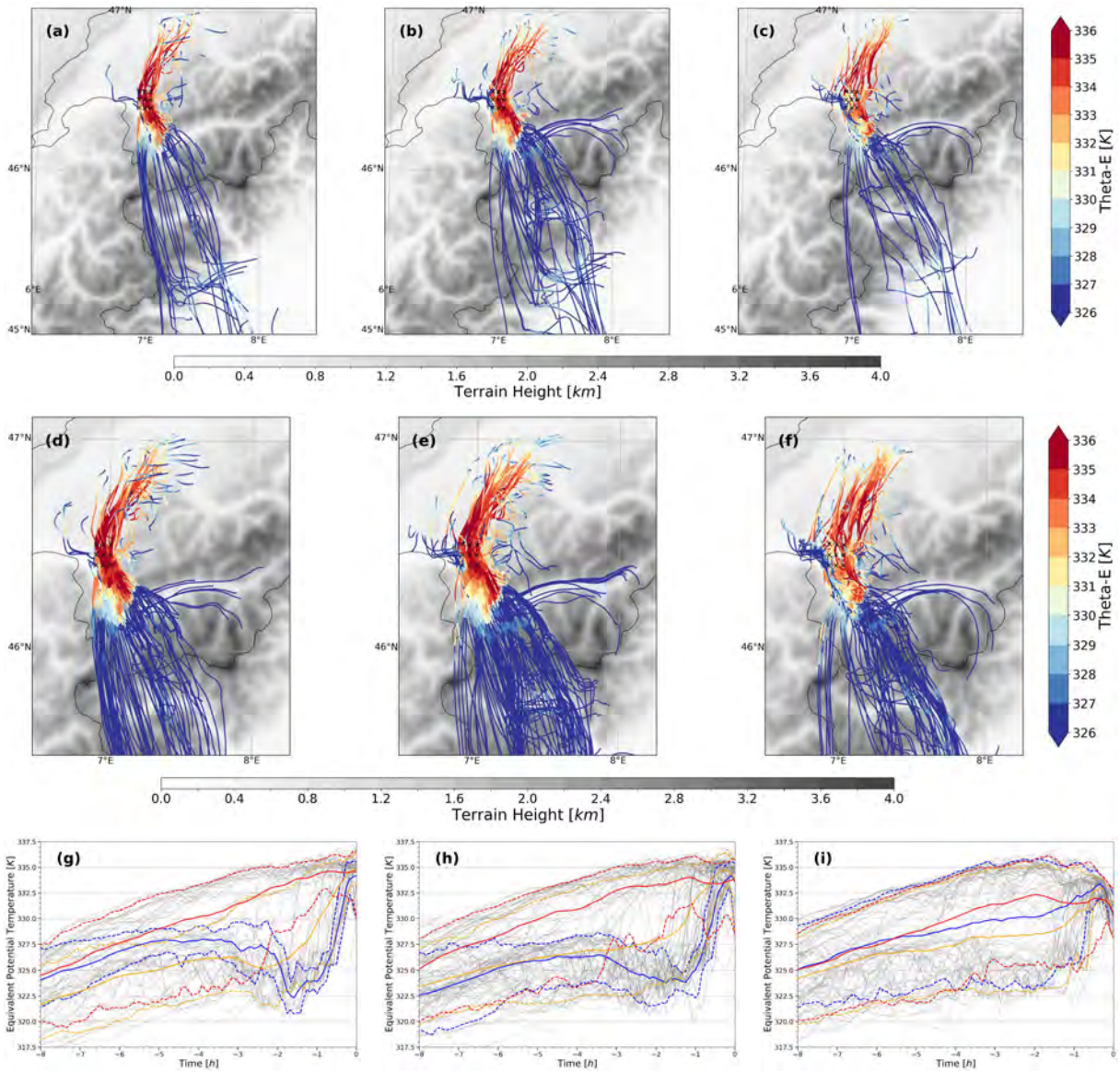

Figure 5.5.7: Same as Figure 5.5.1, but for equivalent potential temperature (Theta-E) [K].

A conditional instability was present in a lower tropospheric layer (800 up to 600 hPa). The analysis of the Theta-E stratification revealed lower Theta-E values (322-323 K) located over higher Theta-E values (331-332 K) resulting in a strong vertical gradient. Moreover, the strongest updraft signals (>5 m s^{-1}) spread from the southern part (before) to the northern part of the initiation area (after the initiation). At the location of thunderstorm initiation in the Vaud Alps, a strong southwesterly wind was blowing (5.5-6 m s^{-1}), intense upwind (<-15 Pa s^{-1}) as well as negative divergence signals (<-2.5 10^{-3} s^{-1}) could be detected.

Based on these results, I can explicitly assess the moisture content in the atmosphere during the thunderstorm initiation. The persistent high RH values (90-100 %) indicate a saturated atmosphere. The skew T-log p diagram confirmed this finding and the trajectories further showed the origin of this moisture. High amount of water vapour (8-10 g kg^{-1}) was found along the lower trajectories (SFC up to 2.5 km). Hence, the basic ingredient of a substantial amount of boundary-layer moisture is certainly fulfilled.

The high CAPE values (1850-2050 J kg^{-1}) indicate a high potential for possible strong convection.

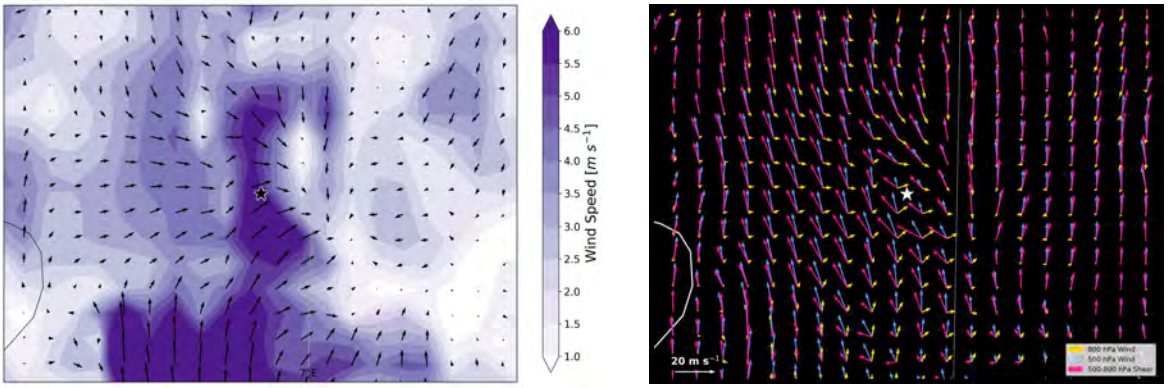

Figure 5.5.8: Left: Horizontal map of wind speed [m s^{-1}] and direction @ 800 hPa on 30.05.2018 at 14:50 UTC with initiation location (6.95974° E, 46.4482° N, asterisk) for southwestern Switzerland. Right: Horizontal map of vertical wind shear on time and location of initiation (see above) for southwestern Switzerland. The map contains wind speed @ 800 hPa (yellow), wind speed @ 500 hPa (blue) and the 500 - 800 hPa vertical wind shear (pink).

These CAPE values could build up, because the higher CIN values (>10 J kg^{-1}) west to south of the initiation location inhibited strong convection and hence the depletion of CAPE. But at the the initiation location, the CIN values were low (<5 J kg^{-1}) and convection could start without inhibition at the time of initiation. A sign for an unstable atmosphere delivers the inversion of the vertical Theta-E gradient and the resulting potential instability. In the pseudo-sounding, a layer was found with an inherent conditional instability (800 up to 600 hPa). These points led me to the conclusion, that the atmosphere was conditional unstable stratified and the basic ingredient for thunderstorm initiation was met.

On the skew T-log p diagram, the wind barbs indicate a directional wind shear with increasing altitude. This pattern could also detected by the comparison of the trajectories from different starting heights. Furthermore, strong vertical wind shears (10-15 m s^{-1}) were present according to the calculation between 800 and 500 hPa altitude levels. Based on these findings, I can infer favourable conditions for the evolution of thunderstorms with a long duration.

Lastly finding the triggering mechanism, a look at the terrain height contours on the divergence map gives a good indication. The thunderstorm initiated in the Vaud Alps close to Lake Geneva in the warmest time of the day (16:50 CET). The horizontal wind indicates a southwesterly flow along the topography and an acceleration in the area of initiation (from 3-4 to 5.5-6 m s^{-1}). This area is situated close to the

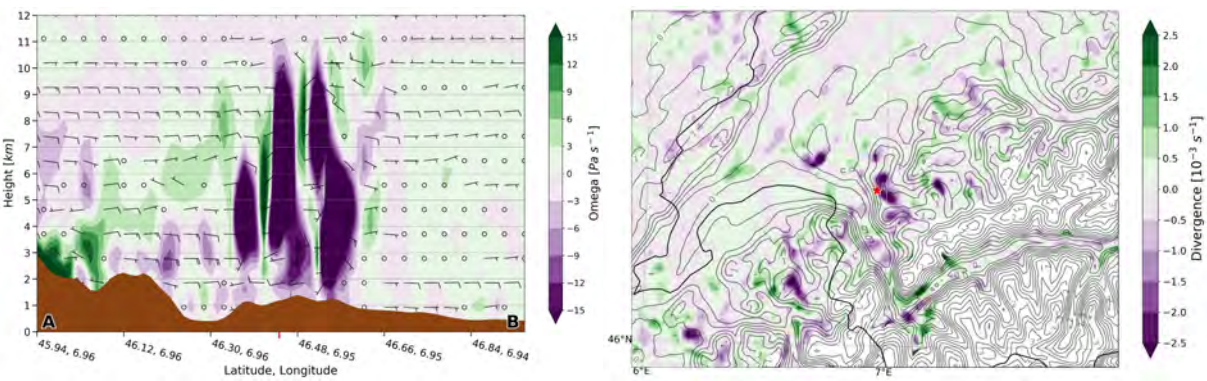

Figure 5.5.9: Left: Vertical cross-section (VCS) of vertical motion (Omega) [Pa s^{-1}] on 30.05.2018 at 14:50 UTC. VCS in north-south direction with initiation location indicated by red tick on x-axis, starts at A (6.95974° E, 45.9482° N) and ends at B (6.95974° E, 46.9482° N). Right: Horizontal map of wind divergence @ 800 hPa [10^{-3} s^{-1}] on time of initiation (see above) and with initiation location (6.95974° E, 46.4482° N, asterisk). The contour lines indicate the terrain height [km] for the area of southwestern Switzerland.

top of a mountain and experienced strong upwinds (<-15 Pa s^{-1}) due to strong airflow convergence (<-2.5 10^{-3} s^{-1}). The explanation for this pattern can be find in the diurnal mountain-valley wind system. This system describes the faster warming of mountain flanks and valleys compared to the lowlands in the course of the day. The warmer and less-dense air ascents along the mountain flanks and the airflow converges at the top of the mountain range. The ascending air needs to be replaced and therefore, an airflow sets in from the lowlands towards the mountains. Within the airflow, water vapour is transported from the lowlands to the mountains (explains the high amount of moisture, WVMR up to 12 g kg^{-1}), where convergence of the airflow occurs. This can lead to orographic convection and to the initiation of thunderstorms. Based on the discussed conditions and processes, the most plausible triggering mechanism of the thunderstorm in this case study is the orographic-related lifting.

5.6 Pre-Storm Environments of All Thunderstorms

To extract more generally valid patterns of the pre-storm environments, all thunderstorms identified by TITAN in the simulations of May 2018 and in end of the century climate conditions are analysed. The analysis (see 4.2 Pre-Storm Environments of All Thunderstorms) focused on the temporal evolution of different important variables for the initiation of thunderstorms. This evolution, up to 2 hours before the thunderstorm initiation, was investigated with 30 minutes time steps. For every time step, the variables were extracted at the initiation location of the thunderstorms (1 grid point). Figure 5.6.1 shows the mean of these variables at each time step for all the thunderstorm initiations in May 2018. Whereas, the surrogate climate change model data (see 3 Data) was used for the temporal evolution of the variables shown in Figure 5.6.2. In these climate conditions, TITAN identified 4311 thunderstorm initiations in contrast to 2686 thunderstorm initiations in May 2018. Note the varying axes limits between the two figures of the same variables. They are differing due to the ability for detecting the pattern of the temporal evolution. This would be impossible with consistent axis limits covering the magnitude of the variables from both climate conditions. In the following, the temporal evolution and the magnitude of the variables are first presented for May 2018 and for end of the century climate conditions accordingly. Afterwards, the changes will be emphasised between the two climate conditions.

The temporal evolution of CAPE (red), CIN (blue) and the WVMR at 850 hPa (grey) are shown in Figure 5.6.1a) for May 2018. From 120 until 60 minutes before the initiation, CAPE increases (473 to 489 J kg^{-1}) and CIN decreases (9.4 to 8.0 J kg^{-1}). A deceleration of this decrease is identifiable and CIN only slightly decreases until the next time step 30 minutes before initiation (7.9 J kg^{-1}). After peaking 1 hour before the initiation, CAPE begins its depletion. First, the decrease begins slowly until 30 minutes before the initiation (464 J kg^{-1}). But until the thunderstorm initiation, CAPE has considerably decreased (336 J kg^{-1}). In this last half an hour, CIN experiences also the biggest change by closely reaching the magnitude from 2 hours ago (9.2 J kg^{-1}). The WVMR at 850 hPa shows a temporal evolution without such pronounced changes. In the first 30 minutes, the WVMR increases (6.721 to 6.769 g kg^{-1}) and slightly decreases afterwards until the next time step (6.758 g kg^{-1}). This sequence is again repeated until the thunderstorm initiation, but with a stronger increase (6.828 g kg^{-1}) followed by a small decrease of the WVMR (6.826 g kg^{-1}).

In end of the century climate conditions (Figure 5.6.2a), CAPE values increase and peak already 90 minutes before the initiation (801 to 832 J kg^{-1}). Then the values slowly decrease for 60 minutes (822 J kg^{-1}) until they make a huge drop to the value at the initiation time (665 J kg^{-1}). A contrary pattern is detectable for CIN, which experiences a slow decrease (11.1 to 9.9 J kg^{-1}) and a strong increase in the last half an hour before the thunderstorm initiation (12.6 J kg^{-1}). The WVMR alternately increases and decreases, but the increasing changes are more pronounced. Hence, the WVMR is higher at the time of initiation (8.669 g kg^{-1}) compared to 120 minutes before (8.564 g kg^{-1}). For each variable, Table 2 presents the corresponding magnitude of mean, 10th and 90th percentile for May 2018 (blue) and end of century climate conditions (red).

By comparing the results of both climate conditions, the mean of CAPE strongly increases (mean of all time steps from 447.4 to 789 J kg^{-1}, +76.4 %) in end of the century climate conditions. Further, an increase is also detectable in the means of CIN (8.64 to 10.88 J kg^{-1}, +25.9 %) and WVMR (6.7804 to 8.6536 g kg^{-1}, +27.6 %). The pattern of the temporal evolution in the pre-storm environments of CAPE remains roughly the same. The only noteworthy difference can be detected in the time of the maximum value, which shifts from 60 to 90 minutes before thunderstorm initiation in end of the century climate conditions. The evolution pattern of CIN behaves as well similarly in both climate conditions. But in

end of century climate conditions, a stronger decrease from 120 to 60 minutes and a more pronounced increase can be detected in the last half an hour before thunderstorm initiation. Like in May 2018, WVMR increases also in future climate change conditions over time, but the pattern of the mean fluctuates more

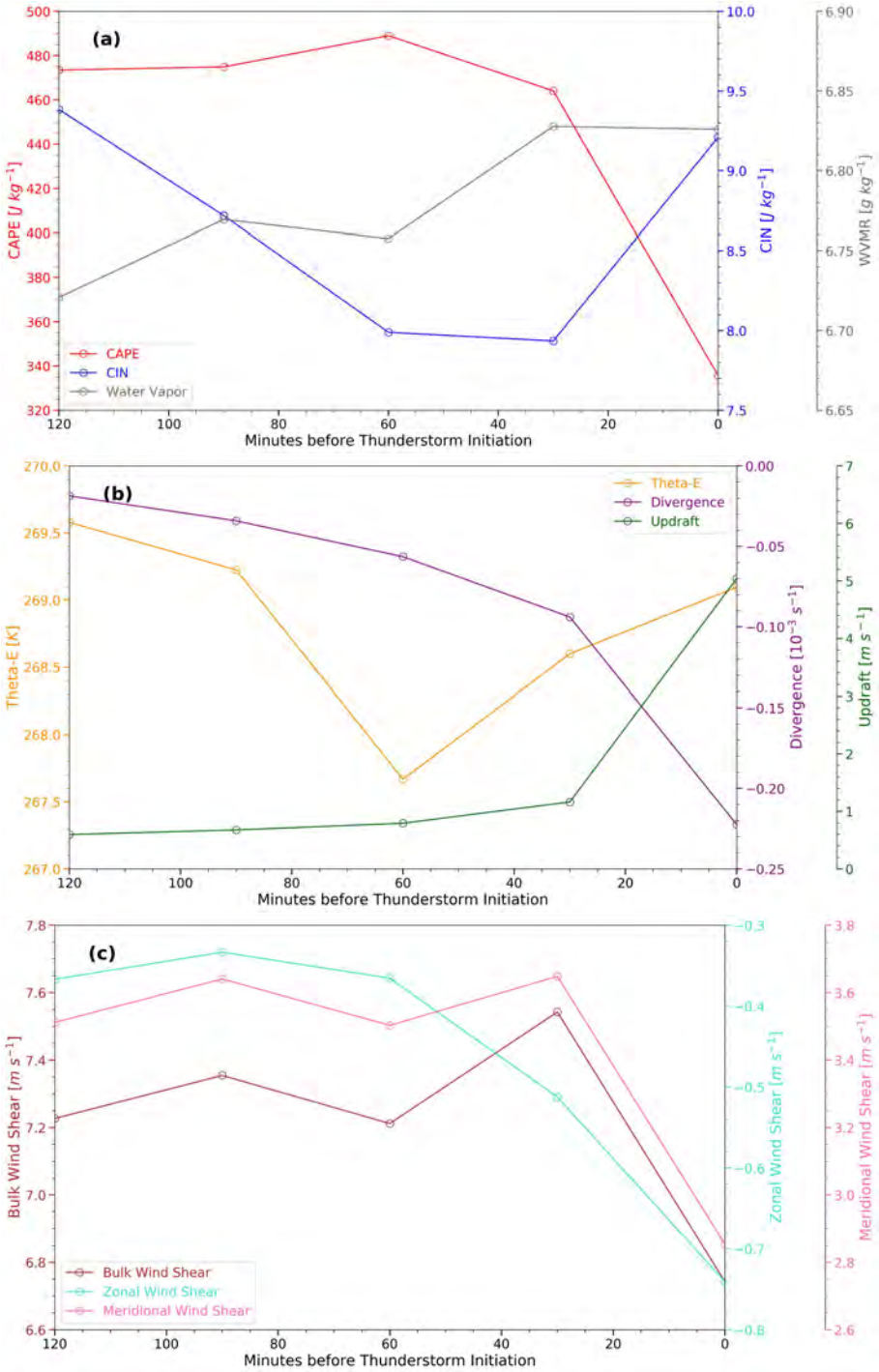

Figure 5.6.1: Temporal evolution of important variables in the pre-storm environments of all thunderstorms in May 2018. The evolution is analysed from the time of initiation until 2 hours before the initiation in 30 minutes time steps (circles). At each time step and for every thunderstorm initiation, the mean is calculated of the extracted variables at the respective location of initiation. (a): Temporal evolution of Convective Available Potential Energy (CAPE) [J kg^{-1}] (red), Convective Inhibition (CIN) [J kg^{-1}] (blue) and Water Vapour Mixing Ratio (WVMR) at 850 hPa [g kg^{-1}] (grey). (b): Temporal evolution of equivalent potential temperature (Theta-E) @ 850 hPa [K] (orange), horizontal wind divergence at 850 hPa [10^{-3} s^{-1}] (purple) and maximum updraft [m s^{-1}] (green). (c): Temporal evolution of Bulk wind shear 500 - 850 hPa [m s^{-1}] (brown), zonal wind shear 500 - 850 hPa [m s^{-1}] (turquoise) and meridional wind shear 500 - 850 hPa [m s^{-1}] (pink).

in the pre-storm environment.

Figure 5.6.1b) presents Theta-E at 850 hPa (orange), horizontal wind divergence at 850 hPa (purple) and maximum updraft (green). The temporal evolution of Theta-E for May 2018 (Figure 5.6.1c) reveals a decrease until 60 minutes before the initiation (269.58 to 267.67 K) and subsequently, an almost equivalent increase in the remaining hour until the thunderstorm initiation (269.1 K). The horizontal wind divergence steadily decreases (-0.019 to -0.094 10^{-3} s^{-1}) until an intensification of the decrease happens in the last 30 minutes before the initiation (-0.222 10^{-3} s^{-1}). The opposite is detectable for the maximum updraft speed, which means a slow increase (0.60 to 1.16 m s^{-1}) is followed by a strong increase in the last 30

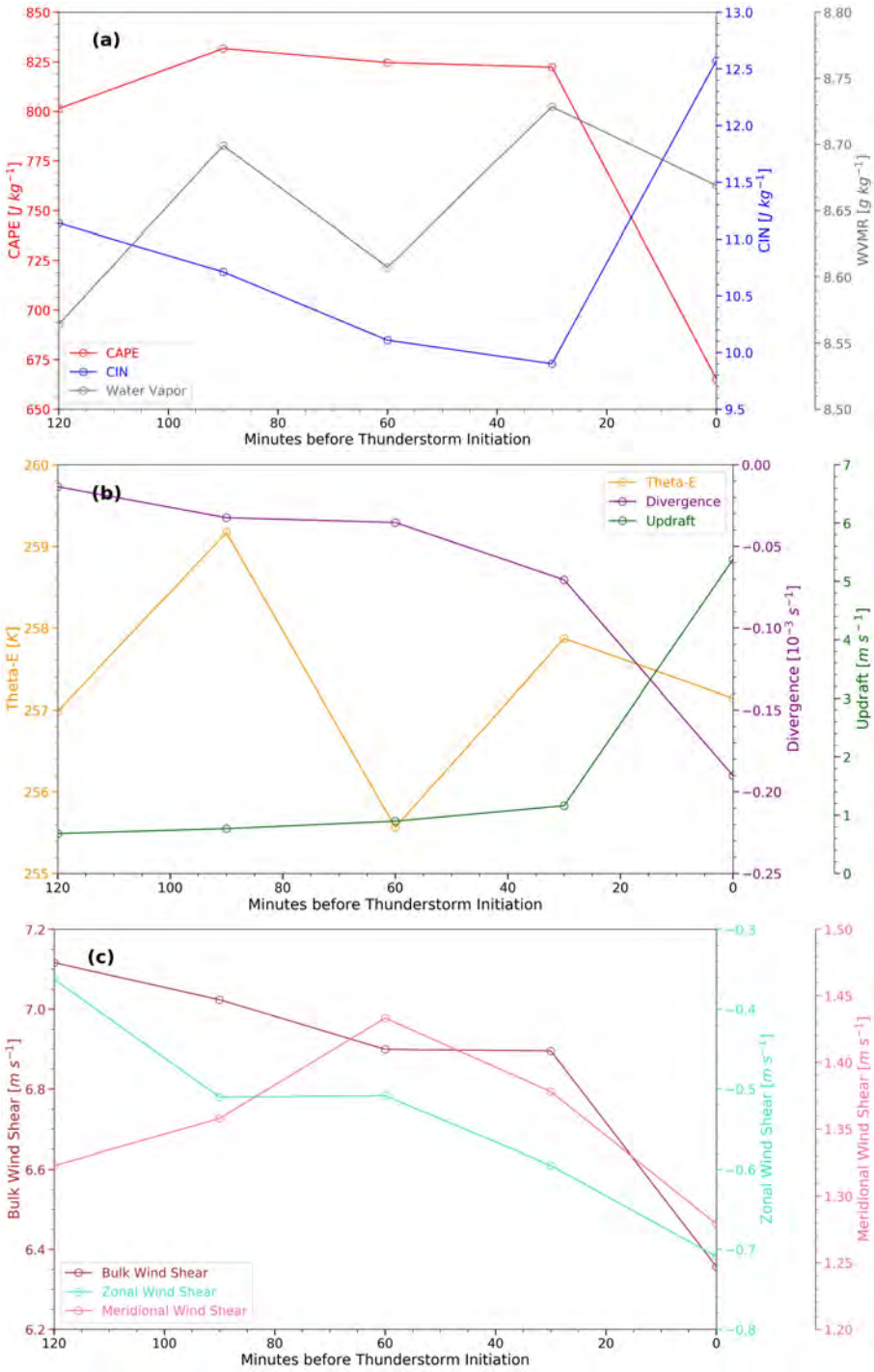

Figure 5.6.2: Same as Figure 5.6.1, but for end of the century climate conditions.

Table 2: Temporal evolution of the magnitude (mean, 10th and 90th percentile) of CAPE, CIN and WVMR @ 850 hPa for May 2018 and end of the century climate conditions:

Convective Available Potential Energy (CAPE) [J kg^{-1}]						
May 2018				**End of Century**		
10th %ile	**Mean**	**90th %ile**	**Minutes before Initiation**	**10th %ile**	**Mean**	**90th %ile**
47	473	1007	120	123	801	1573
48	475	1009	90	143	832	1618
50	489	1053	60	130	825	1611
38	464	998	30	123	822	1593
6	336	836	0	44	665	1402

Convective Inhibition (CIN) [J kg^{-1}]						
May 2018				**End of Century**		
10th %ile	**Mean**	**90th %ile**	**Minutes before Initiation**	**10th %ile**	**Mean**	**90th %ile**
0	9.4	28.0	120	0.1	11.1	31.4
0	8.7	27.1	90	0.1	10.7	29.3
0	8.0	24.0	60	0.1	10.1	27.9
0	7.9	24.0	30	0.1	9.9	27.3
0	9.2	31.3	0	0.0	12.6	36.5

Water Vapour Mixing Ratio (WVMR) @ 850 hPa [g kg^{-1}]						
May 2018				**End of Century**		
10th %ile	**Mean**	**90th %ile**	**Minutes before Initiation**	**10th %ile**	**Mean**	**90th %ile**
0	6.721	9.494	120	0	8.564	12.815
0	6.769	9.570	90	0	8.699	12.966
0	6.758	9.661	60	0	8.608	12.939
0	6.828	9.631	30	0	8.728	13.012
0	6.826	9.692	0	0	8.669	12.992

minutes before thunderstorm initiation (5.04 m s^{-1}).

In end of century climate conditions (Figure 5.6.2b), the temporal evolution of Theta-E is characterised by a continuously up and down of the mean value. This results in a strong increase (256.98 to 259.17 K), which is followed by an even stronger decrease (255.57 K). Next, Theta-E increases again (257.87 K) before decreasing with the smallest of all changes to the final value at the time of initiation (257.14 K). Horizontal wind divergence decreases almost steadily until half an hour before the initiation (-0.013 to -0.070 10^{-3} s^{-1}). Only the first decrease from 120 to 90 minutes is a little bit more pronounced than the decrease of the following two time steps (-0.013 to -0.032 10^{-3} s^{-1}). In the last 30 minutes before thunderstorm initiation, the horizontal wind divergence values are getting much more negative compared to the 90 minutes before (-0.190 10^{-3} s^{-1}). The maximum updraft speed steadily increases at first (0.69 to 1.16 m s^{-1}), before a vigorous increase in the last 30 minutes before thunderstorm initiation (5.38 m s^{-1}). The detailed magnitudes for the mean, 10th and 90th percentile of each variable are summarised in Table 3.

Table 3: Temporal evolution of the magnitude (mean, 10th and 90th percentile) of Theta-E @ 850 hPa, horizontal wind divergence @ 850 hPa and maximum updraft for May 2018 and end of the century climate conditions:

Equivalent potential temperature (Theta-E) @ 850 hPa [K]						
May 2018				**End of Century**		
10th %ile	**Mean**	**90th %ile**	**Minutes before Initiation**	**10th %ile**	**Mean**	**90th %ile**
0	269.58	328.81	120	0	256.98	342.33
0	269.22	328.84	90	0	259.17	342.94
0	267.67	329.19	60	0	255.57	343.03
0	268.60	328.74	30	0	257.87	343.06
0	269.10	328.39	0	0	257.14	342.47

Horizontal wind divergence @ 850 hPa [10^{-3} s^{-1}]						
May 2018				**End of Century**		
10th %ile	**Mean**	**90th %ile**	**Minutes before Initiation**	**10th %ile**	**Mean**	**90th %ile**
-0.39	-0.019	0.35	120	-0.35	-0.013	0.335
-0.41	-0.034	0.33	90	-0.39	-0.032	0.340
-0.53	-0.056	0.36	60	-0.43	-0.035	0.356
-0.66	-0.094	0.39	30	-0.57	-0.070	0.371
-1.27	-0.222	0.54	0	-1.12	-0.190	0.432

Maximum updraft [m s^{-1}]						
May 2018				**End of Century**		
10th %ile	**Mean**	**90th %ile**	**Minutes before Initiation**	**10th %ile**	**Mean**	**90th %ile**
0.10	0.60	1.17	120	0.11	0.69	1.27
0.11	0.68	1.35	90	0.12	0.77	1.50
0.14	0.80	1.70	60	0.13	0.90	1.80
0.17	1.16	2.83	30	0.16	1.16	2.82
0.27	5.04	10.82	0	0.25	5.38	12.22

Comparing the magnitudes of the variables in both climate conditions, reveal a lower mean of Theta-E (268.834 to 257.346 K, -4.3 %) for the climate conditions at the end of the century. The opposite is true for the horizontal wind divergence (-0.085 to -0.068 10^{-3} s^{-1}, +20 %) and the maximum updraft (1.656 to 1.78 m s^{-1}, +7.5 %), which slightly increase in these conditions. The minimum Theta-E value 1 hour before the initiation is the only consistent pattern of the temporal evolution in both climate conditions. In May 2018, Theta-E decreases two time steps to this minimum value and increase again over the same time period. Whereas for future climate change conditions, an initial increase is detectable before this decrease. Afterwards, Theta-E decreases in the last half an hour before thunderstorm initiation. The temporal evolution patterns for the horizontal wind divergence and maximum updraft remain almost the same. Divergence just decrease slightly stronger from 120 to 90 minutes before the initiation.

Finally, the bulk wind shear 500 - 850 hPa (brown), zonal wind shear 500 - 850 hPa (turquoise) and meridional wind shear 500 - 850 hPa (pink) are shown for in Figure 5.6.1c) for May 2018. The bulk wind shear initially increased (7.23 to 7.35 m s^{-1}) and slightly decreased too (7.21 m s^{-1}). Its maximum value was then reached 30 minutes before the thunderstorm initiation (7.54 m s^{-1}). Afterwards, the bulk wind

Table 4: Temporal evolution of the magnitude (mean, 10th and 90th percentile) of bulk, zonal and meridional wind shear 500 - 850 hPa for May 2018 and end of the century climate conditions:

Bulk wind shear 500 - 850 hPa [m s^{-1}]						
May 2018				**End of Century**		
10th %ile	**Mean**	**90th %ile**	**Minutes before Initiation**	**10th %ile**	**Mean**	**90th %ile**
0	7.23	13.70	120	0	7.12	15.45
0	7.35	13.87	90	0	7.02	15.40
0	7.21	13.91	60	0	6.90	15.09
0	7.54	14.37	30	0	6.90	15.11
0	6.74	12.96	0	0	6.36	13.50

Zonal wind shear 500 - 850 hPa [m s^{-1}]						
May 2018				**End of Century**		
10th %ile	**Mean**	**90th %ile**	**Minutes before Initiation**	**10th %ile**	**Mean**	**90th %ile**
-6.01	-0.37	4.83	120	-6.01	-0.36	5.20
-6.22	-0.33	5.31	90	-6.35	-0.51	4.98
-6.23	-0.37	5.06	60	-5.97	-0.51	5.21
-6.60	-0.51	5.11	30	-6.41	-0.59	5.05
-6.74	-0.74	4.92	0	-6.40	-0.71	4.71

Meridional wind shear 500 - 850 hPa [m s^{-1}]						
May 2018				**End of Century**		
10th %ile	**Mean**	**90th %ile**	**Minutes before Initiation**	**10th %ile**	**Mean**	**90th %ile**
-5.75	3.51	12.31	120	-9.45	1.32	11.28
-5.66	3.64	12.43	90	-8.81	1.36	10.81
-5.54	3.50	12.42	60	-8.77	1.43	11.05
-5.60	3.65	12.72	30	-8.19	1.38	10.98
-4.87	2.85	10.81	0	-7.33	1.28	10.00

shear drops until the initiation time (6.74 m s^{-1}). The meridional wind shear follows the same pattern, solely that the last increase is less pronounced before reaching the maximum magnitude (3.50 to 3.65 m s^{-1}). The zonal wind shear exhibits an intensifying decrease (-0.33 to -0.74 m s^{-1}) after a first slightly increase from 120 to 90 minutes before thunderstorm initiation (-0.37 to -0.33 m s^{-1}).

Figure 5.6.2c) shows the temporal evolution of the different wind shears in end of the century climate conditions. The bulk wind shear constantly drops until the thunderstorm initiation (7.12 to 6.36 m s^{-1}), which includes a time step without any change of the mean value (6.9 m s^{-1}). After this stable period from 60 to 30 minutes before initiation, the decrease of the bulk wind shear is more pronounced during the last 30 minutes (6.90 to 6.36 m s^{-1}). This time, the zonal wind shear follows a similar pattern as the bulk wind shear. The difference occurs in the first and last time step. The zonal wind shear has a stronger decrease in the first time step (-0.36 to -0.51 m s^{-1}), but a less strong decrease in the last half an hour before thunderstorm initiation (-0.59 to -0.71 m s^{-1}). The meridional wind shear experiences an almost equal increase in the first two time steps (1.32 to 1.43 m s^{-1}) compared to the decrease of the last two time steps until the initiation of the thunderstorm (1.43 to 1.28 m s^{-1}). For both climate conditions,

the magnitudes of the mean, 10th and 90th percentile for each variable can be seen in Table 4.

Over all, the magnitudes of the mean values from the different wind shears only change slightly by comparing the two climate conditions. While the bulk wind shear decreases a little bit over all time steps (7.214 to 6.86 m s^{-1}, -4.9 %), the signal is not as clear for the zonal wind shear. There, the values decrease only for the time steps from 90 to 30 minutes before thunderstorm initiation, which is enough for a decrease of the mean (-0.464 to -0.536 m s^{-1}, -15.5 %). The most pronounced change can be seen in the values of the meridional wind shear, which strongly decreases in future climate conditions (3.43 to 1.354 m s^{-1}, -60.5 %). In these future climate changes conditions, bulk wind shear behaves differently compared to its temporal evolution in May 2018. The alternating increase and decrease, with a maximum value 30 minutes before the initiation, switches to a steady decrease in future climate conditions. But the strongest change still happens in the last half an hour before the initiation. Instead of the initial increase in the temporal evolution of May 2018, the zonal wind shear decreases from the beginning and most pronounced in the first 30 minutes. The temporal evolution of the meridional wind shear follows a similar pattern as the bulk wind shear in May 2018. But in end of the century climate conditions, the meridional wind shear increases during the first two time steps and decrease in the remaining hour until the initiation of the thunderstorm. Finally, I have to mention the need for significance tests of the results due to the high variability of the magnitudes in the data sets (comparing the 10th and 90th percentiles in the Tables 2, 3 & 4).

6 Discussion

This chapter discusses the research questions set out in the beginning. The aim of this study was to improve the understanding of thunderstorm initiation in Switzerland. Besides analysing specific thunderstorms (case studies), the analysis focused on the pre-storm environments of all thunderstorms in May 2018 and in end of the century conditions. The following subsections are divided accordingly to this separation.

6.1 Case Studies

In the results of each case study (see 5 Results), I investigated the basic ingredients for the initiation of the particular thunderstorm. Besides the assessment of a substantial amount of boundary-layer moisture, a conditional instability and a vertical wind shear, the focus was set on the investigation of the possible triggering mechanism of the thunderstorm initiation. Therefore, the research followed the questions set out in the beginning, which are answered in the following.

[A] How relevant was the presence of convergence for the initiation of selected thunderstorms in May 2018 in Switzerland?

Convergence could be detected in every case study, which implies the importance of its presence for thunderstorm initiation. All the triggering mechanisms were a combination with convergence. In the first, second and fifth case study, the orographic forcing triggered the initiation and convergence was resulting due to the topographic situation. In the third and fourth case study, the propagating gust fronts caused convergence and hence, initiated the thunderstorms. Consequently, I can attribute a high relevance to the presence of convergence for the initiation of thunderstorms in May 2018 in Switzerland.

[B] Which impact had storm outflow boundaries on the initiation of selected thunderstorms in May 2018 in Switzerland?

Storm outflow boundaries were responsible for thunderstorm initiation in two case studies (Case Study III and IV). More accurately, the outflow of the thunderstorm formed a cool pool with a propagating gust front. The airmasses were forced to ascent and strong updraft values could be detected. Thereof, the initiation of the thunderstorm was triggered (Case Study III) or intensified (Case Study IV). Both initiation locations are located in northeastern Switzerland. In this region, storm outflow boundaries commonly occur due to the principal eastward movement of thunderstorms in Switzerland. When they initiate in the west, they move without any obstacles over the Swiss Plateau towards the eastern part of Switzerland. Also in this case studies, the gust fronts propagated eastward before they reached the initiation location. To conclude, the impact of storm outflow boundaries was high especially in the two mentioned case studies.

[C] How far influenced the complex topography of Switzerland the initiation of selected thunderstorms in May 2018?

The complex topopgraphy of Switzerland had a direct influence on three case studies (Case Study I, II and V). In the first case study, the topography influenced the convergence and as a result the initiation processes. With its complexity, the topography was also in the second case study a major driver of the evolved convergence and the resulting thunderstorm initiation. But the biggest influence of the topography was on the initiation in the fifth case study. There, orographic-related forcing with the airflow convergence at the mountain top caused the initiation of this thunderstorm. After all, I can infer a strong influence of the complex topography of Switzerland on the initiation of selected thunderstorms in May 2018.

6.2 Pre-Storm Environments of All Thunderstorms

From the analysis of the pre-storm environments of all thunderstorms in May 2018 (see 5.6 Pre-Storm Environments of All Thunderstorms) resulted, inter alia, the temporal evolution of the different variables. In the following, the role of these variables and their temporal evolution is discussed in relation to the initiation process of a thunderstorm. Until 1 hour before the initiation, CAPE increased and CIN decreased. The higher CIN values 2 hours before the initiation inhibited the previous convection and hence, CAPE could build up. With the aforementioned decrease of CIN, convection is not longer inhibited and can start to form. With this initialised convection, CAPE decreases until the thunderstorm initiation. At the same time, the WVMR increases due to the boundary-layer water vapour inflow. This increase in the WVMR combined with higher boundary-layer temperature (i.e. increase in Theta-E), results in an increase of CIN in the last hour before the initiation. The strengthening of convection until the thunderstorm initiation correspond to an increase of the low-level convergence and the updraft. Furthermore, the initiating thunderstorm influences the vertical wind field and decreases the vertical wind shear by its up- and downdrafts.

The temporal evolution was also analysed for certain variables in the case studies, but mostly only in the last half an hour before thunderstorm initiation. There, the decreasing mean of CAPE can be detected in all case studies (except Case Study I), which corresponds to the same pattern as for the mean of all thunderstorms in May 2018. The increase of the WVMR and Theta-E (identified in the mean of all thunderstorms in May 2018) can be seen as well in the pre-storm environments of all case studies (except Case Study III for Theta-E). Moreover, the updraft of all case studies intensified in the last half an hour before the initiation, which corresponds to the pattern of all thunderstorms form May 2018. The increasing mean of CIN of all thunderstorms could solely be identified in Case Study II. But the reason for that can be probably found in the coarse analysis of CIN in the case studies (5 and 10 J kg^{-1} contour lines and area in skew T-log p diagram), which could not capture the small changes of CIN in the pre-storm environment. For the remaining variables (divergence and the various vertical wind shears), the pre-storm environment of the case studies was not analysed in such great detail.

For discussing how these conditions of the pre-storm environments may change in end of the century climate conditions, the corresponding research question stated in the beginning of this master thesis will now be answered:

[D] How might the temporal evolution of important variables before thunderstorm initiation and their magnitude change in future climate conditions?

The magnitude of the CAPE mean values increase strongly in end of the century climate conditions (+76.4 %), whereas, the increase is less pronounced for CIN (+25.9 %) and WVMR (+27.6 %). This robust increase in CAPE is projected for "most future time periods and greenhouse gas (GHG) scenarios" (Trapp et al., 2019, p. 5493). The temporal evolution patterns of CAPE and CIN do not change strongly in future climate conditions. This is more the case for the WVMR, where the mean is more fluctuating. The change of the magnitude is the strongest for divergence (+20 %), while Theta-E and updraft mean values only slightly change (-4.3 % and +7.5 %). The temporal evolution patterns of the horizontal wind divergence and the maximum updraft remain almost the same in both climate conditions. At the same time, Theta-E behaves differently and more variably, except the still present minimum value 60 minutes before the initiation. The magnitude of the mean bulk wind shear decreases (-4.9 %) as well as the mean zonal wind shear (-15.5 %). The mean of the meridional wind shear decreases the strongest of all vertical wind shears in end of the century climate conditions (-60.5 %). The zonal wind shear maintain a similar temporal evolution pattern in future climate conditions, other than bulk and meridional wind

shear. The bulk wind shear steadily decreases until the thunderstorm initiation and the meridional wind shear reaches already its maximum value 30 minutes earlier than in May 2018.

All these finding together lead me to the conclusion, that the potential for strong convection increases in end of the century climate conditions. This conclusion is supported by the higher number of thunderstorm initiations identified by TITAN in the end of century climate conditions (4311) compared to May 2018 (2686). The potential for strong convection is enhanced due to a strong increase of CAPE and a higher amount of water vapour present at this height level in the atmosphere, while CIN does not increase correspondingly strong. In addition, stronger updrafts indicate a higher potential for severe deep convection. What counters these arguments is the behaviour of the horizontal wind. The increase of divergence at 850 hPa corresponds to a decrease of low-level convergence. But the higher CIN values would require stronger lifting. Moreover, the decrease in bulk and meridional wind shear would infer a lower potential of thunderstorms with a long duration. The reason for the decrease in Theta-E, despite higher WVMR and warmer temperatures in future climate conditions, need to be further investigated (e.g. with Theta-E on multiple altitude levels). To conclude, I could assess favourable atmospheric conditions for the initiation of strong thunderstorms in end of the century climate conditions. Thereby, indications are present inferring a potential reduction of the duration of thunderstorm. In a next step, significance tests should be applied to these results, due to the high variability in the data sets.

7 Conclusion

7.1 Summary

To improve the understanding of conditions and processes leading to thunderstorm initiation, this master thesis conducted five case studies in May 2018 (see 5 Results). The research of this case studies, based on the WRF model data (see 3 Data), followed an ingredients-based methodology, after Doswell et al. (1996), and tried to define the basic ingredients for thunderstorm initiation (see 4.1 Case Studies). These atmospheric preconditions consist of a substantial amount of boundary-layer moisture, a conditional instability present in the atmosphere, a triggering mechanism to cause lifting of boundary-layer air and a vertical wind shear (Doswell et al., 1996; Stull, 2015; Wallace & Hobbs, 2006) (see 1.1 State of Knowledge). Related to these basic ingredients, the aim of the conducted case studies was to find the local thunderstorm triggering mechanisms in Switzerland in May 2018. Therefore, a novel research approach was implemented by using Lagranto in high resolution WRF model data. The backwards calculated trajectories with Lagranto, revealed new insights into the formation of the atmospheric profile. Based on this additional information, the origin of airmasses and evolution of certain variables along the trajectories could be determined. Combined with other analysis tools (horizontal maps, vertical cross-sections, pseudo-soundings, and maps of the variables' temporal evolution at a specified location), the basic ingredients for thunderstorm initiation were investigated and the local thunderstorm triggering mechanisms assessed. In all five case studies low-level convergence was present, which implies the importance of its presence for thunderstorm initiation. Further, storm outflow boundaries were responsible for thunderstorm initiation in two case studies and had a big impact on their thunderstorm initiation. Finally, the complex topopgraphy of Switzerland had a direct influence on three case studies and had a strong influence on the initiation of these selected thunderstorms.

In the second part of the master thesis, the focus shifted to the comparison of the pre-storm environments of all thunderstorms in May 2018 and in end of the century climate conditions (see 3 Data). The aim was to improve the understanding of how the pre-storm conditions of thunderstorms may be impacted by the changing climate conditions. This was achieved by analysing the temporal evolution and the magnitude of important variables for thunderstorm initiation in the pre-storm environments of both climate conditions. Besides the description of the temporal evolution (see 5.6 Pre-Storm Environments of All Thunderstorms), detailed information about the magnitudes of the mean, 10th and 90th percentile was provided. Based on these information, the changes could be assessed between the pre-storm environments in May 2018 and end of century climate conditions. By taking the mean of all thunderstorm initiations, a strong increase in CAPE (+76.4 %) was detected together with an increase in the WVMR (+27.6 %) and updraft (+7.5 %) in end of century climate conditions. With higher magnitudes of these variables, the potential for strong convection increases. The concurrent increase in CIN (+25.9 %) and the decrease in low-level convergence (-20 %) counter this previous finding. Because convergence should by higher to overcome the enhanced CIN. In addition, the decrease of all vertical wind shears implies a reduction of the thunderstorm duration in end of the century climate conditions.

7.2 Outlook

In a further step, significance tests need to be applied to the results of the pre-storm environments of all thunderstorms. To expand the analysis, the investigation area could be split into different regions (regionalisation) and the variables can be investigated at varying heights as well as complemented with other variables. Moreover, the same analysis approach could be used with other parameterisation schemes of the cloud microphysics or model data and investigate the resulting differences.

Because the thunderstorm research with the trajectories from Lagranto revealed new and interesting information about the formation of the atmospheric layers, this approach can be further extended from the case studies to more events. Thereby, the Lagrangian approach could be more generalised between the analysed thunderstorm initiations by the definition of comparable metrices (e.g. vertical wind shear of approaching trajectories). Last but not least, the thunderstorm triggering mechanisms in Switzerland should be further investigated in order to improve the understanding of the local triggering mechanisms in the complex topography of Switzerland. The gained knowledge of the conducted case studies and future work can help improving the forecast of these destructive and cost-intensive weather extremes.

Appendix

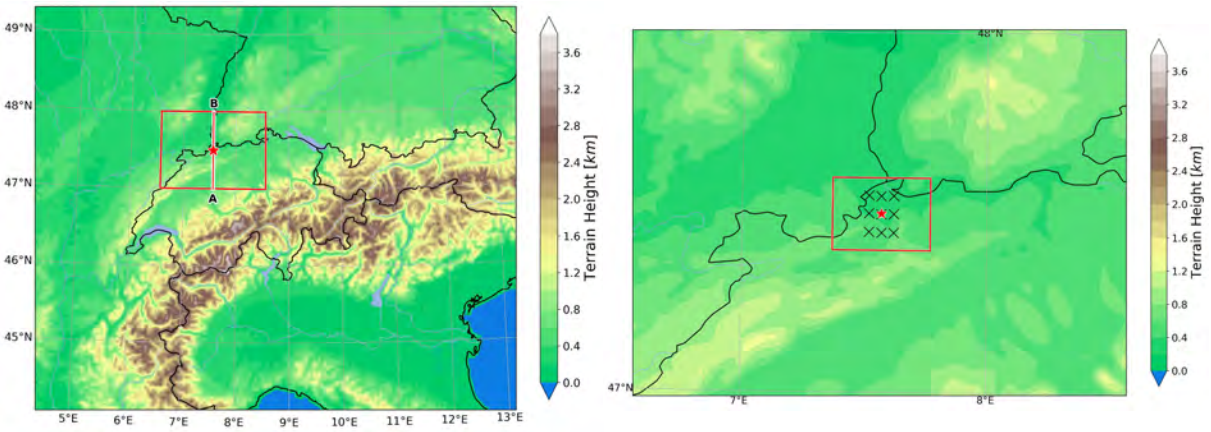

Figure 1: Terrain height [km] with location of thunderstorm initiation (7.56971° E, 47.4961° N, asterisk) of Case Study I. Left: Path of vertical cross-section (line from A (7.5697° E, 46.9961° N) to B (7.5697° E, 47.9961° N)) and extent of horizontal maps (rectangle). Right: Starting locations of trajectories (crosses; spatial distance of 0.05° in between) and smaller extent of horizontal figures (rectangle).

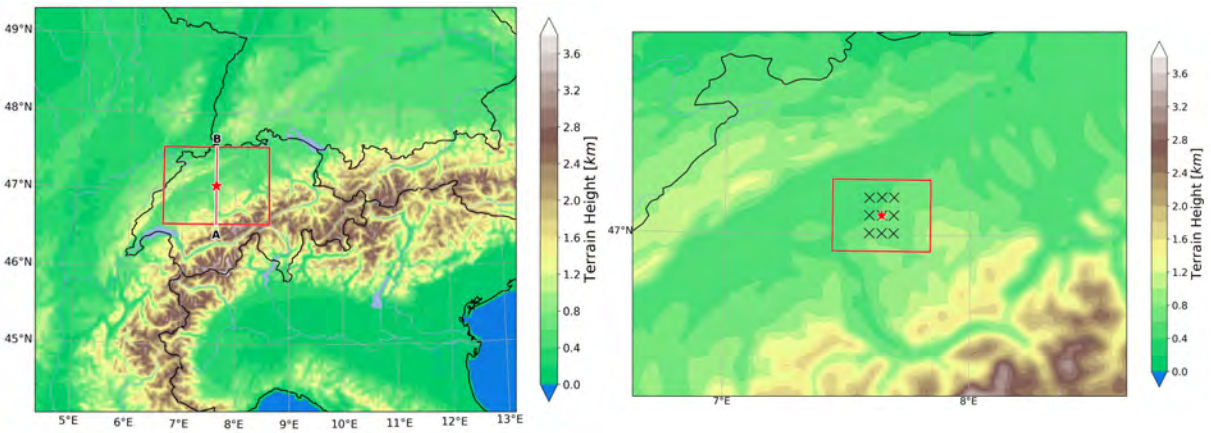

Figure 2: Terrain height [km] with location of thunderstorm initiation (7.63891° E, 47.0546° N, asterisk) of Case Study II. Left: Path of vertical cross-section (line from A (7.63891° E, 46.5546° N) to B (7.63891° E, 47.5546° N)) and extent of horizontal maps (rectangle). Right: Starting locations of trajectories (crosses; spatial distance of 0.05° in between) and smaller extent of horizontal figures (rectangle).

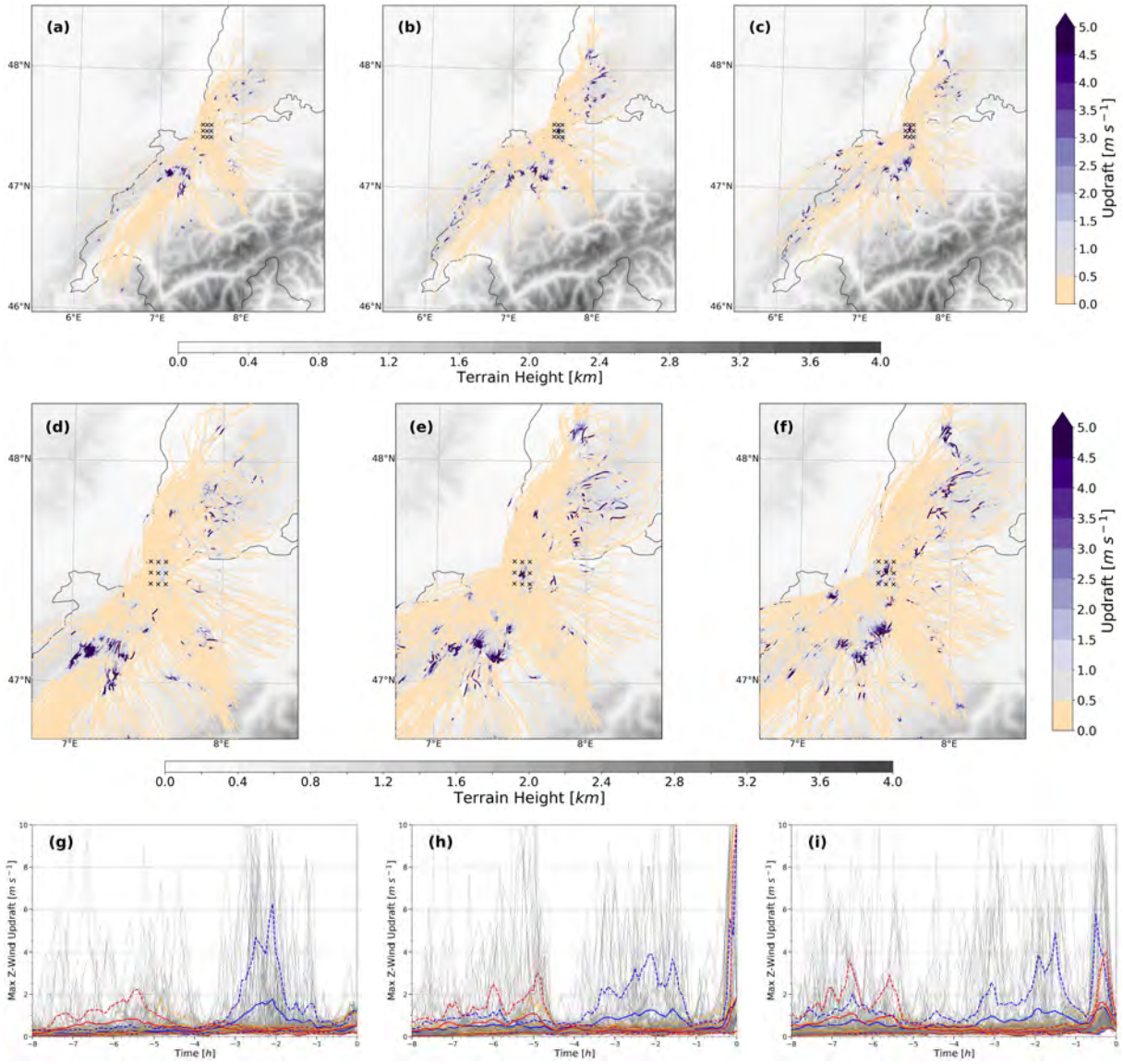

Figure 3: Same as Figure 5.1.1, but for maximum z-wind updraft [m s^{-1}].

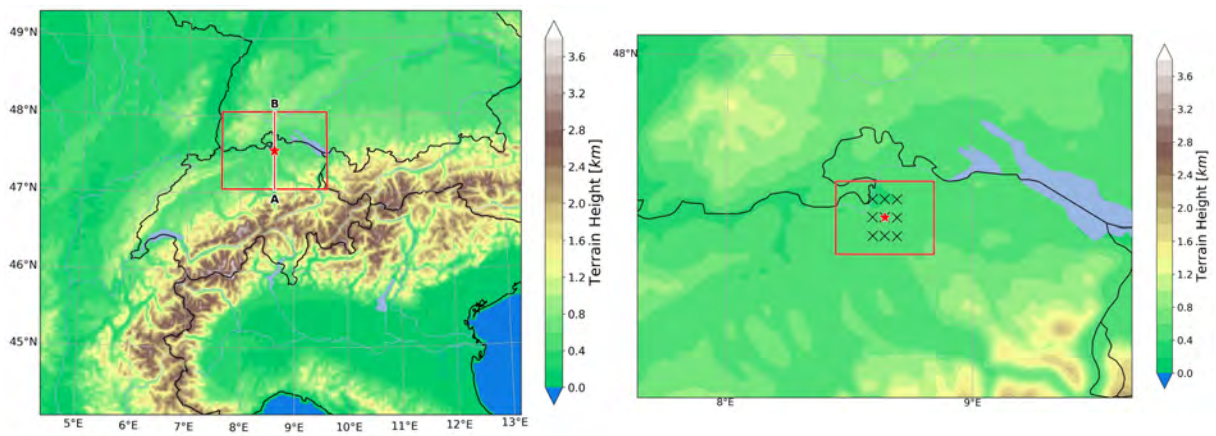

Figure 4: Terrain height [km] with location of thunderstorm initiation (8.64449° E, 47.5522° N, asterisk) of Case Study III. Left: Path of vertical cross-section (line from A (8.64449° E, 47.0522° N) to B (8.64449° E, 48.0522° N)) and extent of horizontal maps (rectangle). Right: Starting locations of trajectories (crosses; spatial distance of 0.05° in between) and smaller extent of horizontal figures (rectangle).

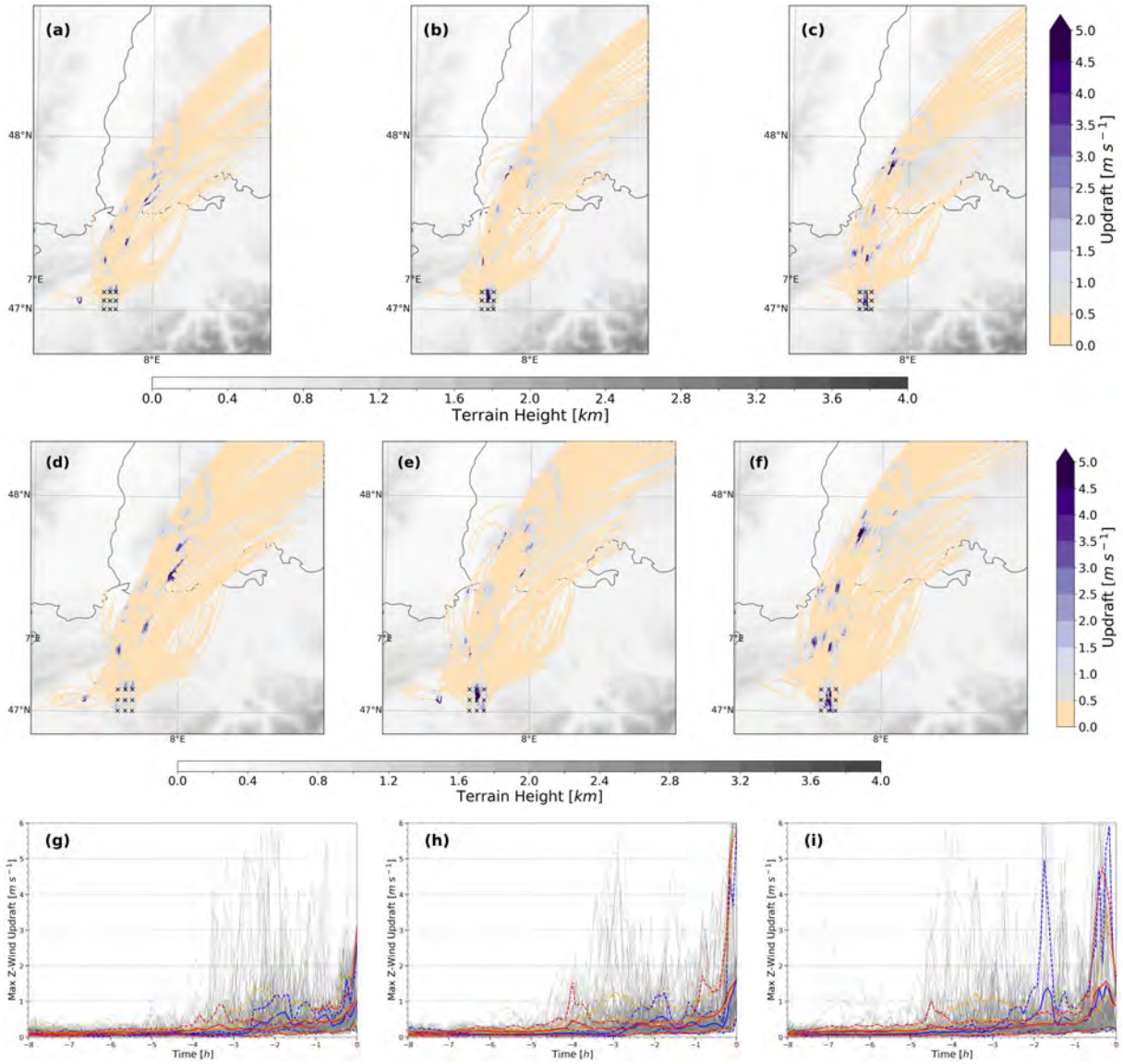

Figure 5: Same as Figure 5.2.1, but for maximum z-wind updraft [m s^{-1}].

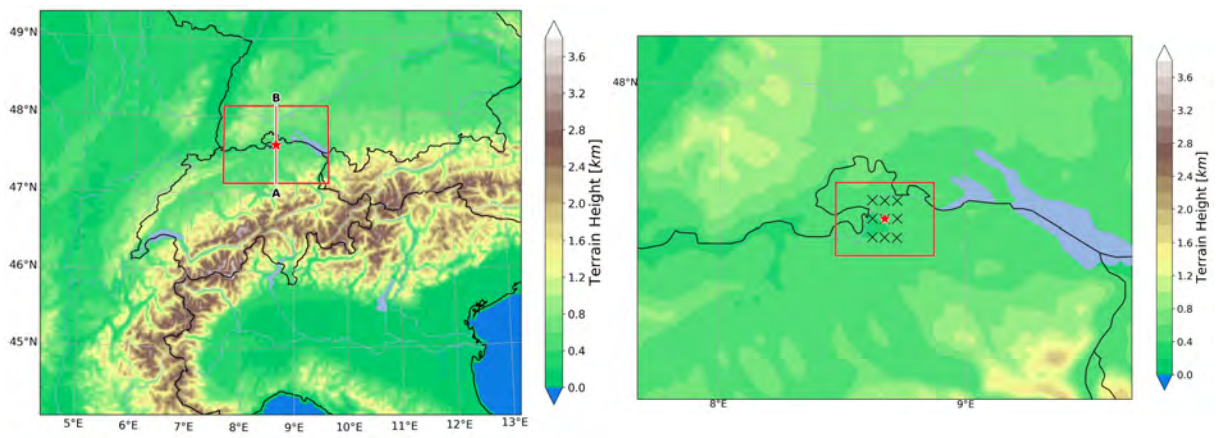

Figure 6: Terrain height [km] with location of thunderstorm initiation (8.67235° E, 47.629° N, asterisk) of Case Study IV. Left: Path of vertical cross-section (line from A (8.67235° E, 47.129° N) to B (8.67235° E, 48.129° N)) and extent of horizontal maps (rectangle). Right: Starting locations of trajectories (crosses; spatial distance of 0.05° in between) and smaller extent of horizontal figures (rectangle).

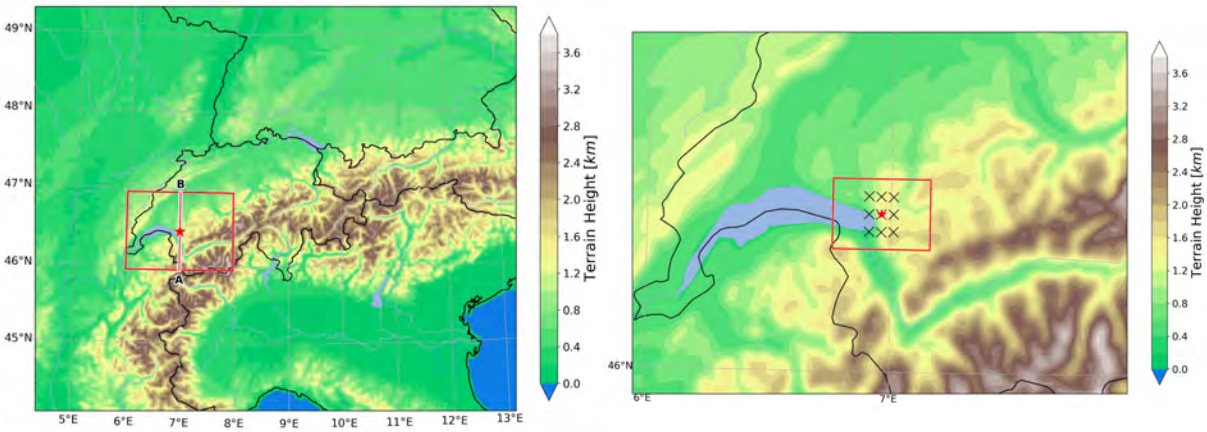

Figure 7: Terrain height [km] with location of thunderstorm initiation (6.95974° E, 46.4482° N, asterisk) of Case Study V. Left: Path of vertical cross-section (line from A (6.95974° E, 45.9482° N) to B (6.95974° E, 46.9482° N)) and extent of horizontal maps (rectangle). Right: Starting locations of trajectories (crosses; spatial distance of 0.05° in between) and smaller extent of horizontal figures (rectangle).

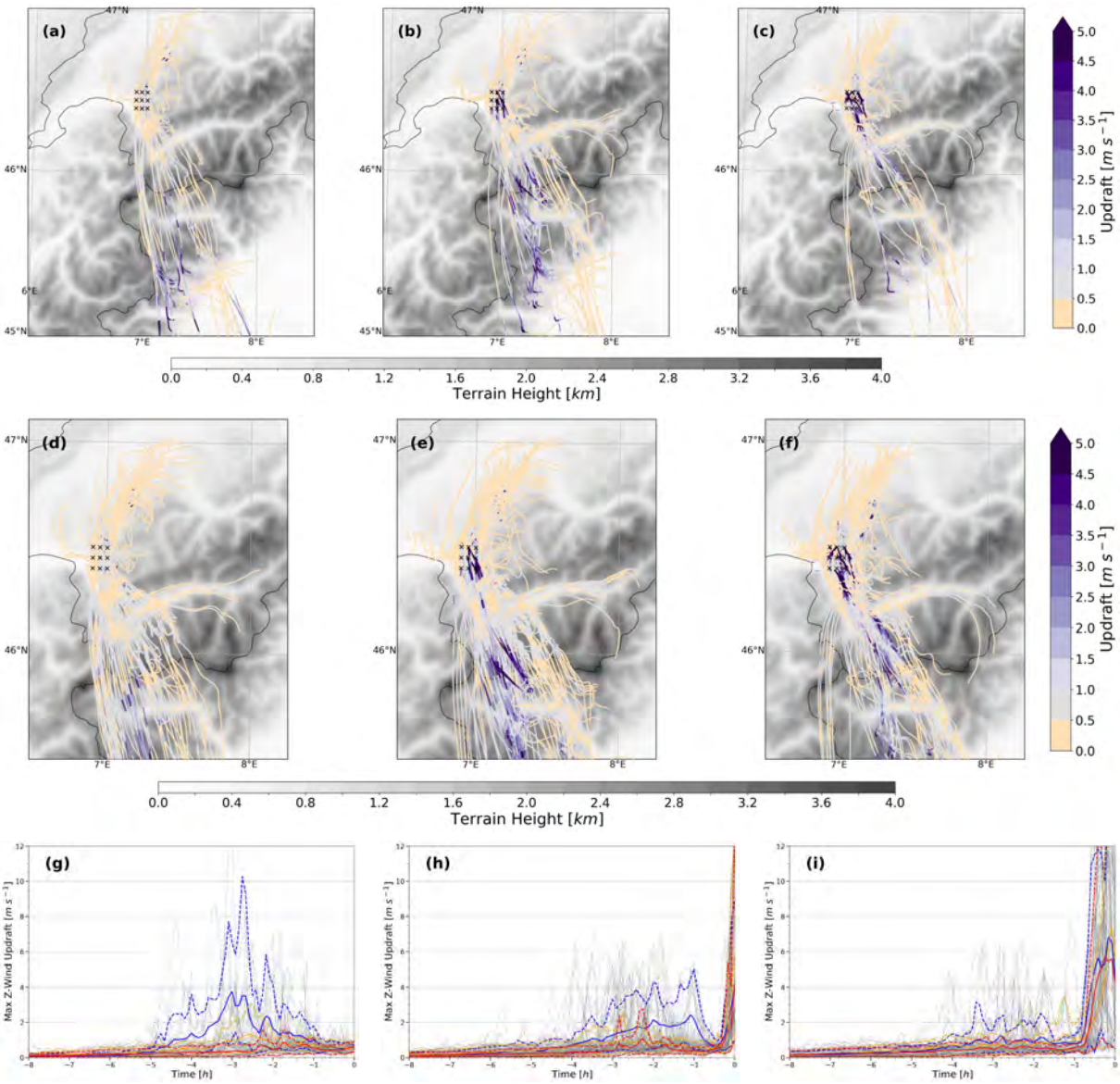

Figure 8: Same as Figure 5.5.1, but for maximum z-wind updraft [m s^{-1}].

Figures

Tables

Bibliography

Allen, J. T., Tippett, M. K., Kaheil, Y., Sobel, A. H., Lepore, C., Nong, S., & Muehlbauer, A. (2017). An extreme value model for u.s. hail size [Publisher: American Meteorological Society]. *Monthly Weather Review*, *145*(11), 4501–4519. https://doi.org/10.1175/MWR-D-17-0119.1

AMS. (2012, April 25). *Thunderstorm - AMS glossary*. Retrieved April 2, 2019, from http://glossary.ametsoc.org/wiki/Thunderstorm

Ban, N., Schmidli, J., & Schär, C. (2014). Evaluation of the convection-resolving regional climate modeling approach in decade-long simulations. *Journal of Geophysical Research: Atmospheres*, *119*(13), 7889–7907. https://doi.org/10.1002/2014JD021478

Ban, N., Schmidli, J., & Schär, C. (2015). Heavy precipitation in a changing climate: Does short-term summer precipitation increase faster? *Geophysical Research Letters*, *42*(4), 1165–1172. https://doi.org/10.1002/2014GL062588

Beniston, M., Stephenson, D. B., Christensen, O. B., Ferro, C. A. T., Frei, C., Goyette, S., Halsnaes, K., Holt, T., Jylhä, K., Koffi, B., Palutikof, J., Schöll, R., Semmler, T., & Woth, K. (2007). Future extreme events in european climate: An exploration of regional climate model projections. *Climatic Change*, *81*(1), 71–95. https://doi.org/10.1007/s10584-006-9226-z

Bott, A. (2016, May 20). *Synoptische meteorologie: Methoden der wetteranalyse und -prognose* (2. Aufl. 2016). Berlin Heidelberg, Springer Spektrum.

Brooks, H. E. (2009). Proximity soundings for severe convection for europe and the united states from reanalysis data. *Atmospheric Research*, *93*(1), 546–553. https://doi.org/10.1016/j.atmosres.2008.10.005

Browning, K. A., Blyth, A. M., Clark, P. A., Corsmeier, U., Morcrette, C. J., Agnew, J. L., Ballard, S. P., Bamber, D., Barthlott, C., Bennett, L. J., Beswick, K. M., Bitter, M., Bozier, K. E., Brooks, B. J., Collier, C. G., Davies, F., Deny, B., Dixon, M. A., Feuerle, T., ... Wieser, A. (2007). The convective storm initiation project. *Bulletin of the American Meteorological Society*, *88*(12), 1939–1956. https://doi.org/10.1175/BAMS-88-12-1939

Byers, H. R., & Braham, R. R. (1949). *The thunderstorm: Report of the thunderstorm project* [Google-Books-ID: D8sJAQAAIAAJ]. U.S. Government Printing Office.

CH2018. (2018). *CH2018 - climate scenarios for switzerland*. National Centre for Climate Services. Zurich.

Cotton, W. R., & Anthes, R. A. (1992, October 2). *Storm and cloud dynamics* [Google-Books-ID: X4WYgoBhYaQC]. Academic Press.

Dixon, M., & Wiener, G. (1993). TITAN: Thunderstorm identification, tracking, analysis, and nowcasting—a radar-based methodology. *Journal of Atmospheric and Oceanic Technology*, *10*(6), 785–797. https://doi.org/10.1175/1520-0426(1993)010⟨0785:TTITAA⟩2.0.CO;2

Doswell, C. A. (1987). The distinction between large-scale and mesoscale contribution to severe convection: A case study example [Publisher: American Meteorological Society]. *Weather and Forecasting*, *2*(1), 3–16. https://doi.org/10.1175/1520-0434(1987)002⟨0003:TDBLSA⟩2.0.CO;2

Doswell, C. A., Brooks, H. E., & Maddox, R. A. (1996). Flash flood forecasting: An ingredients-based methodology. *Weather and Forecasting*, *11*(4), 560–581. https://doi.org/10.1175/1520-0434(1996)011⟨0560:FFFAIB⟩2.0.CO;2

Federer, B., Waldvogel, A., Schmid, W., Hampel, F., Rosini, E., Vento, D., Admirat, P., & Mezeix, J. F. (1978). Plan for the swiss randomized hail suppression experiment. design of grossversuch IV. *pure and applied geophysics*, *117*(3), 548–571. https://doi.org/10.1007/BF00876634

Federer, B., Waldvogel, A., Schmid, W., Schiesser, H. H., Hampel, F., Schweingruber, M., Stahel, W., Bader, J., Mezeix, J. F., Doras, N., D'Aubigny, G., DerMegreditchian, G., & Vento, D. (1986). Main results of grossversuch IV [Publisher: American Meteorological Society]. *Journal of Climate*

and Applied Meteorology, *25*(7), 917–957. https://doi.org/10.1175/1520-0450(1986)025⟨0917:MROGI⟩2.0.CO;2

Galway, J. O. (1992). Early severe thunderstorm forecasting and research by the united states weather bureau. *Weather and Forecasting*, *7*(4), 564–587. https://doi.org/10.1175/1520-0434(1992)007⟨0564:ESTFAR⟩2.0.CO;2

García-Ortega, E., Fita, L., Romero, R., López, L., Ramis, C., & Sánchez, J. L. (2007). Numerical simulation and sensitivity study of a severe hailstorm in northeast spain. *Atmospheric Research*, *83*(2), 225–241. https://doi.org/10.1016/j.atmosres.2005.08.004

Graham, E., Koffi, E. N., & Mätzler, C. (2012). An observational study of air and water vapour convergence over the bernese alps, switzerland, during summertime and the development of isolated thunderstorms. *Meteorologische Zeitschrift*, *21*(6), 561–574. https://doi.org/10.1127/0941-2948/2012/0347

Haberlie, A. M., Ashley, W. S., & Pingel, T. J. (2015). The effect of urbanisation on the climatology of thunderstorm initiation. *Quarterly Journal of the Royal Meteorological Society*, *141*(688), 663–675. https://doi.org/10.1002/qj.2499

Hering, A. M., Morel, C., Galli, G., Sénési, S., Ambrosetti, P., & Boscacci, M. (2004). Nowcasting thunderstorms in the alpine region using a radar based adaptive thresholding scheme, In *Proceedings of ERAD*.

House, D. C. (1963). Forecasting tornadoes and severe thunderstorms (D. Atlas, D. R. Booker, H. Byers, R. H. Douglas, T. Fujita, D. C. House, F. H. Ludlum, J. S. Malkus, C. W. Newton, Y. Ogura, R. A. Schleusener, B. Vonnegut, & R. T. Williams, Eds.). In D. Atlas, D. R. Booker, H. Byers, R. H. Douglas, T. Fujita, D. C. House, F. H. Ludlum, J. S. Malkus, C. W. Newton, Y. Ogura, R. A. Schleusener, B. Vonnegut, & R. T. Williams (Eds.), *Severe local storms*. Boston, MA, American Meteorological Society. https://doi.org/10.1007/978-1-940033-56-3_7

Houze, R. A., Schmid, W., Fovell, R. G., & Schiesser, H.-H. (1993). Hailstorms in switzerland: Left movers, right movers, and false hooks [Publisher: American Meteorological Society]. *Monthly Weather Review*, *121*(12), 3345–3370. https://doi.org/10.1175/1520-0493(1993)121⟨3345:HISLMR⟩2.0.CO;2

Huntrieser, H., Schiesser, H. H., Schmid, W., & Waldvogel, A. (1997). Comparison of traditional and newly developed thunderstorm indices for switzerland. *Weather and Forecasting*, *12*(1), 108–125. https://doi.org/10.1175/1520-0434(1997)012⟨0108:COTAND⟩2.0.CO;2

IPCC. (2013). *Climate change 2013: The physical science basis. contribution of working group i to the fifth assessment report of the intergovernmental panel on climate change*. Cambridge, United Kingdom, New York, NY, USA, Cambridge University Press. https://doi.org/10.1017/CBO9781107415324

Johns, R. H., & Doswell, C. A. (1992). Severe local storms forecasting [Publisher: American Meteorological Society]. *Weather and Forecasting*, *7*(4), 588–612. https://doi.org/10.1175/1520-0434(1992)007⟨0588:SLSF⟩2.0.CO;2

Klose, B. (2016). *Meteorologie: Eine interdisziplinäre Einführung in die Physik der Atmosphäre* (3rd ed.). Springer Spektrum. https://doi.org/10.1007/978-3-662-43622-6

Kottmeier, C., Kalthoff, N., Barthlott, C., Corsmeier, U., van Baelen, J., Behrendt, A., Behrendt, R., Blyth, A., Coulter, R., Crewell, S., di Girolamo, P., Dorninger, M., Flamant, C., Foken, T., Hagen, M., Hauck, C., Höller, H., Konow, H., Kunz, M., ... Wulfmeyer, V. (2008). Mechanisms initiating deep convection over complex terrain during COPS. Retrieved April 23, 2019, from https://www.ingentaconnect.com/content/schweiz/mz/2008/00000017/00000006/art00018

Liu, C., Ikeda, K., Rasmussen, R., Barlage, M., Newman, A. J., Prein, A. F., Chen, F., Chen, L., Clark, M., Dai, A., Dudhia, J., Eidhammer, T., Gochis, D., Gutmann, E., Kurkute, S., Li, Y., Thompson, G.,

& Yates, D. (2017). Continental-scale convection-permitting modeling of the current and future climate of north america. *Climate Dynamics*, *49*(1), 71–95. https://doi.org/10.1007/s00382-016-3327-9

Markowski, P., & Richardson, Y. (2010). Mesoscale meteorology in midlatitudes. *Wiley*.

MeteoSwiss. (2018a, December 21). *2018: Rekordwärme und massive regenarmut*. Retrieved March 23, 2020, from https://www.meteoschweiz.admin.ch/home/suche.subpage.html/de/data/blogs/2018/12/2018-waermstes-jahr-seit-messbeginn-.html?query=sommer+2018+schweiz&topic=0&pageIndex=0&tab=search_tab

MeteoSwiss. (2018b, June 2). *Minimum der gewitteraktivität*. Retrieved June 8, 2019, from https://www.meteoschweiz.admin.ch/home/suche.subpage.html/de/data/blogs/2018/6/minimum-der-gewitteraktivitaet.html?query=gewitter+mai+2018+schweiz&topic=0&pageIndex=0&tab=search_tab

MeteoSwiss. (2018c, May 31). *Nochmals das gleiche?* Retrieved June 8, 2019, from https://www.meteoschweiz.admin.ch/home/suche.subpage.html/de/data/blogs/2018/5/nochmals-das-gleiche.html?pageIndex=0&query=gewitter%20mai%202018%20schweiz&tab=search_tab

MeteoSwiss. (2018d, May 30). *Warmer mai und extrem warmer frühling*. Retrieved June 8, 2019, from https://www.meteoschweiz.admin.ch/home/suche.subpage.html/de/data/blogs/2018/5/warmer-mai-und-extrem-warmer-fruehling.html?pageIndex=1&query=gewitter%20mai%202018%20schweiz&tab=search_tab

MeteoSwiss. (2019). *Klimareport 2018*. Bundesamt für Meteorologie und Klimatologie MeteoSchweiz. Zürich.

Morrison, H., & Milbrandt, J. A. (2014). Parameterization of cloud microphysics based on the prediction of bulk ice particle properties. part i: Scheme description and idealized tests. *Journal of the Atmospheric Sciences*, *72*(1), 287–311. https://doi.org/10.1175/JAS-D-14-0065.1

Nisi, L., Hering, A., Germann, U., & Martius, O. (2018). A 15 - year hail streak climatology for the alpine region. *Quarterly Journal of the Royal Meteorological Society*, *144*(714), 1429–1449. https://doi.org/10.1002/qj.3286

Nisi, L., Martius, O., Hering, A., Kunz, M., & Germann, U. (2016). Spatial and temporal distribution of hailstorms in the alpine region: A long-term, high resolution, radar-based analysis. *Quarterly Journal of the Royal Meteorological Society*, *142*(697), 1590–1604. https://doi.org/10.1002/qj.2771

Ogura, Y., & Takahashi, T. (1971). Numerical simulation of the life cycle of a thunderstorm cell. *Mon. Wea. Rev*, *99*(12), 895–911.

Ogura, Y. (1963). The evolution of a moist convective element in a shallow, conditionally unstable atmosphere: A numerical calculation [Publisher: American Meteorological Society]. *Journal of the Atmospheric Sciences*, *20*(5), 407–424. https://doi.org/10.1175/1520-0469(1963)020⟨0407:TEOAMC⟩2.0.CO;2

Pierce, E. T. (1976). The thunderstorm research international program (TRIP)—1976. *Bulletin of the American Meteorological Society*, *57*(10), 1214–1216. https://doi.org/10.1175/1520-0477(1976)057⟨1214:TTRIP⟩2.0.CO;2

Powers, J. G., Klemp, J. B., Skamarock, W. C., Davis, C. A., Dudhia, J., Gill, D. O., Coen, J. L., Gochis, D. J., Ahmadov, R., Peckham, S. E., Grell, G. A., Michalakes, J., Trahan, S., Benjamin, S. G., Alexander, C. R., Dimego, G. J., Wang, W., Schwartz, C. S., Romine, G. S., ... Duda, M. G. (2017). The weather research and forecasting model: Overview, system efforts, and future directions. *Bulletin of the American Meteorological Society*, *98*(8), 1717–1737. https://doi.org/10.1175/BAMS-D-15-00308.1

Rotunno, R., Klemp, J. B., & Weisman, M. L. (1988). A theory for strong, long-lived squall lines. *Journal of the Atmospheric Sciences*, *45*(3), 463–485. https://doi.org/10.1175/1520-0469(1988)045⟨0463:ATFSLL⟩2.0.CO;2

Schär, C., Frei, C., Lüthi, D., & Davies, H. C. (1996). Surrogate climate-change scenarios for regional climate models. *Geophysical Research Letters*, *23*(6), 669–672. https://doi.org/10.1029/96GL00265

Schemm, S., Nisi, L., Martinov, A., Leuenberger, D., & Martius, O. (2016). On the link between cold fronts and hail in switzerland. *Atmospheric Science Letters*, *17*(5), 315–325. https://doi.org/10.1002/asl.660

Schmid, W., Schiesser, H.-H., & Bauer-Messmer, B. (1997). Supercell storms in switzerland: Case studies and implications for nowcasting severe winds with doppler radar. *Meteorological Applications*, *4*(1), 49–67. https://doi.org/10.1017/S1350482797000388

Skamarock, C., Klemp, B., Dudhia, J., Gill, O., Liu, Z., Berner, J., Wang, W., Powers, G., Duda, G., Barker, D., & Huang, X.-y. (2019). A description of the advanced research WRF model version 4. https://doi.org/10.5065/1dfh-6p97

Sprenger, M., & Wernli, H. (2015). The LAGRANTO lagrangian analysis tool – version 2.0. *Geoscientific Model Development*, *8*(8), 2569–2586.

Stull, R. (2015). *Practical meteorology: An algebra-based survey of atmospheric science, dept. of earth, ocean & atmospheric sciences university of british columbia, vancouver, BC, canada.*

Sturmarchiv, S. (2019, January 5). *Extremereignisse 2018*. Retrieved June 8, 2019, from http://www.sturmarchiv.ch/index.php?title=Extremereignisse_2018

Trapp, R. J., Hoogewind, K. A., & Lasher-Trapp, S. (2019). Future changes in hail occurrence in the united states determined through convection-permitting dynamical downscaling [Publisher: American Meteorological Society]. *Journal of Climate*, *32*(17), 5493–5509. https://doi.org/10.1175/JCLI-D-18-0740.1

Trefalt, S., Martynov, A., Barras, H., Besic, N., Hering, A. M., Lenggenhager, S., Noti, P., Röthlisberger, M., Schemm, S., Germann, U., & Martius, O. (2018). A severe hail storm in complex topography in switzerland - observations and processes. *Atmospheric Research*, *209*, 76–94. https://doi.org/10.1016/j.atmosres.2018.03.007

Wallace, J. M., & Hobbs, P. V. (2006, March 24). *Atmospheric science: An introductory survey* [Google-Books-ID: HZ2wNtDOU0oC]. Elsevier.

Weckwerth, T. M., & Parsons, D. B. (2006). A review of convection initiation and motivation for IHOP_2002. *Monthly Weather Review*, *134*(1), 5–22. https://doi.org/10.1175/MWR3067.1

Wernli, H., & Davies, H. C. (1997). *A lagrangian-based analysis of extratropical cyclones. i: The method and some applications, QJ roy. meteor. soc., 123, 467–489.*

Wilson, J. W., & Schreiber, W. E. (1986). Initiation of convective storms at radar-observed boundary-layer convergence lines. *Monthly Weather Review*, *114*(12), 2516–2536. https://doi.org/10.1175/1520-0493(1986)114⟨2516:IOCSAR⟩2.0.CO;2

Acknowledgements

First of all, I would like to extend my gratitude to Prof. Dr. Olivia Romppainen-Martius for supervising my master thesis. Based on the many helpful remarks and discussions, the quality of this research could substantially be increased. Further, my thanks goes to my co-supervisors Dr. Timothy Raupach and Dr. Yannick Barton, which invested a lot of time in answering all my questions regarding the implementation of the research and its improvement. Last but not least, I would like to thank Dr. Michael Sprenger for the technical assistance with Lagranto and the helpful suggestions for the appropriate implementation and the thesis in general.

Acknowledgements have to be made to the IT support of Dr. Andrey Martinov, without the completion of my master thesis would not be possible, especially in this extraordinary COVID-19 time period. Many thanks goes additionally to the whole climate impacts group for their support in various topics and the fruitful discussions. This holds true in the same way for all the students in the fifth floor master's pool room. Thereby, Christoph von Matt deserves my special thanks due to assisting in initial trivialities and the improvement of my programming skills.

Finally, I want to thank my family and friends for their encouragement, support and love during the creation of this thesis as well as outside of the university.

Declaration of consent

on the basis of Article 30 of the RSL Phil.-nat. 18

Name/First Name: Lanz Thomas

Registration Number: 14-119-564

Study program: M.Sc. in Climate Sciences

Bachelor ☐ Master ☑ Dissertation ☐

Title of the thesis: Lagrangian Analysis of Thunderstorms in Switzerland

Supervisor: Prof. Dr. Olivia Romppainen-Martius

I declare herewith that this thesis is my own work and that I have not used any sources other than those stated. I have indicated the adoption of quotations as well as thoughts taken from other authors as such in the thesis. I am aware that the Senate pursuant to Article 36 paragraph 1 litera r of the University Act of 5 September, 1996 is authorized to revoke the title awarded on the basis of this thesis.
For the purposes of evaluation and verification of compliance with the declaration of originality and the regulations governing plagiarism, I hereby grant the University of Bern the right to process my personal data and to perform the acts of use this requires, in particular, to reproduce the written thesis and to store it permanently in a database, and to use said database, or to make said database available, to enable comparison with future theses submitted by others.

Thun, August 31, 2020

Place/Date

Signature